ผลของมอดุลัสของยังของชั้นสารยึดติดที่มีต่อรูปแบบการแตกร้าวของโครงสร้างชั้นเปราะ

นางสาวพรทิพย์ สกลกูล

วิทยานิพนธ์นี้เป็นส่วนหนึ่งของการศึกษาตามหลักสูตรปริญญาวิทยาศาสตรมหาบัณฑิต
สาขาวิชาฟิสิกส์ ภาควิชาฟิสิกส์
คณะวิทยาศาสตร์ จุฬาลงกรณ์มหาวิทยาลัย
ปีการศึกษา 2547

ISBN 974–53–1030–1

EFFECT OF YOUNG'S MODULUS OF ADHESIVE LAYER ON FRACTURE MODES OF BRITTLE LAYER STRUCTURES

Miss Porntip Sakolkool

A Thesis Submitted in Partial Fulfillment of the Requirements
for the Degree of Master of Science in Physics
Department of Physics
Faculty of Science
Chulalongkorn University
Academic Year 2004

ISBN 974-53-1030-1

Thesis Title	Effect of Young's Modulus of Adhesive Layer on Fracture Modes of Brittle Layer Structures
By	Miss Porntip Sakolkool
Field of Study	Physics
Thesis Advisor	Associate Professor Prapaipan Chantikul, Ph.D.
Thesis Co–advisor	Natthaphon Wuttiphan, Ph.D.

Accepted by the Faculty of Science, Chulalongkorn University in Partial Fulfillment of the Requirements for the Master's Degree

……. Dean of the Faculty of Science
(Professor Piamsak Menasveta, Ph. D.)

THESIS COMMITTEE

……Chairman
(Assistant Professor Pisistha Ratanavararak, Ph. D.)

……Thesis Advisor
(Associate Professor Prapaipan Chantikul, Ph. D.)

……Thesis Co–advisor
(Natthaphon Wuttiphan, Ph.D.)

……Member
(Assistant Professor Chaisingh Poo-Rakkiat, Ph. D.)

……Member
(Assistant Professor Rattachat Mongkolnavin, Ph. D.)

พรทิพย์ สกลกูล : ผลของมอดุลัสของยังของชั้นสารยึดติดที่มีต่อรูปแบบการแตกร้าวของโครงสร้างชั้นเปราะ. (EFFECT OF YOUNG'S MODULUS OF ADHESIVE LAYER ON FRACTURE MODES OF BRITTLE LAYER STRUCTURES) อ. ที่ปรึกษา : รศ. ดร. ประไพพรรณ ฉันธิกุล, อ. ที่ปรึกษาร่วม : ดร. ณฏฐพล วุฒิพันธุ์, 117 หน้า. ISBN 974–53–1030–1.

งานวิจัยนี้ได้ทำการตรวจสอบผลของมอดุลัสของยังของชั้นสารยึดติดที่มีต่อรูปแบบการแตกร้าวของโครงสร้างชั้นเปราะโดยวิธีการอินเดนเทชันด้วยหัวกดทรงกลม เราใช้โครงสร้างสามชั้นซึ่งประกอบด้วย แก้วชั้นผิว (หนา 500 และ 1000ไมครอน) เชื่อมกับแก้วชั้นฐาน (หนา 5.8 มิลลิเมตร) ด้วยสารยึดติดพอลิเมอร์ (หนา 20 และ 200 ไมครอน) ที่มีค่ามอดุลัสของยังแตกต่างกัน โดยชั้นผิวถูกกดด้วยหัวกดทรงกลมทังสเตนคาร์ไบด์ (รัศมี1.59 มิลลิเมตร) เป็นโครงสร้างชั้นเปราะจำลองในงานวิจัยนี้ สารยึดติดพอลิเมอร์ที่เลือกให้มีค่ามอดุลัสของยังต่างๆกันในช่วงกว้าง ได้แก่ สตีลอีพอกซี เรซิน, อีพอกซี เรซิน และ ซิลิโคน ซีลแลนท์ จากการวัดค่ามอดุลัสของยังของสารยึดติดด้วยวิธีทดสอบเทนไซล์พบว่าสตีลอีพอกซี เรซินมีค่ามอดุลัสของยังมากที่สุด ขณะที่ซิลิโคน ซีลแลนท์มีค่ามอดุลัสของยังน้อยที่สุด เราใช้เทคนิคบอนด์อินเทอร์เฟสร่วมกับการใช้กล้องจุลทรรศน์แบบสะท้อนแสงในการตรวจสอบรูปแบบรอยร้าวที่เกิดขึ้นจากการที่กดชั้นผิวของโครงสร้างสามชั้นด้วยหัวกดทรงกลมทังสเตนคาร์ไบด์ เราพบว่าเมื่อแรงกดมีค่าสูงพอ เกือบทุกระบบโครงสร้างชั้นที่มีความหนาของชั้นผิวและชั้นสารยึดติดแตกต่างกันจะมีรอยร้าวรูปโคนเกิดขึ้นที่ผิวของแก้วชั้นบนก่อนและมีรอยร้าวรัศมีเกิดขึ้นที่ผิวล่างของแก้วชั้นบนตรงรอยต่อระหว่างชั้น โดยค่าโหลดวิกฤตที่ทำให้เกิดรอยร้าวรูปโคนจะมีค่าต่ำกว่าค่าโหลดวิกฤตที่ทำให้เกิดรอยร้าวรัศมี

ในงานวิจัยนี้พบว่าค่าโหลดวิกฤตที่ทำให้เกิดรอยร้าวรูปโคนและรอยร้าวรัศมีจะมีค่าต่ำที่สุดเมื่อโครงสร้างชั้นมีซิลิโคน ซีลแลนท์เป็นตัวเชื่อมระหว่างชั้น และจะมีค่าสูงที่สุดเมื่อโครงสร้างชั้นนั้นมีสตีลอีพอกซี เรซินเป็นตัวเชื่อมระหว่างชั้น ทั้งนี้เป็นเพราะชั้นตัวเชื่อมซิลิโคน ซีลแลนท์มีค่ามอดุลัสของยังน้อยมากจึงเกิดการโค้งได้มากกว่าชั้นเชื่อมต่อที่เป็นสตีลอีพอกซี เรซิน อันส่งผลให้ชั้นผิวของโครงสร้างชั้นเปราะที่มีซิลิโคน ซีลแลนท์ เป็นตัวเชื่อมต่อระหว่างชั้นเกิดการโค้งมากกว่าชั้นผิวของโครงสร้างชั้นเปราะที่มีสตีลอีพอกซี เรซินเป็นตัวเชื่อมระหว่างชั้น

ภาควิชา.....ฟิสิกส์..... ลายมือชื่อนิสิต……

สาขาวิชา.....ฟิสิกส์..... ลายมือชื่ออาจารย์ที่ปรึกษา..……

ปีการศึกษา.....2547…….. ลายมือชื่ออาจารย์ที่ปรึกษาร่วม……...

4472340723 : MAJOR PHYSICS

KEY WORDS : YOUNG'S MODULUS / FRACTURE MODES / LAYER STRUCTURES

PORNTIP SAKOLKOOL : EFFECT OF YOUNG'S MODULUS OF ADHESIVE LAYER ON FRACTURE MODES OF BRITTLE LAYER STRUCTURES. THESIS ADVISOR : ASSOC. PROF. PRAPAIPAN CHANTIKUL, PH.D., THESIS CO-ADVISOR : NATTHAPHON WUTTIPHAN, PH.D., 117 pp. ISBN 974-53-1030-1.

An investigation is made of the role of Young's modulus of adhesive interlayer in determining fracture modes in brittle layer structures from indentation with hard spheres. A trilayer system consisting of a glass coating layer (thicknesses of 500 and 1000 μm) joined to a glass substrate (thickness of 5.8 mm) by an adhesive polymer(thicknesses of 20 and 200 μm), loaded at its coating surface with a hard tungsten carbide sphere (radius 1.59 mm), is used as a model system in this work. Steel-epoxy resin, epoxy resin and silicone sealant which have a broad range of Young's modulus are used as the three different adhesive interlayers in this work. Young's modulus measured for each of the chosen adhesive interlayer using tensile tests indicates that the steel-epoxy resin has the highest value of Young's modulus, whereas the silicone sealant has the lowest value of Young's modulus. A bonded-interface technique together with a reflection optical microscopy is used to reveal crack profiles of the specimens due to contact with the tungsten carbide sphere. For almost all specimens of various layer geometries (different thicknesses of coating layer or adhesive interlayer) used in this work, it is found that if the contact load is sufficiently high, both the cone crack initiated at the top surface of the coating layer and the radial crack initiated at the lower surface of the coating layer are generally evident. The critical contact loads for the cone crack initiation are always found to be lower than those for the radial crack initiation.

At any layer geometry, it is found that both the critical loads for cone crack and radial crack initiation are the lowest for the layer specimens with silicone sealant interlayer, and they are the highest in the layer specimens with steel-epoxy resin interlayer. Such finding is attributed to the unequal ability of the different adhesive interlayer to flex due to the contact load. The silicone sealant interlayer having lower Young's modulus can be flexed more than the steel-epoxy resin interlayer during the contact, and consequently can allow its coating layer to flex more than the coating layer of the specimen with steel-epoxy resin interlayer.

Department……Physics….	Student's signature…….....
Field of study….Physics….	Advisor's signature……
Academic year….2004…....	Co-advisor's signature……...

ACKNOWLEDGEMENTS

I would like to express my sincere gratitude and deep appreciation to my advisor Assoc. Prof. Dr. Prapaipan Chantikul and Dr. Natthaphon Wuttiphan (co-advisor) for valuable guidance and encouragement throughout this thesis.

I wish to express my special thanks to the thesis committee, Assist. Prof. Dr. Pisistha Ratanavararak, Assist. Prof. Dr.Chaisingh Poo-Rakkiat and Assist. Prof. Dr. Rattachat Mongkolnavin for their reading and comment.

I would like to acknowledge the National Science and Technology Development Agency (NSTDA) for scholarship and Chulalongkorn University for financial-support research. I also would like to acknowledge the National Metal and Materials Technology Center (MTEC) and Department of Physics, Faculty of Science of Chulalongkorn University for laboratory assistance in this thesis.

My appreciation also goes to Dr. Pavadee Aungkavattana, Miss Patthamaporn Timakul and Miss Lugsanee Pinyo for their kindness and suggestion. I would like to thank MTEC staffs for their expert and helpful and I am also grateful to my true friends for their help and eternal friendship.

Finally, I would like to express my faithful thanks to my mother for her support and encouragement throughout the entire study.

Contents

Contents (continued)

Page

List of Figures

Page

List of Figures (continued)

Page

List of Figures (continued)

Page

List of Figures (continued)

Page

List of Figures (continued)

Page

List of Figures (continued)

Page

List of Tables

Page

CHAPTER I

INTRODUCTION

1.1 High - Technology Ceramics

According to the National Academy of Sciences, USA, ceramics are inorganic, nonmetallic, materials processed or consolidated at high temperatures. High-technology ceramics are different from the traditional clay-based ceramic products like tiles, tablewares, sanitarywares, and refractory bricks. They are actually highly purified, chemically- prepared powders, which are mixed and fired to make materials like alumina, silicon nitride, silicon carbide, zirconia, barium titanate, and synthetic ferrites.

Table 1 lists many inherently useful and unique properties of high-technology ceramics. Valued for their superior properties, these materials are being developed for use in high-performance applications [1, 2]. The biggest use of high-technology ceramics in the electronic component business is for packaging of integrated circuit. They are also extensively used in electronic capacitors and, to a lesser extent, in other electronic components such as resistors, sensors and transducers. Ceramic capacitors are primarily comprised of complex barium titanate or strontium titanate. Ceramic sensors include many forms of alumina. Magnetic ceramics of both soft ferrites and permanent hard ferrite magnets are used in applications ranging from recording heads and temperature sensors to fractional horsepower motors and other permanent magnet applications. Ceramics are also used in biological functions and joint materials. For

optical applications, nearly transparent alumina and mullite are used for the high-pressure sodium-vapor lamps that have revolutionized outdoor lighting, and for special-purpose infrared transmission windows. Ceramics are used for laser hosts.

Table 1.1 Useful Properties of High-Technology Ceramics

High resistance to chemical corrosion
High melting point
High hardness
High compression strength
High wear resistance
Low weight per volume
Biocompatibility
Optical transparency
Tailored dielectric constant
High piezoelectric constant
High piezoelectric coupling coefficient
High magnetic permeability
Fast ion conduction

Cutting tools of alumina, titanium carbide, and silicon nitride are in use and constitute a significant fraction of the throwaway cutting tools appropriate for numerically controlled machine tools and other automatic production systems which make tool reuse less practical. Similarly, wear-resistance materials such as alumina, zirconia, and silicon carbide are becoming used as mechanical seals, liners, bearings, thread guides, and pressure sensors.

Brittleness is an overriding factor, which largely limits the ultimate usefulness of ceramics. Under tensile stresses, their rigid covalent or ionic-covalent bonding of atoms cannot stretch but tends to break. This means that they are highly susceptible to failure from small scale (1-100 μm) flaws. These flaws may be in the form of machining damage, grain boundary fissures, processing defects (pores or inclusions), etc. In any industrial applications, a proper understanding of the microfracture-controlled properties, particularly strength and toughness, is paramount.

1.2 Ceramic Layer Structures

In the past decade of research in the area of structural ceramics, there are significant advancements in the understanding and exploitation of microstructural tailoring as a means of enhancing mechanical behaviors [3, 4]. This includes not only conventional properties such as strength and toughness, but also more complex behaviors such as contact damage, mach inability, and resistance to wear/erosion. Composites, in which ceramic layers of different composition and/or microstructure are combined, provide a new and intriguing dimension to this area of research. The specific application for the layered structure will determine the optimum composition, microstructure and layer geometry. Their properties can be tailored to meet specific requirements that the constituent layer materials cannot. For example, a hard ceramic coating can protect a softer and tougher metal substrate from wear while the metal substrate provides fracture resistance [5]. A bilayer structure, which consists of HAp as top layer and tough bioceramics as substrate can provide an artificial substitution for an implant to be used in orthopedic and dental surgeries [6]. The hydroxyapatite

top layer can stimulate hard tissue growth which bridges the bilayer implant to bone while the tougher substrate provides fracture resistance.

There are different philosophies for achieving the required property improvements. One of the methods is the development of surface compressive residual stress in outer layers. This approach results in an increase in the strength and the “apparent” fracture toughness [7,8]. The other approach is to deliberately introduce weak interfaces in order to promote crack deflection for toughening [9-12]. The more recent method is the development of layered structures with strong interfaces in order to avoid crack deflection along the interface. Russo *et al.* [13, 14] propose a tri-layer composite design in which the inner layer consists of material with a strong R-curve (a material which fracture toughness increases as a function of crack length), sandwiched by the outer layers of a high strength, non R-curve material. These systems exhibit high strengths over a wide range of starting flaw sizes.

Brittle layers can be joined together into laminate structures with a weak adhesive interlayer. Practical examples are seashells, natural teeth, dental crowns, car windscreens, and some thermal barrier coatings. The brittle layers afford stiffness, wear resistance and durability; the compliant interlayer provides damage tolerance, by redistributing stresses, and confining fractures within individual brittle layers. The adhesive needs to be weak enough to prevent cracks from penetrating into adjacent layers but strong enough to preclude delamination failures [15,16].

Since the damage tolerance of ceramic layer structures are especially conspicuous in concentrated loading configuration, such as indentation with hard spheres, and projectile impacts, indentation testings in which a hard indenter is loaded onto the surface of testing pieces [17], have become extensively used to

systematically investigate fracture and deformation properties of ceramic layer system [4,18-28]. Indentation damage bears profoundly on a wide range of other mechanical properties, such as strength, toughness and wear. The contact damages accumulated from indentation testing are contributing to a new design philosophy of ceramic layer structures. Critical elements of the new philosophy are: (i) incorporation of strong rather than weak interlayer interfaces, to avoid delamination; (ii) adjustment of elastic-plastic mismatch between layers so as to partition energy from the contact loading system into competing fracture and quasi-plastic modes. And thus to suppress (rather than deflect) any cone (or other) cracks that originate in the outer layers. This philosophy has been demonstrated on several material systems: ceramic bilayers, alumina/alumina [4,19,29], glass/glass-ceramic [20], and silicon nitride/silicon nitride [21-23]; thermal barrier coatings [24-28]; and simulated dental structures [18].

Most of works mentioned in the last paragraph performed on ceramic-bilayer system in which coating layers are fused to substrates. Contact experiment on brittle layer systems in which brittle layers are joined together with an adhesive interlayer have also been conducted on a glass/soft-epoxy resin/glass system (same Young's modulus between the coating layer and the substrate) and a glass/soft-epoxy resin/polycarbonate system (different Young's modulus between the coating layer and the substrate). These works demonstrate that the presence of the adhesive interlayer has a profound influence on the critical contact loads for the initiation of contact fractures as well as the types and severity of the contact fracture modes. Consequently, extensions of the indentation experiment to investigate the effect of flaw state on the strength [30], and the effect of the layer geometry [31-33], such as

the coating layer thickness and the adhesive thickness, have been made on this glass/soft epoxy resin/glass and glass/ epoxy resin/polycarbonate system.

1.3 Objectives and Scope of this work

In section 1.1, we have already pointed out as to why ceramics are extensively used in many high-performance applications even though they are brittle. In section 1.2, research works done on tailoring ceramic layer structures in order to improve the load bearing capacity and damage tolerance property of their constituent layers as structural components have been reviewed. Due to the potential use of ceramic layer structures, effects of the various variables, such as the Young's modulus mismatch between the coating layer and the substrate, the coating layer thickness and the thickness of the adhesive interlayer, on their strength and damage tolerance properties have been investigated (section 1.2).

Near the end of section 1.2, for ceramic layer structures fabricated by joining ceramic layers together via a soft epoxy resin interlayer, we have particularly pointed out that the soft epoxy resin interlayer has a profound influence on the fracture modes introduced in them. However, the Young's modulus of the adhesive polymer interlayer which can have important influence on their fracture properties has not yet been examined. Therefore in this work, we investigate such an effect of Young's modulus of the adhesive polymer interlayer on fracture modes of brittle layer structures. The Hertzian indentation test is used to introduce contact damages into the coating layer of the layer system. The glass/adhesive polymer/glass is used as our model specimen. Glass is chosen for both its coating layer and substrate because any observed difference in important variables, such as the critical contact loads for

fracture initiation, the types and severity of the contact fracture modes can be attributed to the influence of the Young's modulus of the adhesive polymer interlayer. The layout of this work is as follows:

(i) Young's modulus measurements of glass and various available adhesive polymers are performed.

(ii) Three different types of adhesive polymers, which have a broad range of Young's modulus, are used in this work.

(iii) Trilayer specimens consisting of a glass coating layer (thickness of 500 and 1000 μm) joined to a glass substrate (thickness of 5.8 mm) by an adhesive polymer of three different Young's modulus (thickness of 20 and 200 μm) are prepared.

(iv) The Hertzian-indentation tests are performed by loading a tungsten carbide sphere (radius of 1.59 mm) onto the surface of the glass-coating layer. A widest possible range of indentation load is used.

(v) A bonded-interface technique together with a reflection optical microscopy is used to reveal the contact damages in the specimens.

Accordingly, the thesis is set out as follows. In Chapter 2, theoretical background of materials used to fabricate our layer specimens and Hertzian fracture are given. The Young's modulus measurements, layer preparations and Hertzian indentation tests are described in Chapter 3. Then, the experimental results obtained from our work are presented in Chapter 4. Finally, discussion and conclusions drawn from this study are presented in Chapter 5.

CHAPTER II

THEORETICAL BACKGROUND

2.1 Glass

Glasses are amorphous solids. There are a large number of glass types differing in compositions, properties, as well as application purposes. The basic types are distinguished according to the chemical character of the main components, e.g. oxide glasses, chalcogenide glasses, halogenide glasses. The silicate glasses, based on silicon dioxide SiO_2, are the most important type, and are manufactured on the largest scale. Silica glass, which contains virtually 100% SiO_2, is the simplest type. To achieve advantageous technological properties, additional substances are usually introduced into glass. The composition of silicate glasses may vary over a relatively wide range; in spite of this, most of them can be ranked into some of the following groups designated according to the other significant oxides present: soda-lime glass, boric glass, alumina glass, lead glass.

Similar to crystalline silicates, the SiO_4 tetrahedron constitutes the basic structural unit of silicate glasses (Fig. 2.1a). The small silicon cation at its center is surrounded by four larger oxygen anions. The Si—O bonds are ionic – covalent and of high strength. Being bivalent, oxygen is always shared by two silicon atoms and thus by two tetrahedra. In this way, all the tetrahedra are mutually linked, irregularly, but at all four corners, so that their interactions are considerable.

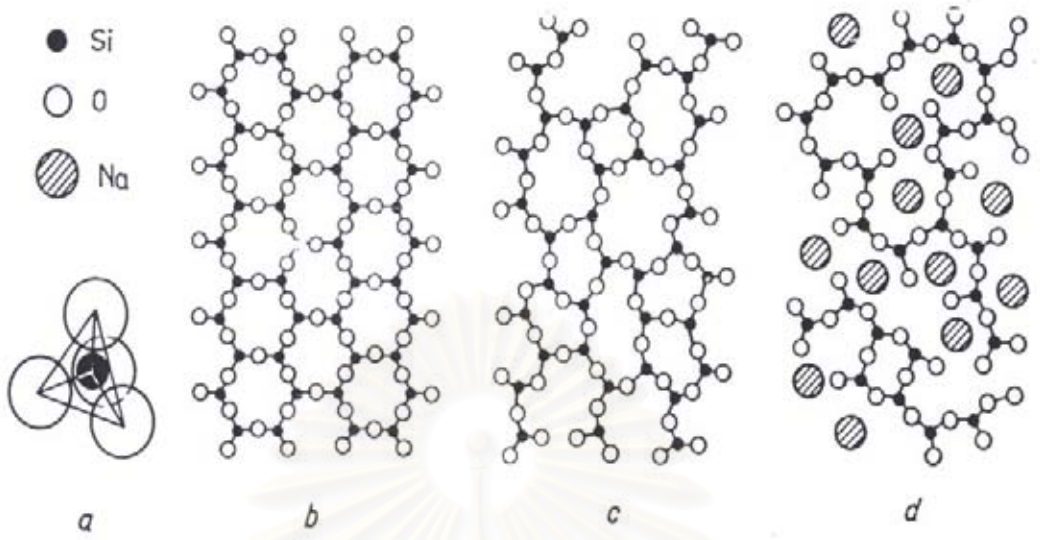

Fig. 2.1 Characteristic features of silicate structure. Courtesy of J. Mencik [34].

The example demonstrated schematically in Fig. 2.1c corresponded to silica glass. Most silicate glasses contained additional oxides besides SiO_2. According to their roles in the formation of the glassy lattice, they can be divided into glass-formers or network-formers (SiO_2, B_2O, P_2O_5, etc.), and modifiers (Na_2O, K_2O, etc.). Between the two groups, there are the transient oxides (Al_2O_3, MgO, etc.) Glass-formers are those oxides that alone are capable of creating a glassy network, and excess oxygen anions are responsible for breaking some of the Si—O bonds (Fig. 2.1d). This is why the modifiers are for example capable of decreasing the glass melting temperature. However, some of them, particularly Na_2O, will also considerably impair the chemical durability and other properties of glass, so that stabilizers such as CaO have to be introduced into the glass.

Glass is brittle material and does not deform plastically before failure. It fails in tension regardless of the nature of loading. The potential tensile strength of glass is about 6.895 GPa, but failure occurs at average stresses far below this value because of

the stress-raising effect of surface imperfections both inherent in the glass and mechanically created [34-37].

Due to its transparency (enabling “in situ” observation of crack accumulation and evolution within it during experiments), commercially availability and inexpensive, soda-lime glass is typically used as a model material in most experiments investigating fracture properties of brittle materials. It is also used in experiments exploring fracture modes in brittle layer structures either as their coating layer alone [30-32] or both coating layer and substrate [33]. In this work, we use it as both coating layer and substrate by joining them together with an adhesive polymer.

2.2 Polymer

This section will focus on a fundamental knowledge of polymer because adhesive polymer will be used as an interlayer of our model brittle layer structure. The behavior of adhesive polymer during loading and fracture is decisively affected by their structures, which depends on both the composition and the manufacturing. The basic features of polymer structures will be given here.

From a microstructural point of view, polymers are much more complex than metals and ceramics. On the other hand, they are inexpensive and easily processed. Many of polymers are organic compounds that are chemically based on carbon, hydrogen, and other nonmetallic elements. Furthermore, they have very large molecular structures. Polymers have lower strengths and moduli and lower temperature-use limits than do metals or ceramics. Because of their predominantly covalent bonding, polymers are generally poor conductors of heat and electricity. Polymers are generally more resistant to chemicals than are metals, but prolonged

exposure to ultraviolet light and some solvents can cause degradation of polymer's properties[36,38].

Polymers are giant chainlike molecules (hence, the name macromolecules), with covalently bonded carbon atoms forming the backbone of the chain. Polymerization is the process of joining together many monomers, the basic building blocks of polymers, to form the chains. For example, an ethyl alcohol monomer has the chemical formula C_2H_5OH. The structural formula of ethyl alcohol is represented by

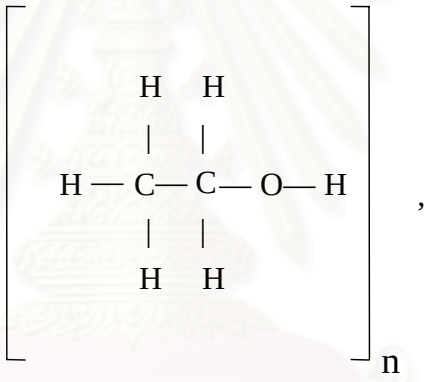

,

where n is the degree of polymerization.

The difference in the behavior of polymers stems from their molecular structure and shape, molecular size and weight, amount and type of bonds (covalent or van der Waals). The different chain configurations are shown in Fig. 2.2. A *linear polymer* consists of a long chain of atoms with attached side groups (fig. 2.2(a)). Examples include polyethylene, polyvinyl chloride, and polymethyl methacrylate. *Branched polymers* have branches attached to the main chain (Fig. 2.2(b)). Branching

can occur with linear, cross-linked, or any other types of polymers. A *cross-linked* polymer has molecules of one chain bonded with those of another (Fig. 2.2(c)).

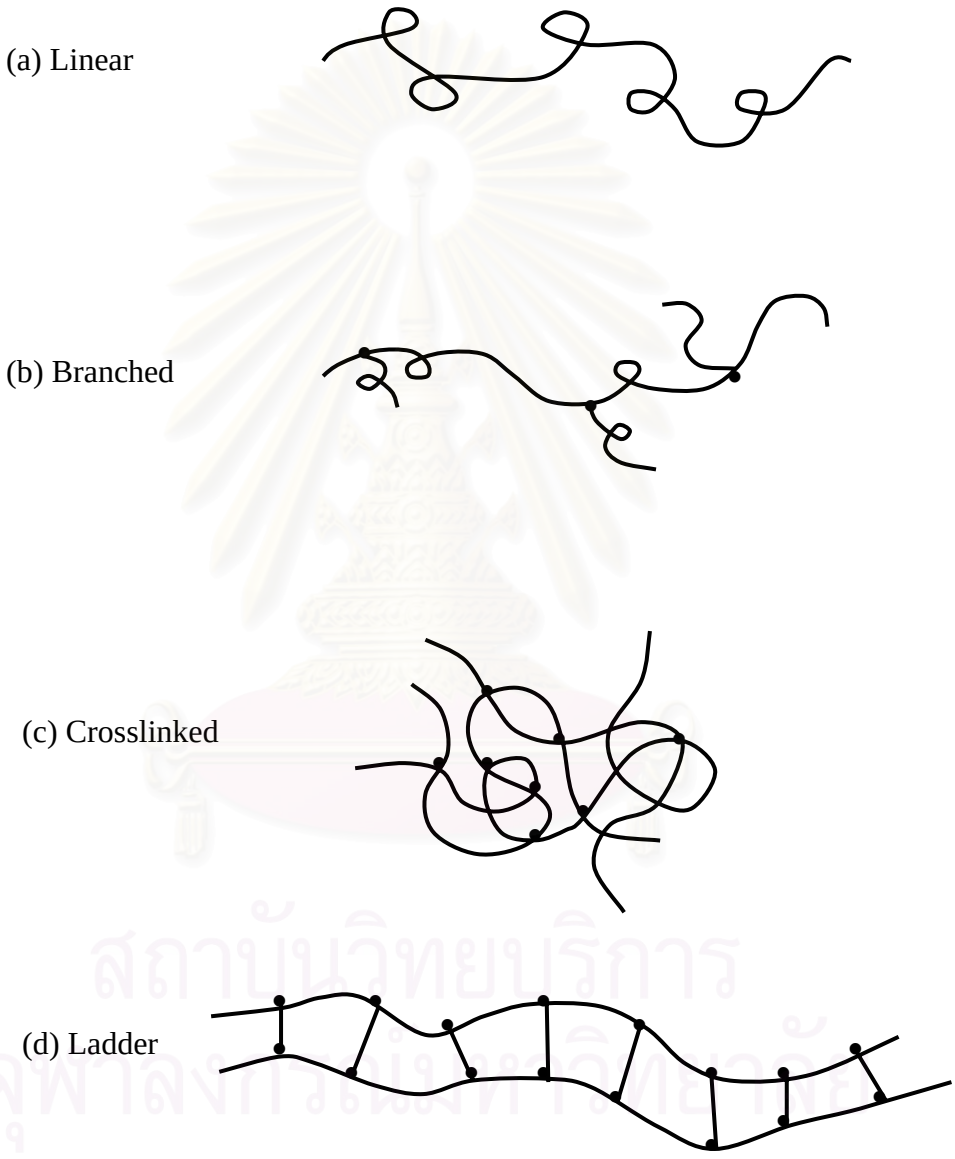

Fig. 2.2 Different types of molecular chain configurations. Courtesy of M.A. Meyers and K. K. Chawla [38].

Cross- linking of molecular chains results in a three-dimensional network. It is easy to see that cross-linking makes sliding of molecules past one another difficult, resulting in strong and rigid polymers. *Ladder polymers* have two linear polymers linked in a regular manner (Fig. 2.2(d)). As a result, ladder polymers are more rigid than linear polymers.

Based on their behavior upon heating, polymers can be divided into two broad categories[38]:

(i) Thermosetting polymers

(ii) Thermoplastics

When the molecules in a polymer are cross-linked in the form of a network, they do not soften on heating. These cross-linked polymers are *thermosetting* polymers. Thermosetting polymers decompose upon heating. Cross-linking makes sliding of molecules past one another difficult, which produces a strong and rigid polymer. A typical example is rubber cross-linked with sulfur, i.e. vulcanized rubber has 10 times the strength of natural rubber. Common examples of thermosetting polymers include phenolic, polyester, polyurethane, and silicone. Polymers that soften or melt upon heating are called *thermoplastics*. Thermoplastics are suitable for liquid flow processing, they are mostly linear polymers- for example, low-and high–density polyethylene and polymethyl methacrylate (PMMA).

2.3 Adhesive Polymer

Adhesive is defined as a non metallic material that is capable of joining bodies together by surface adhesion and internal strength (adhesion and cohesion) without

the structure of the bodies undergoing significant change. Adhesive is an essential bonding agent, conveniently and widely used.

2.3.1 Epoxy Resin and Steel – Epoxy Resin

Epoxy resin adhesives are recognized as the adhesive featuring a versatile chemical functionality and a remarkably low shrinkage on curing. This leads to obtain reliable adhesion joints with low internal stress, excellent cohesion, structural integrity, and outstanding adhesion to all kinds of substances. For example, bonds can be made to metals and glass without resorting to the application of pressure during the bonding process and without any problem in bonding irregular surfaces.

It is of technological significance that the manner in which these adhesives are used is reminiscent of well-known metal soldering techniques. Therefore, the discovery of the bonding function of epoxy resins introduced a new concept in adhesives materials and inaugurated the modern approach to the technology of adhesive bonding.

Epoxy resin based adhesives [39] can be produced in various forms: one and two part liquids, film, or solvent based. This wide variety of formulations is indicative of the advanced state of the art of epoxy adhesives.

The epoxy, epoxide, oxirane, or ethoxyline group [40] is a three-membered ring consisting of a oxygen atom attached to two connected carbon atoms:

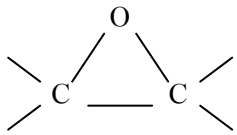

The term “epoxy resin” usually refers to an intermediate molecule, which contains at least two reactive epoxy groups. Such resins are categorized as “thermosetting” since they are capable of “curing” to form cross-linked networks. The rings can be opened by either as catalysts for homopolymerization or as reactive hardeners.

Epoxy resins are thermo hardening compounds which contain one or more epoxy resins. There are a large number of compounds that can be classified under this category. They are oligomers that become polymers if they are joined into a network by cross-linking agents.

The variation of properties with formulation indicates the wide range of structural applications for which epoxy adhesives can be designed. For example, phenolic-modified epoxy resins produce the best high-temperature adhesives, whereas steel-epoxy combinations produce adhesives with high joint strengths.

2.3.2 Silicone Sealant

Silicone sealants are based on tough silicone elastomeric technology [41]. Silicone sealants have a high degree of flexibility and very high temperature resistance (up to 600 °F) when compared to other adhesives. While silicone sealants have a high degree of flexibility, they lack the strength of other epoxy or acrylic

resins. Silicone sealants are available in two-component addition or condensation curing systems or single component room temperature vulcanizing (RTV) forms. RTV forms cure through reaction with moisture in the air and give off aciatic acid fumes or other by-product vapors during curing. Silicone sealants are available in a number of technologies (or cure systems). These technologies include pressure sensitive, radiation cures, moisture cured, thermoset and RTV.

Pressure sensitive silicone adhesives adhere to most surfaces with very slight pressure and they retain their tackiness. They form viscoelastic bonds that are aggressively and permanently tacky, and adhere without the need of more than finger or hand pressure. Ultraviolet (UV) or radiation cured silicone sealants use ultraviolet light, visible light or electron beam irradiation to initiate curing, which allows a permanent bond without heating or excessive heat generation. One disadvantage of UV curing adhesives is the requirement that one substrate is UV transparent. Some UV resin systems employ a secondary curing mechanism to complete curing of adhesive regions shielded from the UV light. The electron beam (EB) curable adhesives use electron beam radiation to cure or initiate curing. The electron beam can penetrate through material that is opaque to UV light. Reactive moisture cured resins are single component adhesives. They are applied like hot melt adhesives until the resin reacts with moisture to crosslink and polymerize, resulting in a cured material. Certain silicone adhesives and cyanoacrylates also use a reaction with moisture or water to cure the adhesive or sealant. Thermoset silicone sealants, which are crosslinked polymeric resins, do not melt and flow when heated, but they may soften. Vulcanization is a thermosetting reaction involving the use of heat and/or pressure in conjunction with a vulcanizing agent materials. The vulcanizing agent is a

crosslinking compound or catalyst. Sulfur is the traditional vulcanizing agent used with natural rubber. Silicones use moisture, acetic acid and other compounds as curing agents.

The widely used in silicone sealants applications are glazing of frame panels and shop front, automotive and marine work, curtail wall sealing, and general sealant: sheet metal, skylight, ventilators, air conditioning, metal or plastic signs.

2.4 Young's modulus

The important elastic constants are Young's modulus, Poisson's ratio, and the shear modulus. Young's modulus, which is measured most often, is defined as

$$E = \sigma/\varepsilon, \tag{2.1}$$

where σ is the normal stress, and ε is the tensile strain. The shear modulus, G, is defined analogously:

$$G = \tau/\gamma, \tag{2.2}$$

where τ is the shear stress and γ is the shear strain. The coefficient of lateral contraction (Poisson's ratio), ν, is rather difficult to measure. It can be obtained in a simpler way by calculation from E and G according to

$$\nu = \frac{E - 2G}{2G}. \tag{2.3}$$

The moduli E and G can be determined by static or dynamic methods. Static methods consist in measuring deformation of a specimen under known static load. Dynamic methods investigate the resonant frequency of a beam in bending or a rod in torsion, or the velocities of the longitudinal or transverse elastic waves within the

material, measured with an ultrasonic detector. Our attention will be limited only to static measurements, which can be carried out in laboratories with simple equipments.

2.5 Hertzian Fracture

We begin with a consideration of the frictionless contact of a hard sphere, radius *r*, at normal load *P*, on a flat specimen surface as shown in Fig. 2.3. The nature of the stresses arising from the contact between two elastic bodies is of considerable importance and was first studied by Hertz in the 1880s [42]. The contact pressure increases monotonically with load from zero at first contact. As the load increases, the contact point expands into cycle. The stress field is initially elastic, as the classical Hertzian stress field [42,43]. In brittle ceramics, the crack evolution events for one complete indentation depicted schematically in Fig. 2.4 [44]: (a) pre-present surface flaws are subjected to tensile stresses outside the contact zone; (b) at some point in the loading a favorably located flaw runs around the contact circle to form a surface “ring” crack; (c) on further loading the embryonic ring crack grows incrementally downward in the rapidly weakening tensile field; (d) at critical load the ring becomes unstable and propagates downward into the full frustum of the Hertzian cone (pop-in); (e) at still further loading the cone continues in stable growth (unless the contact circle expands beyond the ring crack, in which case the cone is engulfed in the compressive contact zone); (f) on loading, the cone crack closes.

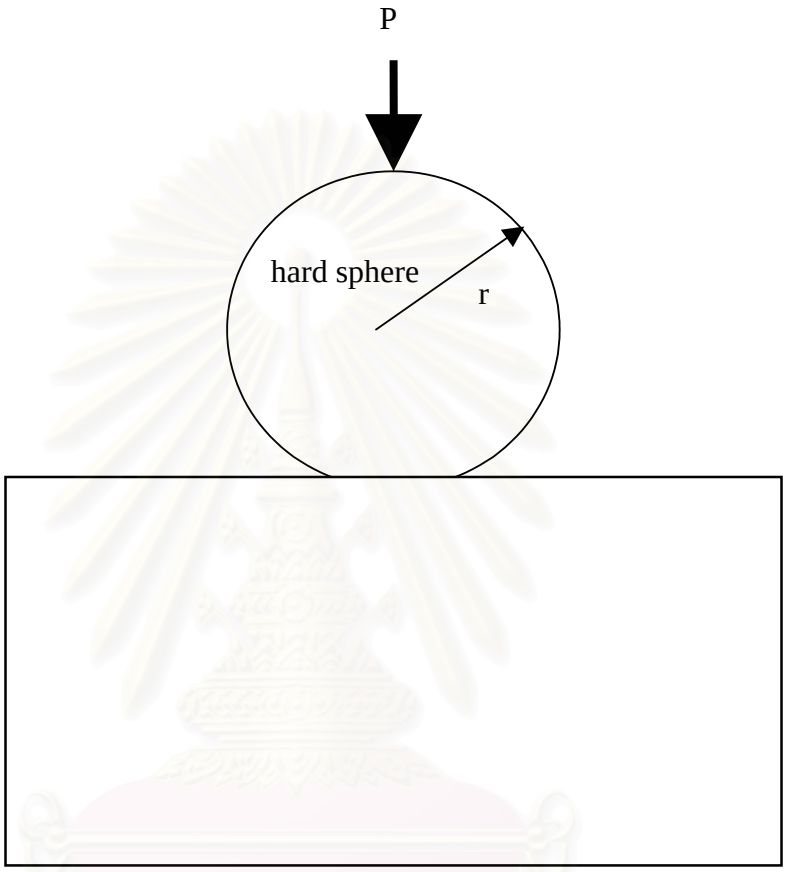

Fig. 2.3 Contact of a hard sphere on a flat specimen and parameters of Hertzian contact test

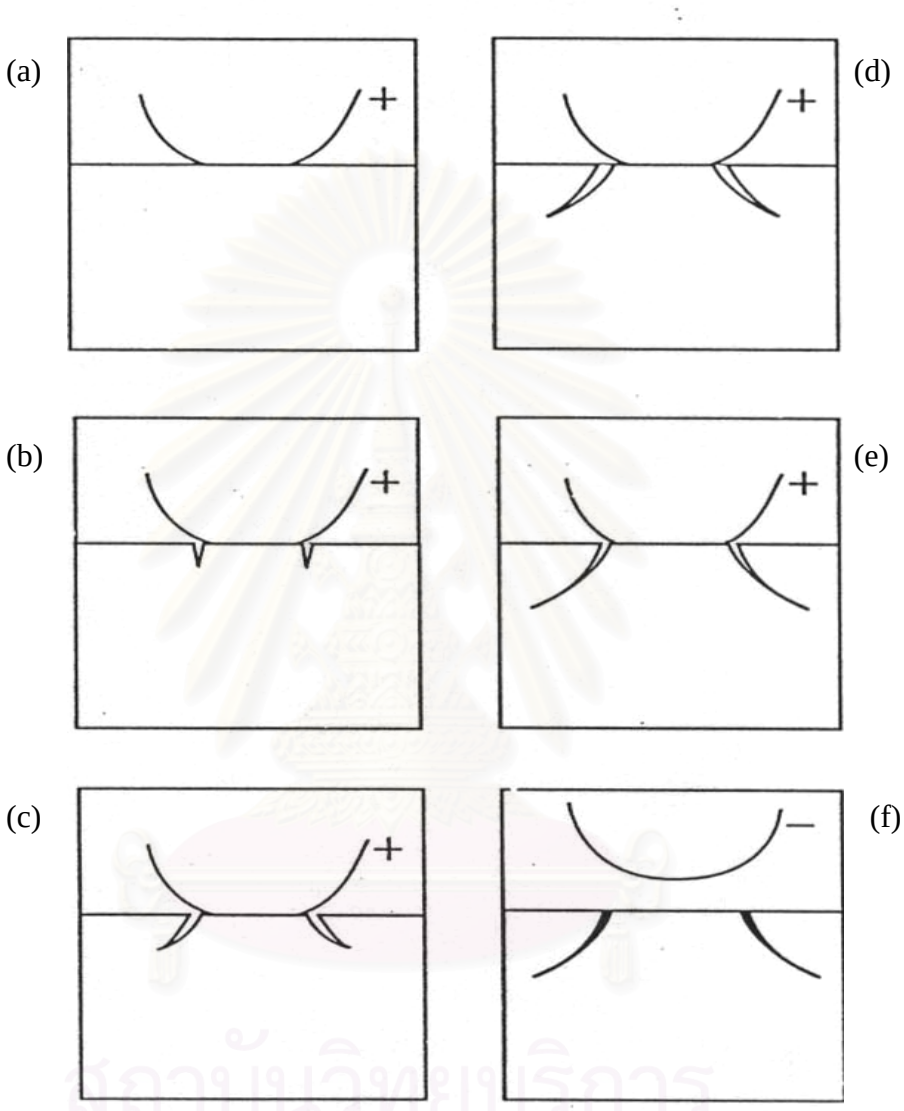

Fig. 2.4 Hertzian cone crack system. Evolution of cone during complete loading (+) and unloading (-) cycle. Courtesy of B.R.Lawn[44].

2.5.1 Brittle Fracture

Investigations on fracture properties of ceramics have indicated that brittleness is an inherent property of ceramics. Brittle fracture is essentially an atomistic process in which cohesive bonds are ruptured at the tip of a growing crack. The stress necessary to cause such rupture varies from material to material according to the type of interatomic potential function. Crack propagation in these materials is also influenced by the presence of grain boundaries, cleavage planes, etc. Therefore, these properties determine toughness, and hence the intrinsic strength, of ceramics. Practically, strengths are found to be at least two orders of magnitude less than the calculated intrinsic strengths. Griffith [45] was the first to recognize that cracks are responsible for the observed low strength in glass specimens. Griffith laid down two major precepts in his formalism of fracture mechanics: (i) equilibrium extension of well-developed cracks is governed by a balance between driving forces (associated with mechanical energy release) and resisting forces (associated with creation of crack surface area); (ii) such cracks start from flaws which act as stress concentrators in the stressed material. We shall first consider an important parameter, the stress intensity factor, K [46]. This term is a convenient parameter for characterizing a *driving* force for fracture and is introduced into the mechanics via an investigation of the manner in which a well-defined crack modifies the stress field in an elastically-loaded solid [45]: flaws in the specimens act as stress concentrators. In terms of a polar coordinate system in Fig. 2.5, solutions for the near field of crack of length c subjected to an applied loading L can be expressed in the form

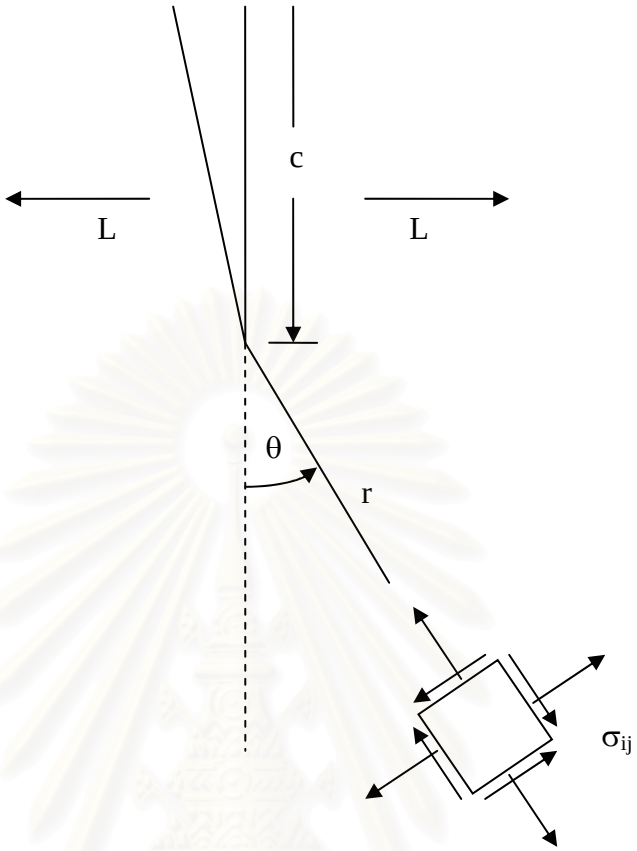

Fig. 2.5 Crack-tip fields. L and c respectively characterize the applied loading and scale of cracking[45].

$$\sigma_{ij} = K(L,c)(2\pi r)^{-1/2} f_{ij}(\theta). \qquad (2.4)$$

The most significant aspect of *K*, which can be seen from this expression, is its independence of the coordinates (r,θ). It depends only on the applied loading and crack geometry and can thereby be used to determine the intensity of the local stress field about the crack tip in terms of the boundary conditions. Accordingly, *K* is a useful indicator of the crack driving force. Moreover, it follows from Eq. (2.4) that the stress intensity factors are additive, as the principle of superposition applies within the

limit of linear elasticity theory. This additive property of K is of distinct advantage in determining the net mechanical force on the fracture system.

To analyze the crack response of a given crack loading system, one begins with the computation of an appropriate stress intensity factor in terms of an applied load L and crack length c. For example, it can be shown that shown that for an edge crack in semi-infinite plate subjected to a uniform tension σ_a (Fig. 2.6),

$$K_a = \sigma_a (\pi \Omega c)^{1/2} , \qquad (2.5)$$

where Ω is a dimensionless crack-geometry constant.

After the parameter K is established, we must then ask whether its value at a given load and crack length is sufficient to drive the crack, i.e. we need a fracture criterion. Generally, cracks may extend under either equilibrium or kinetic conditions. Equilibrium conditions are most nearly attained in high vacuum or inert environments, or at low temperatures. Under these conditions, we might reasonably expect crack extension to occur when K exceeds some critical value K_c. Thus, K_c uniquely quantifies the resistance to crack growth and this quantity has now gained the widest acceptance as a material toughness parameter in engineering design. K_c can be related to the surface energy term via the Griffith criterion for equilibrium crack extension [45]:

$$K_c = [2\Gamma E/(1-\nu^2)]^{1/2} , \qquad (2.6)$$

where Γ is the fracture surface energy, E Young's modulus and ν Poisson's ratio. It is noted that $\Gamma = \gamma$ (true reversible surface energy) for ideal brittle solids.

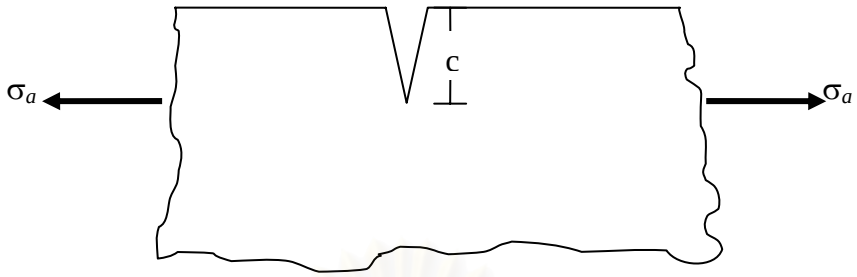

Fig. 2.6 Uniform loading configurations for edge crack in semi-infinite plate.

In cases where fracture takes place in hostile chemical environments (e.g. water), chemical processes activate bond rupture at the crack tip and the crack can therefore extend slowly in response to the environment and applied stress at *subcritical* levels, i.e. at $K < K_c$. Accordingly, the crack growth is rate controlled and the crack propagates according to a *kinetic* equation,

$$v = v(K), \qquad (K < K_c) \tag{2.7}$$

where $v(K)$, the crack-velocity function, is uniquely determined by the stress intensity factor K. This function is usually empirically determined and may have many forms. The most widely used function is of the power-law type,

$$v = v_0(K/K_c)^n, \quad (K < K_c) \tag{2.8}$$

where v_0 and n are constants depending on the given material/environment system. Generally, the $v(K)$ curve in the subcritical domain has more than one branch, corresponding to different mechanisms of rate control [47]. Three regions are commonly distinguished: (i) region I, at low K, with velocity controlled by rate of reaction between environmental species and crack-tip bonds (with the possibility of a zero-velocity threshold in K, corresponding to a fatigue limit in the strength); (ii)

region II, at intermediate *K*, a transport- controlled region where the velocity curve tends to a plateau; (iii) region III, at high *K*, a steeply – rising section of the curve, independent of the environment. Of these three regions, it is the first, which is usually the most important, since the crack kinetics is determined predominantly by the stages of slowest growth.

2.5.2 Hertzian Contact Stress Fields

Consider the frictionless contact of a sphere, radius *r*, at normal load *P*, on a flat continuum specimen, Fig. 2.7. The schematic of critical geometrical parameters is shown in Fig. 2.8. The field is initially elastic. Beyond a critical load, a Hertzian cone crack is initiated. The basic Hertzian elasticity solutions for a sphere of radius *r* at normal load *P* are well documented [42,43,48-50]. The contact radius a is given by

$$a^3 = 4k\,\mathrm{Pr}/3E\,, \tag{2.9}$$

where E is Young's modulus and $k = (9/16)[(1-\nu^2)+(1-\nu'^2)E/E']$ is a dimensionless coefficient, with ν Poisson's ratio and the prime notation denoting the indenter material [49]. The contact radius defines the spatial scale of the contact field. The mean contact pressure

$$p_0 = P/\pi a^2 \tag{2.10}$$

defines the intensity of the contact field. The maximum tensile stress in the specimen occurs at the contact circle:

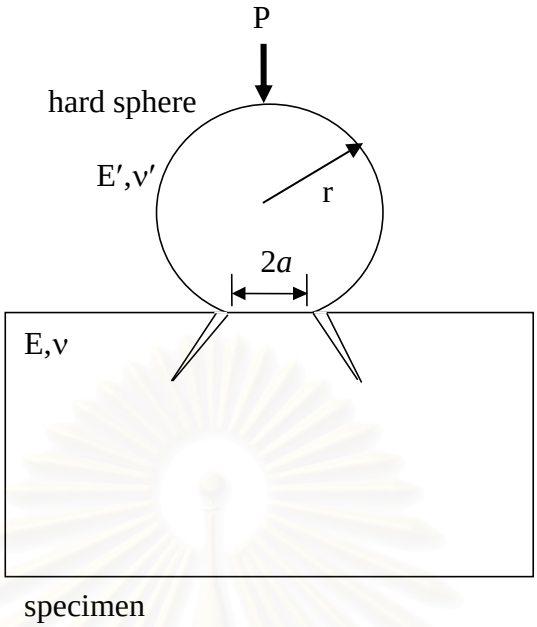

Fig. 2.7 Hertzian contact of sphere on flat glass specimen. Beyond elastic limit, contact initiates cone fracture. Courtesy of B.R.Lawn [50].

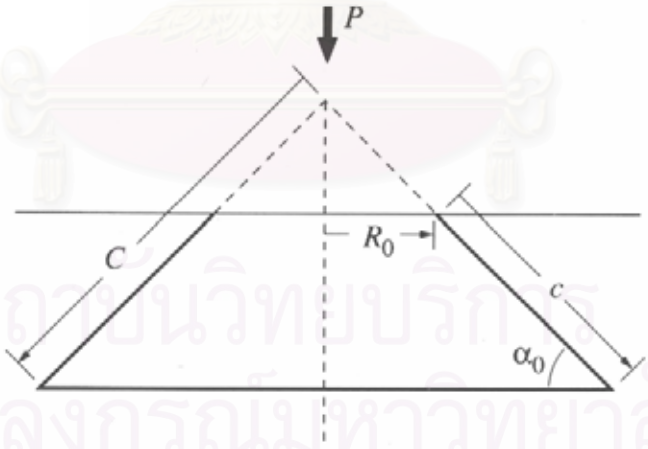

Fig. 2.8 Schematic of critical geometrical parameters of Hertzian cone fracture. Courtesy of B.R.Lawn [50].

$$\sigma_m = \frac{1}{2}(1-2\nu)p_0 \tag{2.11}$$

The maximum shear stress is located along the contact axis at a depth $\approx 0.5a$ below the surface:

$$\tau_m \approx 0.48 p_o \tag{2.12}$$

The mean contact pressure in Eq. (2.10) can be written in other useful forms by combining with Eq. (2.9). One such form expresses p_0 in terms of *a* and *r*:

$$p_0 = (3E/4\pi k)a/r \tag{2.13}$$

Equation (2.13) prescribes a linear relation between p_0,"indentation stress", and a/r,"indentation strain", leading to a procedure for obtaining basic stress-strain information[51,52]. Another useful form is given in terms of *P* and *r*:

$$p_0 = (3E/4k)^{2/3}(P/\pi r^2)^{1/3} \tag{2.14}$$

Principal normal and shear stresses are calculable solutions of the contact boundary conditions [43,53]. It is conventional to define $\sigma_1 \geq \sigma_2 \geq \sigma_3$ nearly everywhere within the Hertzian field, so that σ_1 is the most tensile principal stress and $\tau_{13} = \frac{1}{2}(\sigma_1 - \sigma_3)$ is the maximum principal shear stress. Figure 2.9 shows contours of σ_1, σ_3, and τ_{13} (σ_2 is a "hoop" stress). The σ_1 tensile stresses (shaded) in Fig. 2.9(a) concentrate in a shallow surface region, with maximum value σ_m at the contact circle (Eq. (2.11)). Included in Fig. 2.9(a) are σ_3 stress trajectories (dashed lines) from the specimen surface, defining paths always normal to σ_1 within

(a)

(b)

(c)

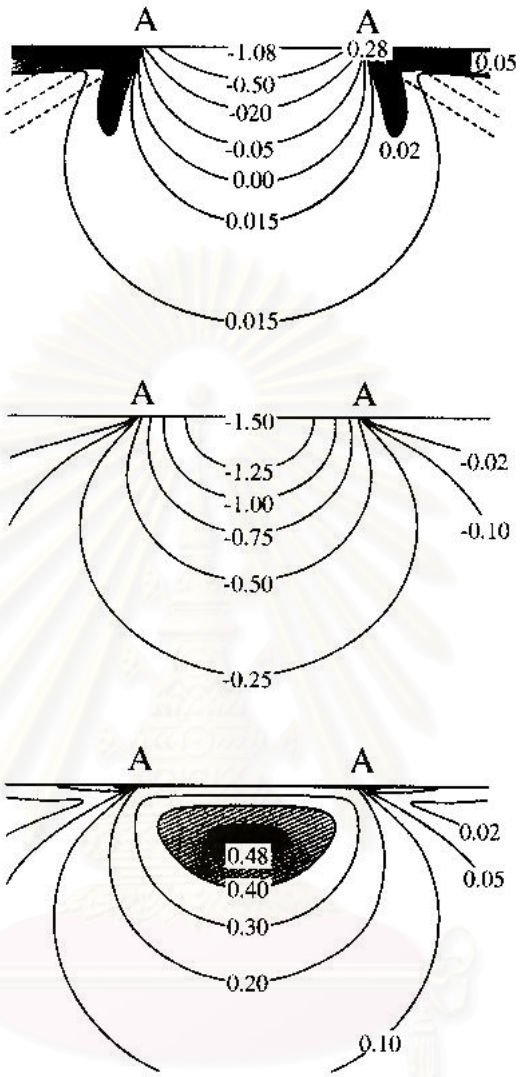

Fig. 2.9 Hertzian stress field: (a) principal normal stress σ_1, (b) principal normal stress σ_3 and (c) principal shear stress $\tau_{13} = \frac{1}{2}(\sigma_1 - \sigma_3)$. Dashed curves in (a) σ_3 stress trajectories. Stresses in unit of P_0. AA denotes contact diameter $2a$. Plotted for $\nu = 0.22$. Courtesy of B.R.Lawn [50].

the plane of the diagram. The rapid decrease of σ_1 along these trajectories is a characteristic feature of contact problems. Note that the σ_3 stresses in Fig. 2.9(b) are everywhere compressive. The principal shear stresses τ_{13} in Fig. 2.9(c) are constrained beneath the contact, with widely spaced contours and maximum value τ_m along the contact axis (Eq. (2.12)).

2.5.3 Crack Propagations in Hertzian Contact Stress Fields

Introduction of Griffith-Irwin fracture mechanics into the Hertzian fracture problem was made in 1967 by Frank and Lawn [54] with the purpose of deriving Auerbach's law* from first principles. The basic precepts of the fracture mechanics approach in the context of Hertzian fracture can be summarized as follows. Cone cracks tend to form in highly brittle solids with zero or insignificant R-curves, i.e., materials with single valued toughness, *K*. For such materials extension of any crack of length *c* under equilibrium conditions (Section 2.5.1) is determined by the simple equality $K = K_c$. If $dK/dc > 0$, the equilibrium is unstable and if $dK/dc < 0$, the equilibrium is stable. When kinetic conditions prevail, extension is determined by a crack velocity relation $v = v(K)$ (Section 2.5.1).

---

* Auerbach [55] established an empirical law between critical load for cone crack initiation P_c and sphere radius r, $P_c \propto r$.

Consider cone cracks in their well-developed state (Fig.2.8). The actual crack length *c* is related to the dimension *C* of a "virtual" cone with the tip located above the contact surface:

$$C = c + R_0 / \cos\alpha_0 , \tag{2.15}$$

where R_0 is the surface ring radius and α_0 is the cone base angle. The stress- intensity factor for this virtual cone crack system is given by [17]

$$K = \chi P / C^{3/2} , \tag{2.16}$$

where χ is a crack geometry coefficient. At $K = K_c$, we have $P \propto C^{3/2}$.

Sphere radius *r* enters Eqs. (2.15) and (2.16) only through R_0; therefore, *K* is insensitive to *r* in the region $c >> R_o$.

The mechanics of cone crack initiation is more complex. The Frank-Lawn treatment [54] addressed this issue in two key steps:

(i) The cone cracks start from flaws on the specimen top surface at (or just outside) the contact circle where the tensile stresses are concentrated. The embryonic cracks subsequently circumvent the contact circle as a shallow surface ring, then propagate downward and outward, closely (but not exactly) following the σ_3 trajectories (so as to be nearly normal at all points to the σ_1 tensile stresses) in the prior stress field (Fig. 2.9(a)).

(ii) A stress- intensity factor for the downward crack extension can be expressed uniquely in terms of the prior stress function $\sigma_1(s)$ where *s* is a coordinate along the σ_3 trajectory. The stress-intensity factor has the form

$$K(c/a) = P_0 a^{1/2} I(c/a, \beta, \nu) , \tag{2.17}$$

where $\beta = R_0 / a$ is the relative crack location and $I(c/a, \beta, \nu)$ is the dimensionless integral

$$I(c/a, \beta, \nu) = 2(c/\pi a)^{1/2} \int_0^{c/a} [\sigma_1(s/a, \beta, \nu)/p_0] d(s/a)/(c^2/a^2 - s^2/a^2)^{1/2} . \quad (2.18)$$

Figure 2.10 sketches the normalized function $K(c/a)/K_c$ for a sequence of increasing loads ($P' \rightarrow P'' \rightarrow P'''$). The function has two unstable branches (1,3) and two stable (2,4) branches. Suppose the specimen contains surface flaws within the range $c < c_f < c^*$ and that equilibrium conditions prevail. Then the crack evolves along the configurational path marked by the arrows, growing stably with load along $K/K_c = 1$ until a critical penetration depth $c = c^*$ is reached, therefore the full cone crack pops in and arrests on branch 4. Inserting $I^* = I(c^*/a) = constant$ and using Eqs. (2.9) and (2.10) to eliminate p_0 and *a* in Eq. (2.17), we obtain critical condition for cone initiation:

$$P_c / r = AK_c^2 / E = \text{constant} \quad (2.19)$$

where $A = 4\pi^2 k / 3I^{*2} = \text{constant}$. Equation (2.19) is a formal statement of Auerbach's law.

The requirement that surface flaws must first grow to depth c^* before propagating into the full cone renders P_c independent of c_f in Eq. (2.19), consistent with the test results on variously abraded glass surfaces [56]. For very small flaws in the range $c_f << c_0$, or for very large spheres (large *r*, large *a*) the initiation is spontaneous from branch 1 to branch 4. Interestingly, for very large flaws in the range $c_f >> c^*$ it can become increasingly difficult to initiate cone cracks at all, because of

difficulties in accommodating the crack to the curved stress trajectory paths of maximum tension [56-58].

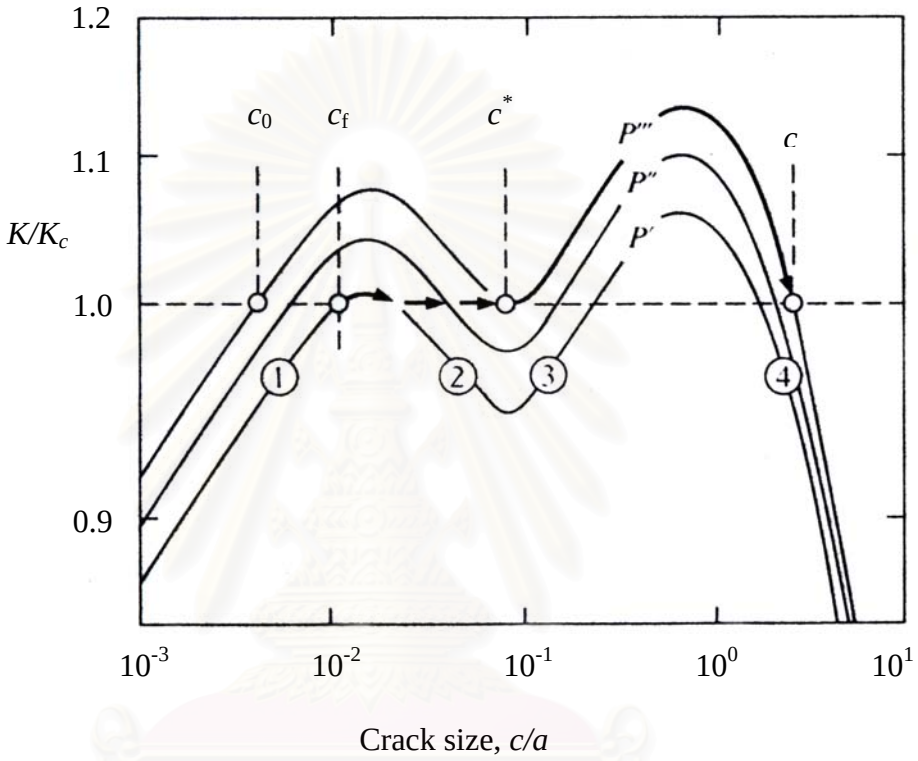

Fig. 2.10 Normalized *K(c)* curves for Hertzian fracture ($\beta = 1$ and $\nu = 0.3$). Arrows indicate evolution from surface flaw to full cone crack. Courtesy of B.R.Lawn [44].

CHAPTER III

EXPERIMENTAL PROCEDURE

3.1 Young's Modulus Measurement

3.1.1 Exploratory Investigation

Exploratory investigations were made to find out which commercially available adhesives having a broad range of Young's modulus were, so they would be chosen to be used in our work. We started with specimen preparation for tests by squeezing out each commercial adhesive into a mould made simply from paper of dimension 4x10x100 mm and leaving it to set fully for an overnight. Then each specimen was pressed and bent by hands. It is found that silicone sealant (DEECO) is the softest and was the easiest to get bent, whereas steel epoxy resin (Pattex-Duro E-POX-E Steel Filler) is the hardest and cannot be bent by hands. So we chose silicone sealant and steel-epoxy resin as well as epoxy resin (Loctite-Duro E-POX-E glue) for further tensile tests to evaluate their Young's moduli. The epoxy resin was also chosen because it was used as an adhesive interlayer of the trilayer systems used in the previous works [32,33].

Though a three-point bending test is the simplest and the most suitable to be used to measure the Young's modulus of glass and can be used to measure those of steel-epoxy resin and epoxy resin, it is not suitable to be used to measure that of silicone sealant. Silicone sealant specimen is too soft for the three-point bending test.

Therefore, the tensile test is chosen to measure Young's modulus of the three adhesives, whereas the three-point bending test is used to measure Young's modulus of glass.

3.1.2 Tensile Test

All the three types of the chosen adhesives, namely steel-epoxy resin, epoxy resin and silicone sealant were prepared in bar shape of dimension 4x10x100 mm by the same preparation method as described in Section 3.1.1. The specimen was then installed in the grips of the universal testing machine (Instron 4502). The schematic and photograph of experimental set up of the tensile test are shown in Fig. 3.1 and Fig. 3.2, respectively. The original distance between gage marks was 50 mm. The crosshead of the Instron testing machine was then moved up, and the load was applied at a constant speed of 50 mm/min. The load and deformation were noted simultaneously. The extension readings could be taken from the Instron machine scale.

The Young's modulus was calculated by extending the initial linear portion of the load-extension curve and dividing the difference in stress corresponding to any segment of section on this straight line by the corresponding difference in strain. The Young's modulus value would be computed using the slope in the linear of stress-strain diagram.

The stress and strain were calculated from [59]

$$\sigma = P/A \tag{3.1}$$

and

$$\varepsilon = \Delta L/L_0 = (L-L_0) / L_0, \tag{3.2}$$

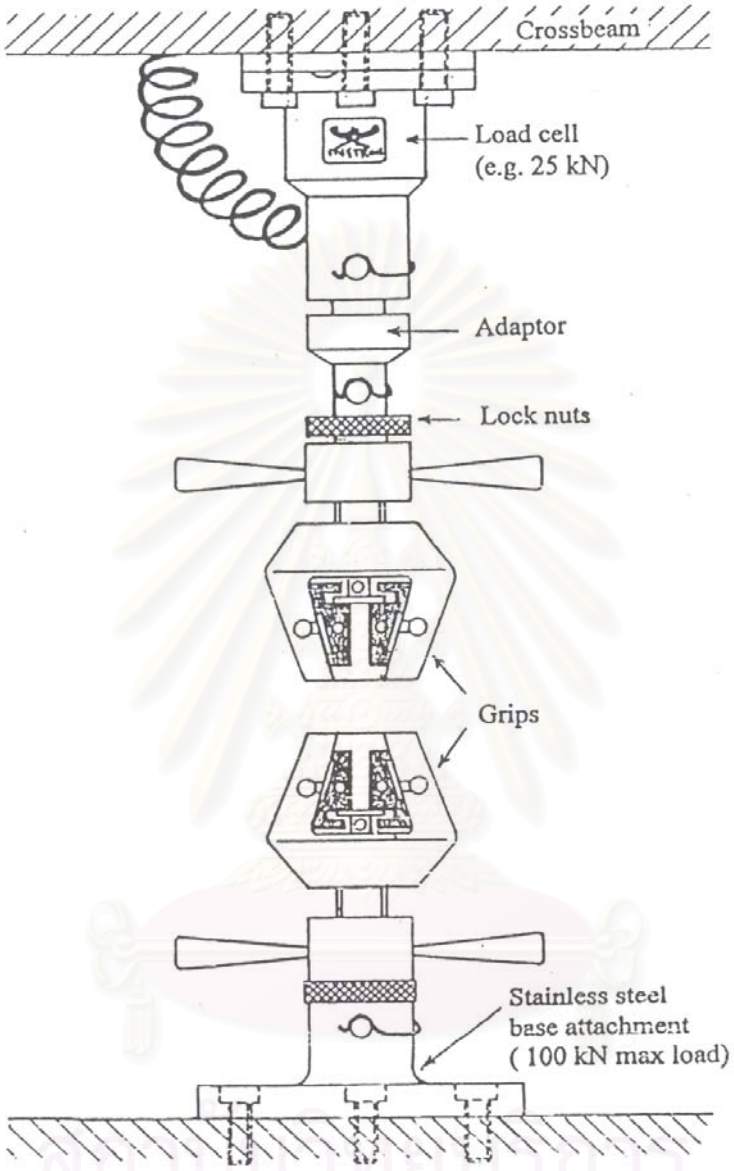

Fig. 3.1 Schematic diagram of tensile test set up.

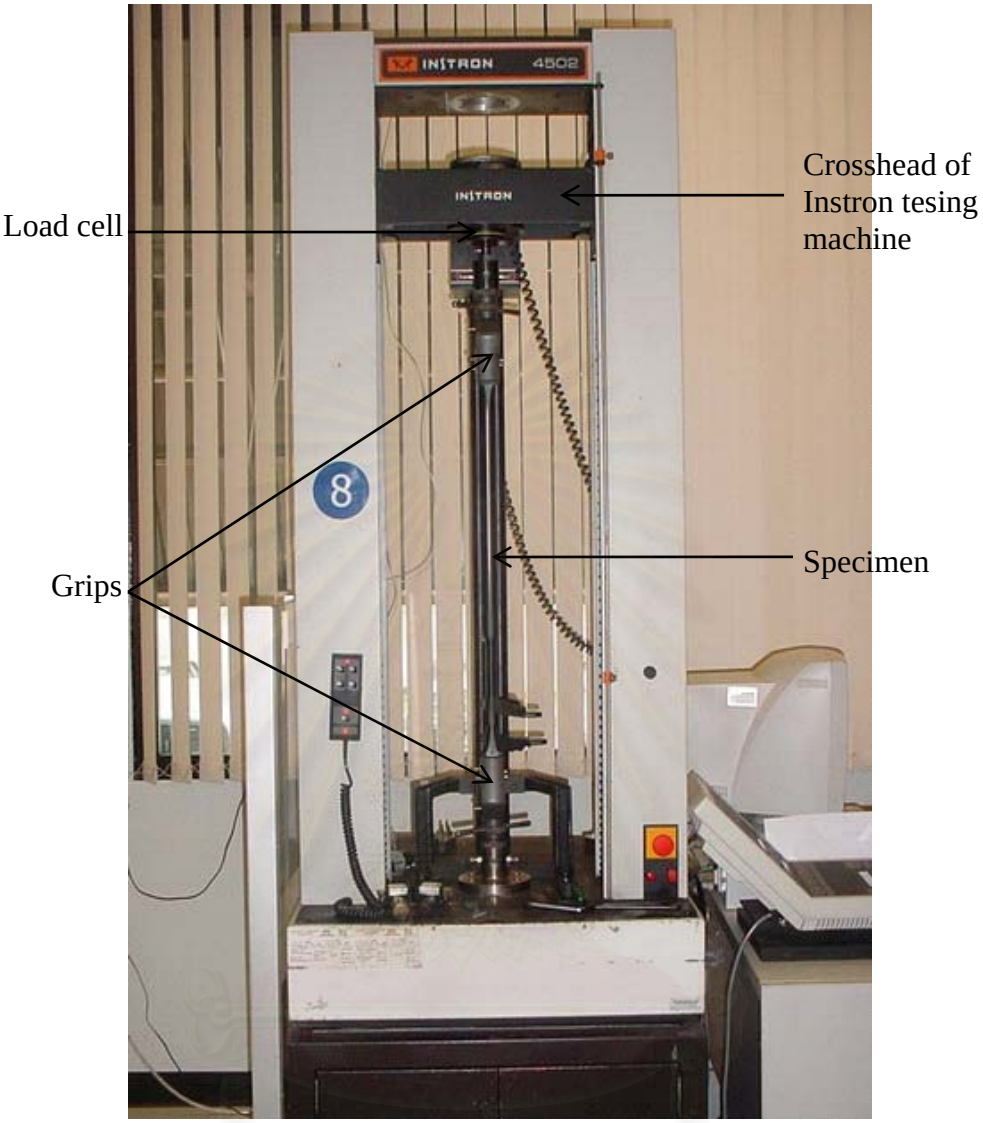

Fig. 3.2 Photograph of tensile test set up in Instron testing machine.

where σ = Stress (Pa),

P = Load (N),

A = Cross-sectional area (m^2),

ε = Strain,

L = Distance between gage marks,

L_0 = Original distance between gage marks,

and $\Delta L = (L-L_0)$ = Increment of distance between gage marks = elongation.

3.1.3 Three-Point Bending Test

For glass, the elastic modulus of glass is usually determined with specimens loaded by bending because deflection is measured more easily than very small elongations [34]. Small rods (beams) with circular or square cross-section are common, though tubes or plates are also sometimes used. A conventional test machine for strength measurements may be used. The deflection is measured with a scale microscope or by means of a suitable electrical or mechanical sensor. Thus, three-point bending test was chose to measure the Young's Modulus of glass.

When the perpendicular load P acts at the center of a specimen lying on two supports (Fig. 3.3), Young's modulus is determined from the expression [34]

$$E = \frac{PL^3}{48Jy} \quad , \tag{3.3}$$

where L is the distance between the supports, y is the deflection of the specimen below the load, and J is the moment of inertia of the cross-section. For a rectangular cross-section [34],

$$J = \frac{bh^3}{12} \quad , \tag{3.4}$$

where b is the width of the specimen, and h is its height in the direction of deflection. So, the formula for obtaining the Young's modulus is

$$E = \left(\frac{P}{y}\right)\frac{L^3}{4bh^3} \quad , \tag{3.5}$$

where $\frac{P}{y}$ is the slope of the elastic portion of the load-deflection curve.

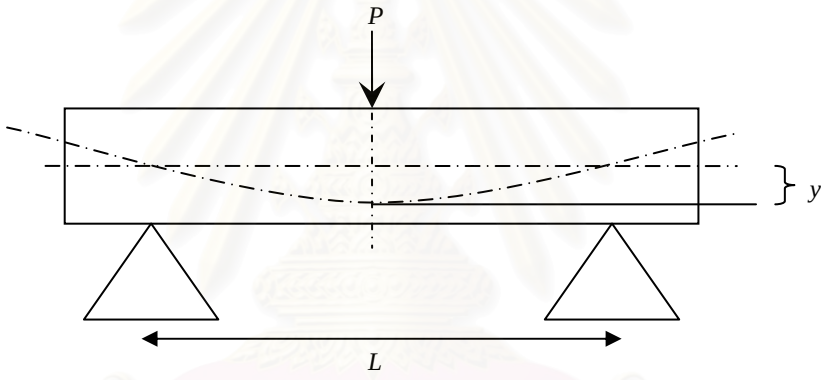

Fig. 3.3 Measurement of Young's modulus with three-point bending

Soda-lime glass was cut into bars of 2.5x10x100 mm, and the three-point bending test was performed by the use of universal testing machine (Instron 4502). The schematic and photograph of experimental set up of the three-point bending test are shown in Fig. 3.4 and Fig. 3.5, respectively. The specimen was placed on the fixed roller to the fixed supports, and the distance between the supports is 40 mm. The rate of crosshead motion at 1.27 mm/min was used. Reading of load and deflection were recorded by the Instron machine scale, while the crosshead was moving down.

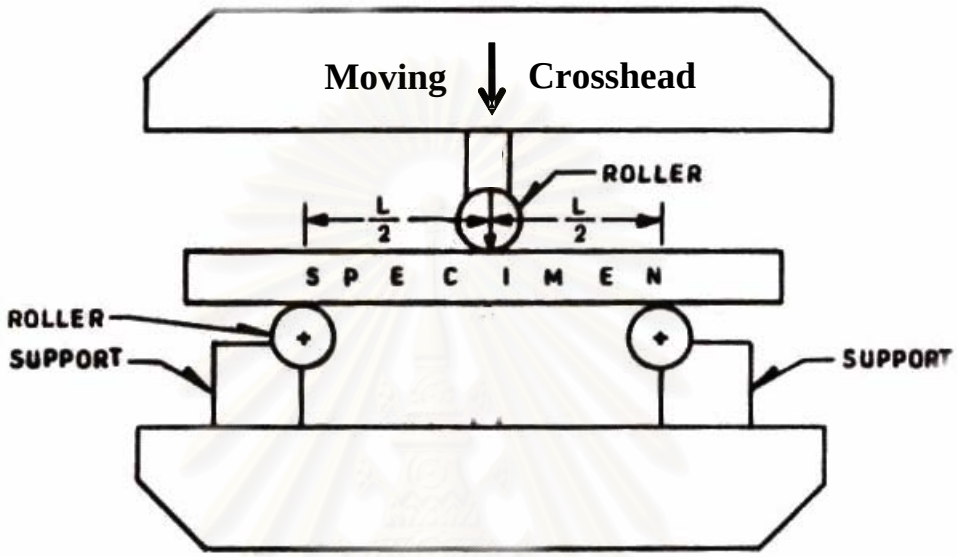

Fig. 3.4 Schematic of experimental set up for 3-point bending test. Courtesy of K. Singh [60].

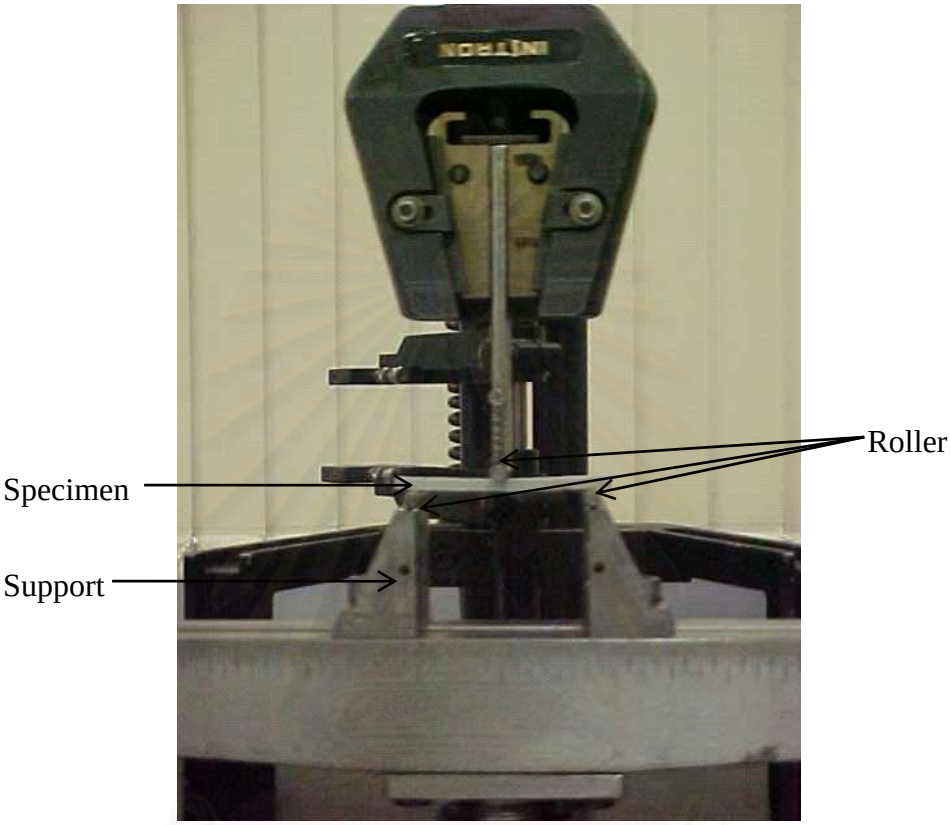

Fig. 3.5 Photograph of experimental set up for 3-point bending test.

3.2 Specimen Preparation

In this thesis, the model layer structures consisting of glass plate coating glued to thick glass substrate with 3 adhesive polymers, namely steel – epoxy resin, epoxy resin and silicone sealant were constructed. We used a model system to examine the role of adhesive interlayer on fracture modes of brittle layer structures by using spherical indentation. The ratio of thicknesses of glass overlayer and adhesive layer were d/h = 50 (d = 1000 μm, h = 20 μm), 25 (d = 500 μm, h = 20 μm), 5 (d = 1000 μm, h = 200 μm) and 2.5 (d = 500 μm, h = 200 μm). However, the bulk glass specimen was also prepared in order to observe fracture patterns produced by Hertzian indentation as a reference.

To form the layer structures, the top surface of the glass plate substrate (5.8 mm) and the bottom surface of the glass plate coating (2.5 mm) were polished by 1μm diamond suspension. Then, these plates were cleaned with distilled water and dried in hot air. The following procedure to bond the glass overlayer onto glass underlayer was carried out (Fig. 3.6): (i) set overlayer and underlayer plate on the clamp, placed them on the opposite sides; (ii) apply each adhesive polymer to capillarity between overlayer and underlayer; (iii) bond these layers together by applying slightly compressive force so as to control the interlayer thickness for the resultant h ≈ 20 μm. Then, the layers were clamped and left for 24 hours in air. The adhesive thickness h ≈ 200 μm was controlled by inserting double-sided sticky tape having thickness of 200 μm at the specimen interface ends. Each adhesive polymer was applied to capillarity between overlayer and underlayer. Then, the layers were clamped and left for 24 hours in air (Fig. 3.7).

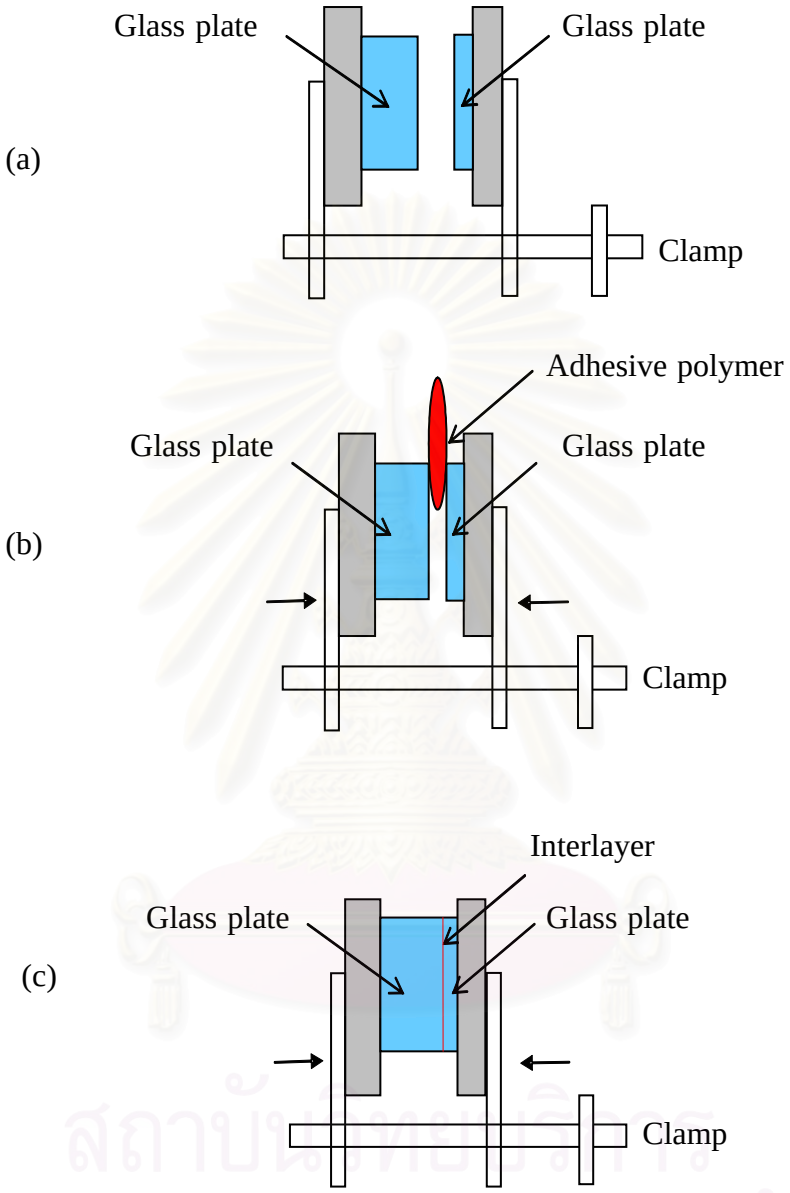

Fig. 3.6 Schematic bonding procedure used to prepare layer structure: (a) set the glass plates on the clamp; (b) apply the adhesive polymer to the capillarity; (c) bond the plates together. Note that the bond interlayer of thickness ≈ 20 μm.

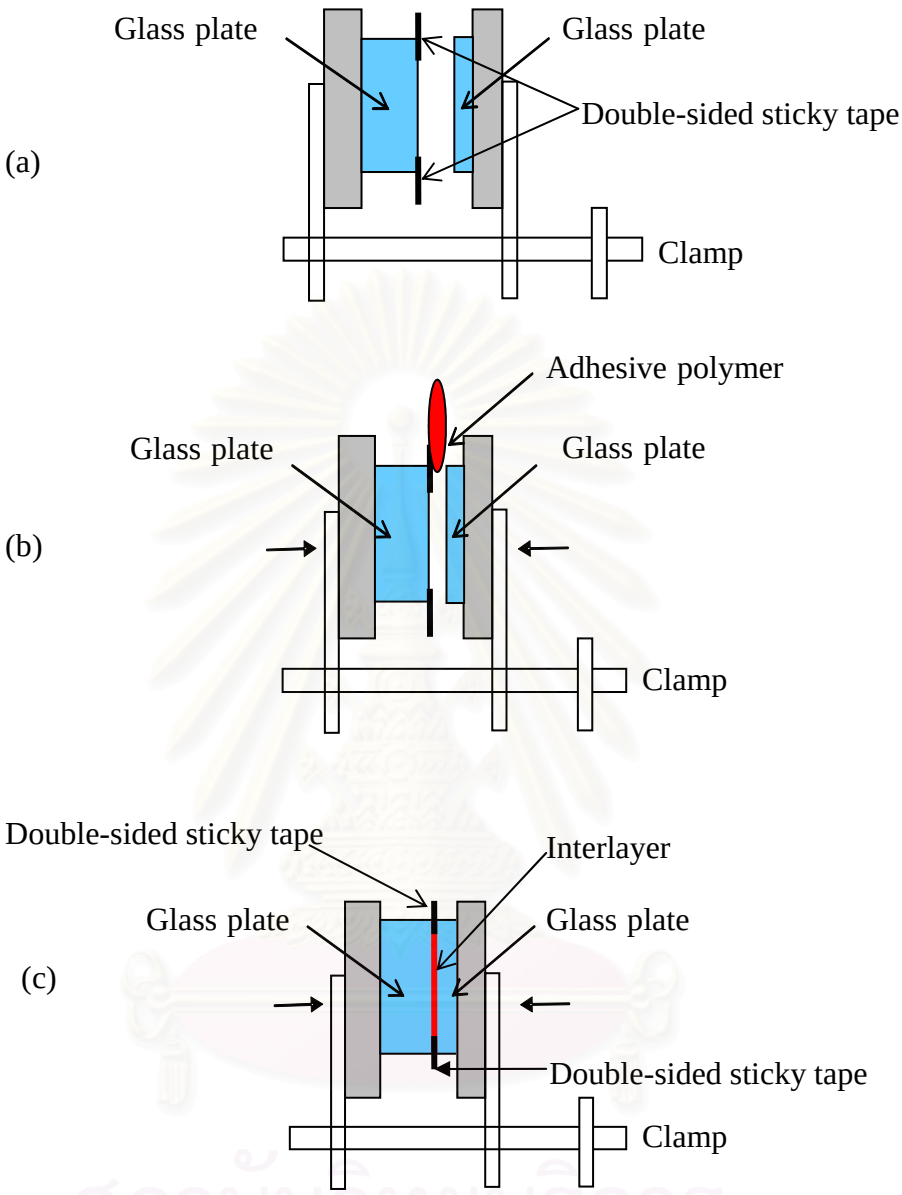

Fig. 3.7 Schematic bonding procedure used to prepare layer structure: (a) set the glass plates with inserting double-sided sticky tape having thickness of 200 μm at the specimen interface ends on the clamp; (b) apply the adhesive polymer to the capillarity; (c) bond the plates together. Note that the bond interlayer of thickness ≈ 200 μm.

After that, the layer structures were cut into sizes 3 mm x 25 mm x 8.32 mm for the specimens with interlayer thickness = 20 μm and 3 mm x 25 mm x 8.50 mm for the specimens with interlayer thickness = 200 μm. The bulk glass specimen was cut into bars 3 mm x 25 mm x 5.8 mm. The schematic of the glass/adhesive polymer/glass specimens is shown in Fig. 3.8.

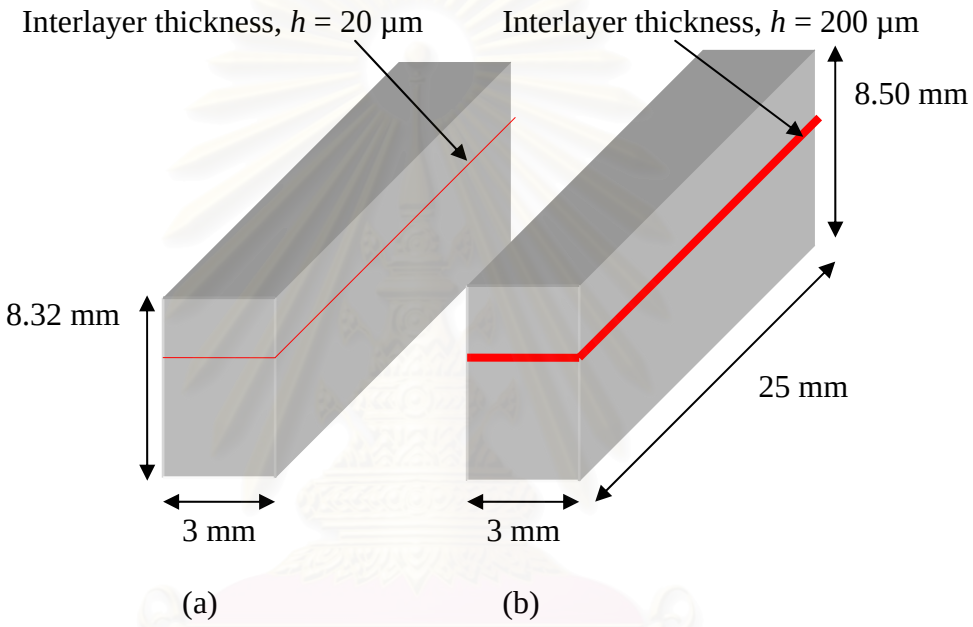

Fig. 3.8 Schematic of the glass/adhesive polymer/glass specimens: (a) specimen with interlayer thickness = 20 μm; (b) specimen with interlayer thickness = 200 μm.

3.3 Spherical Indentation Test: The Bonded-Interface Technique

Hertzian indentation techniques together with bonded-interface techniques are used to observe the damage pattern of blunt indentation beneath surface. The bonded-interface technique is illustrated for a bulk specimen in Fig. 3.9. Two half-specimens with polished surface are bonded face-to-face under clamping pressure. The

indentation test surface which is perpendicular to the bonded interface is grounded and polished. Indentations are made across the interface trace at the test surface. After indentation, the specimen halves are separated. Then, the reflection optical microscopy is used to examine the subsurface deformation and fracture pattern in section view.

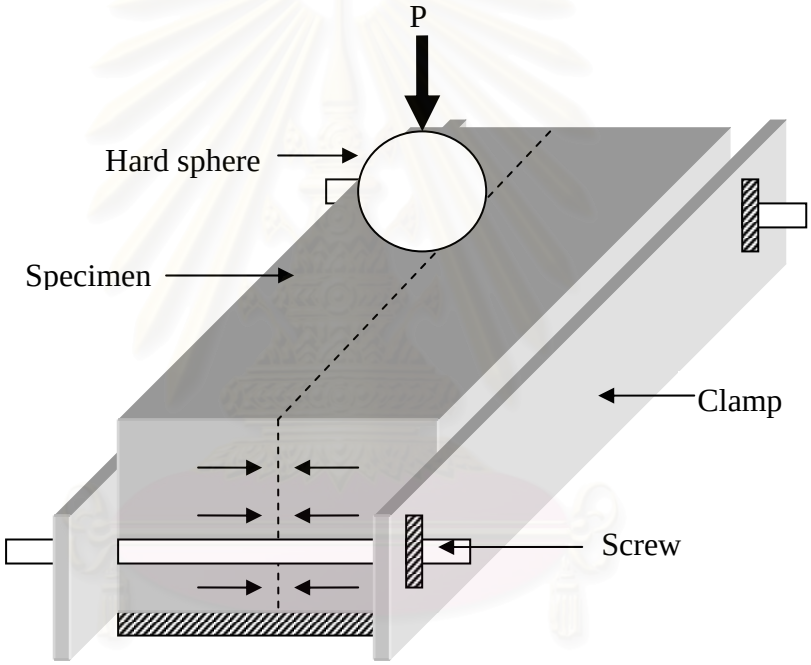

Fig. 3.9 Schematic Hertzian indentation test on top surface of bonded-interface specimen. Specimen consists of two polished halves bonded across the interface.

In this work, in order to be able to observe its deformation/fracture patterns produced by the spherical indentation, the preexisting damages on specimen surfaces have to be removed by grinding and polishing with successively finer abrasive powders to obtain an optical finish. For the bulk glass specimens, two half-specimen sides were ground and polished with a series of SiC paper (320, 600, 800, 1200, 2500, 4000 mesh) and a series of diamond suspension (6, 3, 1 μm). After that, two of the polished half specimens were placed on metal plate and joined together by clamp. Then the top surface of bonded-interface specimen was polished to 1 μm finish. For layer specimens consisting of interlayer thickness h = 20 and 200 μm, the half-layer specimens were ground and polished with a series of SiC paper (320, 600, 800, 1200, 2500, 4000 mesh) and a series of diamond suspension (6, 3, 1 μm). Two of the polished half specimens were placed on metal plate and joined together with clamp. Then the bonded-interface specimens were polished on the top glass surfaces to the required thickness, d, about 1000 and 500 μm with the same grinding and polishing procedure. The top layer thickness should be accurate; this thickness from one edge to the other could have a slightly error (≤ 50 μm).

A sequence of indentations was subsequently made along the bonded-interface trace on the test surfaces of the trilayer specimen, with tungsten carbide (WC) sphere of radius r = 1.59 mm by using a screw-driven testing machine (Instron 4502) in air, taking special care to keep the contacts centered across this trace, and applying a clamping stress normal to the interface to minimize intersurface separation. After indentation, the specimen halves were separated. Then, the reflection optical microscopy was used to examine the fracture pattern in section view. The bonded-interface technique in layered structure is shown in Fig. 3.10.

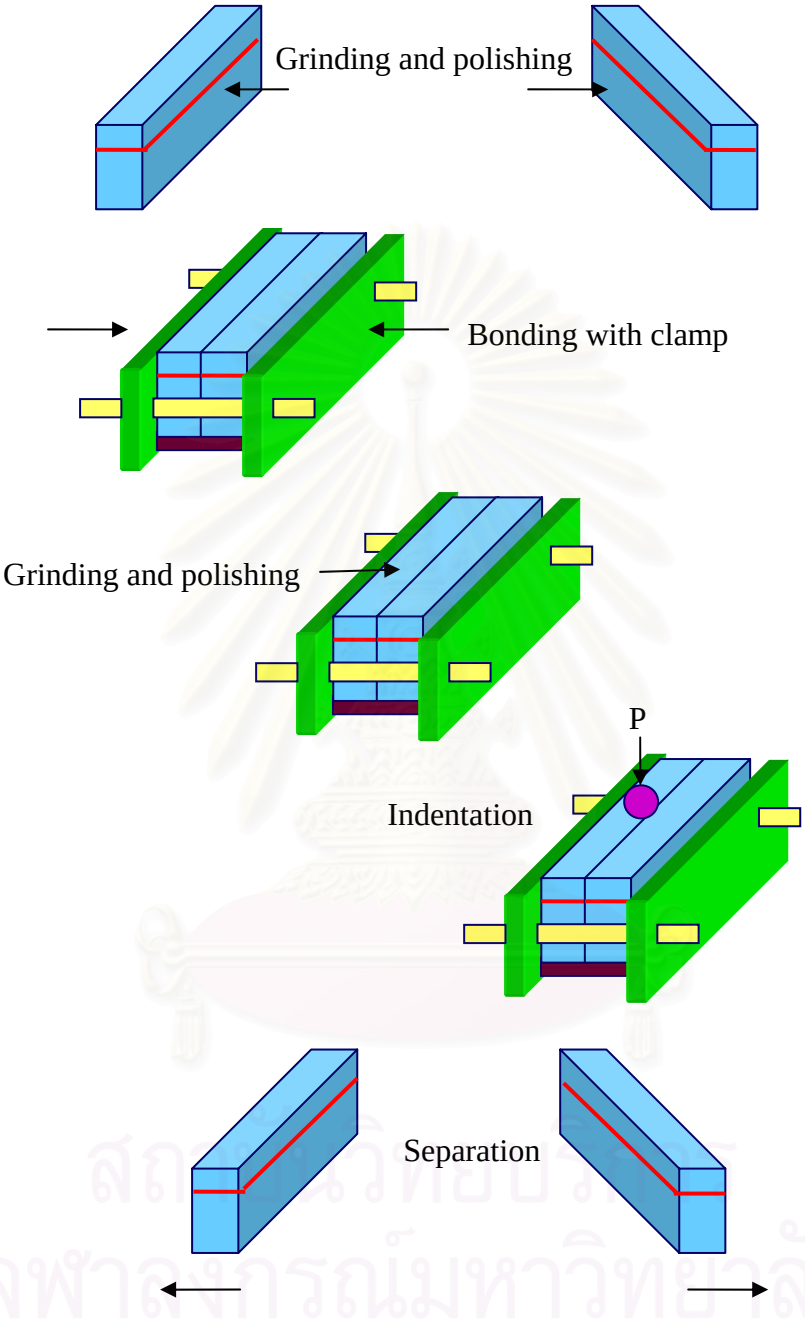

Fig. 3.10 Schematic of the bonded-interface technique

CHAPTER IV

RESULTS

4.1 Young's Modulus of Adhesive Polymers and Glass

The stress-strain data obtained from the tensile tests of steel-epoxy resin specimens, epoxy resin specimens and silicone sealant specimens are plotted as shown in Figs. 4.1, 4.2 and 4.3, respectively. The Young's modulus values were computed from the slope in the linear region of stress- strain plots.

The load-deflection curve of each glass specimen from the three-point bending test is illustrated in Fig. 4.4. The formula used to calculate the Young's modulus of glass specimens is Eq. (3.5). So, calculating the slope of load-deflection plots and plugging it and the parameters in Eq. (3.5) lead to the Young's modulus.

The obtained Young's modulus of each adhesive polymer and glass are shown in Table 4.1.

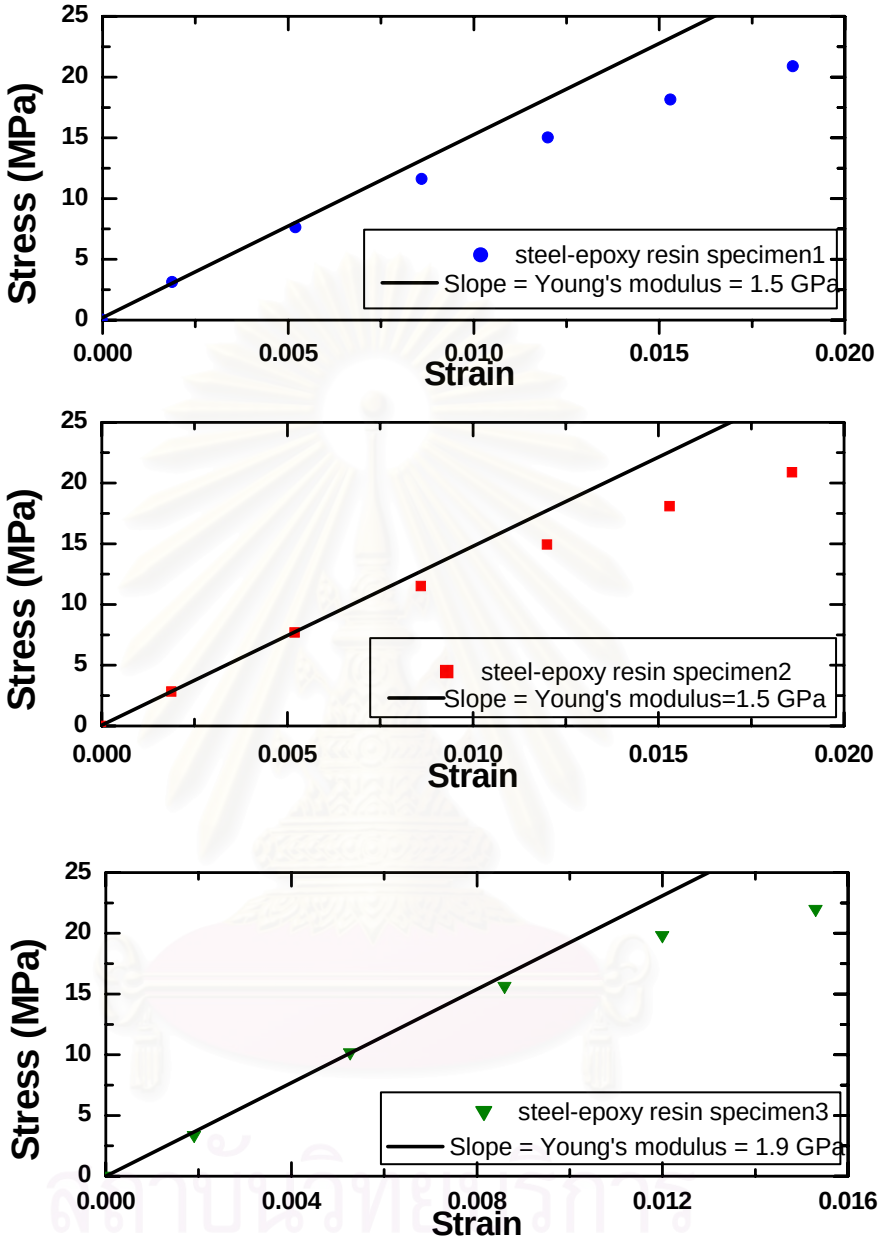

Fig. 4.1 Stress-strain diagram of 3 specimens of steel-epoxy resin by tensile test. Note the slopes represent Young's modulus.

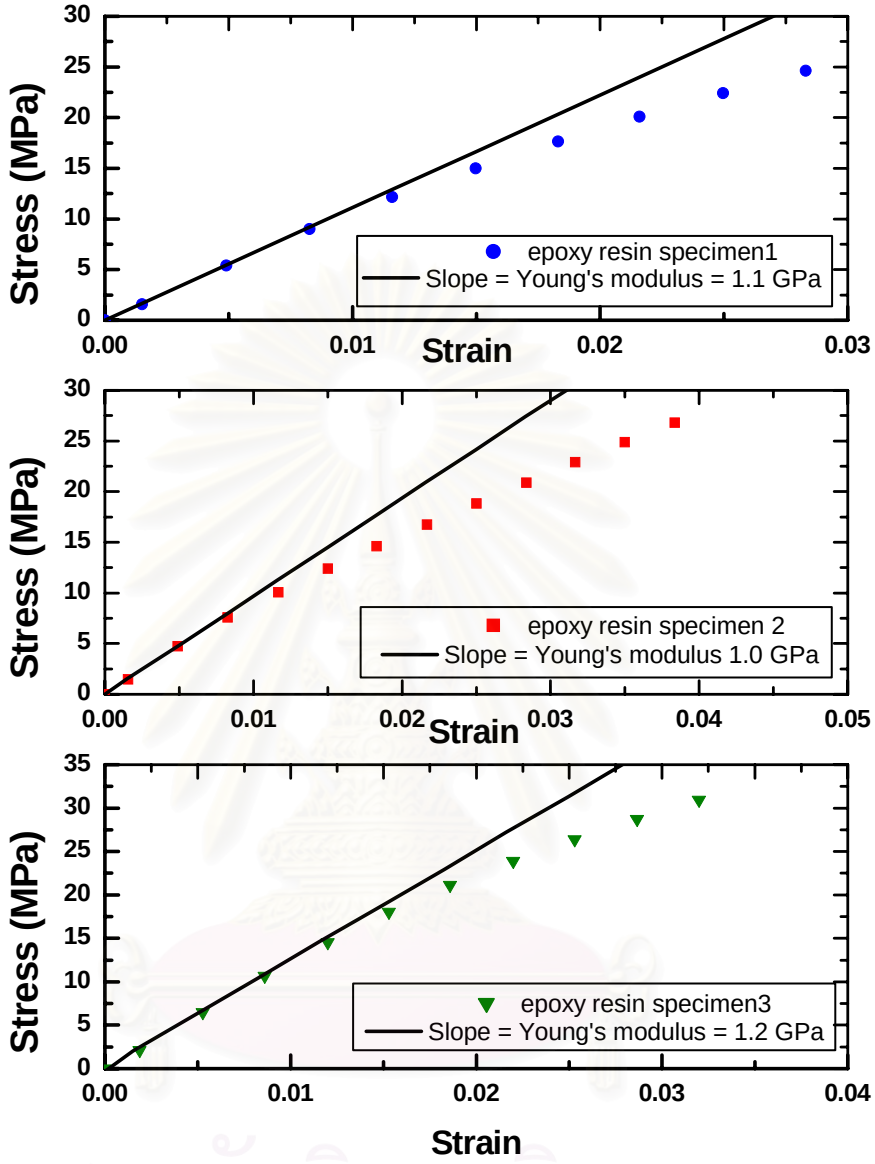

Fig. 4.2 Stress-strain diagram of 3 specimens of epoxy resin by tensile test. Note the slopes represent Young's modulus.

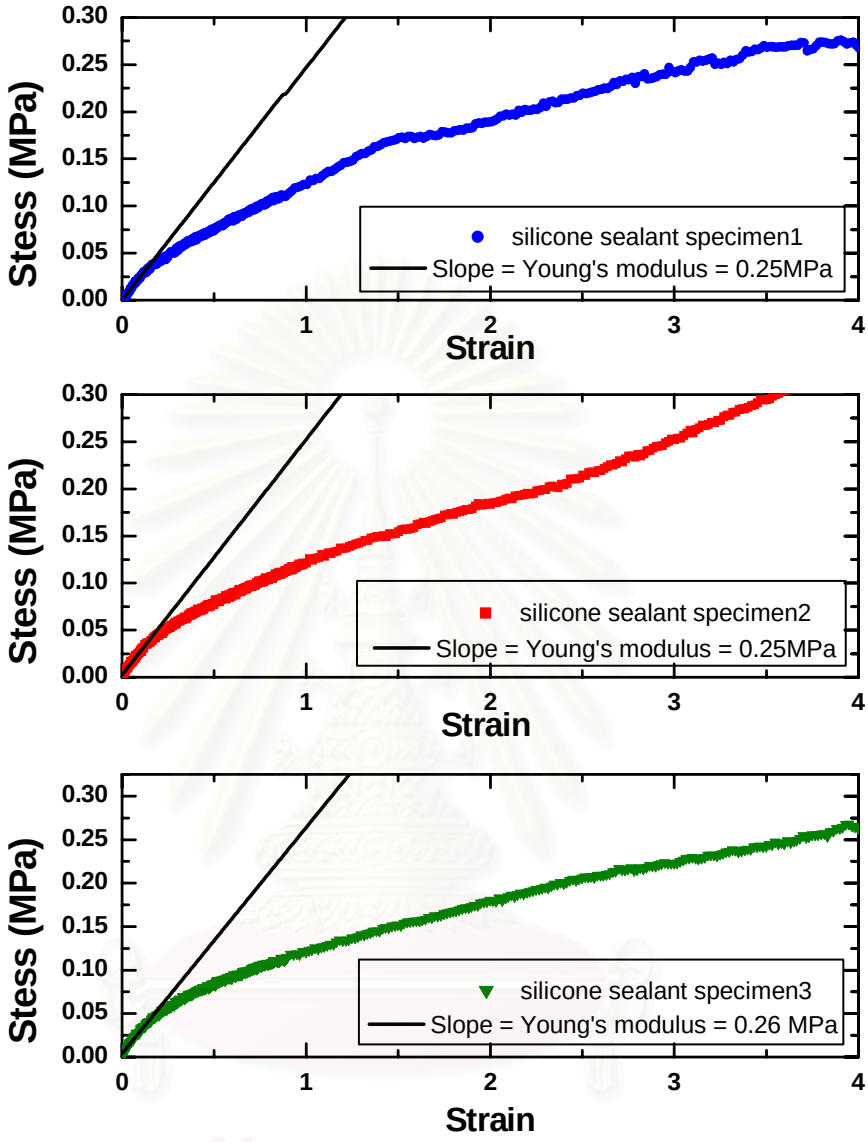

Fig. 4.3 Stress-strain diagram of 3 specimens of silicone sealant by tensile test. Note the slopes represent Young's modulus.

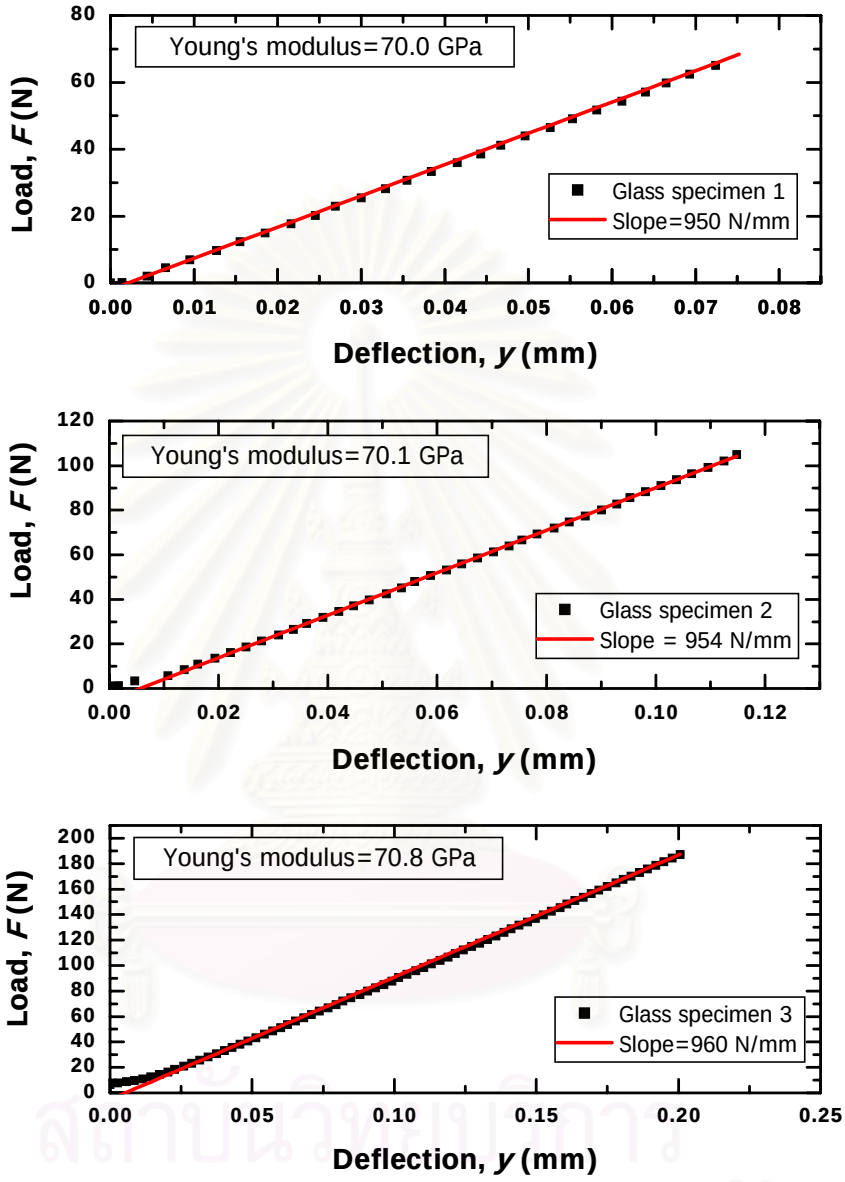

Fig. 4.4 The load-deflection curve of 3 glass specimens by three-point bending test

Table 4.1 Young's moduli of adhesive polymers by tensile test and Young's modulus of glass by three-point bending test

Materials Combination	Average Young's Modulus *E* (GPa)
Steel-Epoxy Resin	1.6 ± 0.2
Epoxy Resin	1.1 ± 0.1
Silicone Sealant	$(2.5 \pm 0.1) \times 10^{-4}$
Glass	70.3 ± 0.4

4.2 Damage Patterns of Glass/Steel-Epoxy Resin/Glass System

The Hertzian indentation fractures, in which their subsurface profiles were revealed by the bonded interface technique (see Section. 3.3), are shown in Figs. 4.5 and 4.6. Figure 4.5 shows a Hertzian indentation damage in glass/steel-epoxy resin/glass system with the coating thickness of 1000 μm bonded with the steel-epoxy resin of thickness h = 20 μm, using a WC sphere of radius r = 1.59 mm. The indentation load P = 250 N. It can be seen that the damage is evident as a ring crack on the top surface of the coating layer (see Fig. 4.5 (a)) while a cone crack, which penetrates into the coating layer, is evident on the side view of the layered system obtained from the bonded-interface technique (see Fig. 4.5 (b)).

Figure 4.6 illustrates the response of Hertzian contact in bulk glass (see Fig. 4.6(a)) in comparison with the glass/steel-epoxy resin/glass system for two coating thicknesses, d = 1000 μm (see Fig. 4.6 (b)) and 500 μm (see Fig. 4.6(c)), bonded with the same steel-epoxy resin of thickness h = 20 μm, due to a WC sphere of radius r = 1.59 mm at fixed P = 200 N. The cone cracks occur in subsurface of coating layer in a similar manner as in the bulk glass, but the length of cone cracks are unequal. Cone crack length in bulk glass is the shortest, and the longest crack length occurs in the layered system of coating thickness d=500 μm.

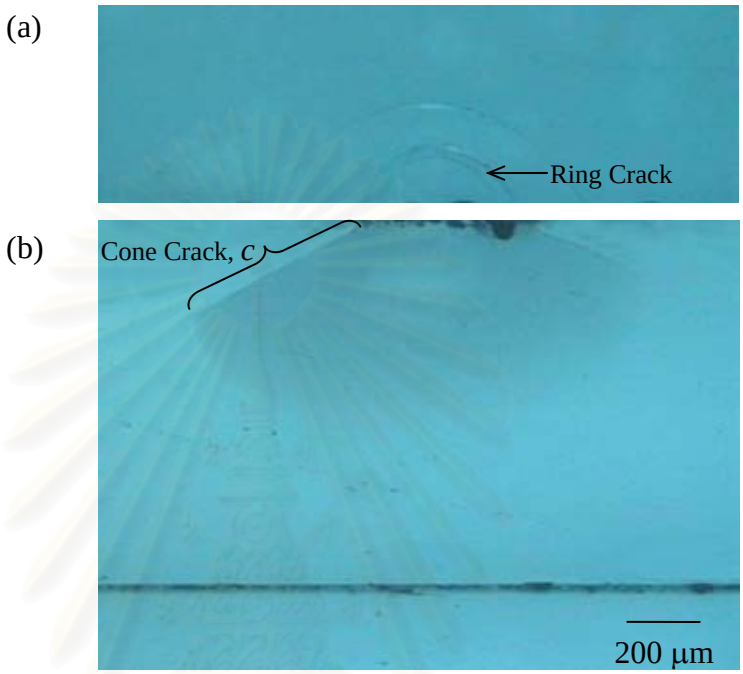

Fig. 4.5 Contact fracture in glass/steel-epoxy resin/glass system, with soda-lime glass coating thickness d = 1000 μm bonded with steel-epoxy resin of thickness h = 20 μm, using a WC sphere of radius r = 1.59 mm at P = 250 N; where c is the crack length: (a) top view; (b) side view.

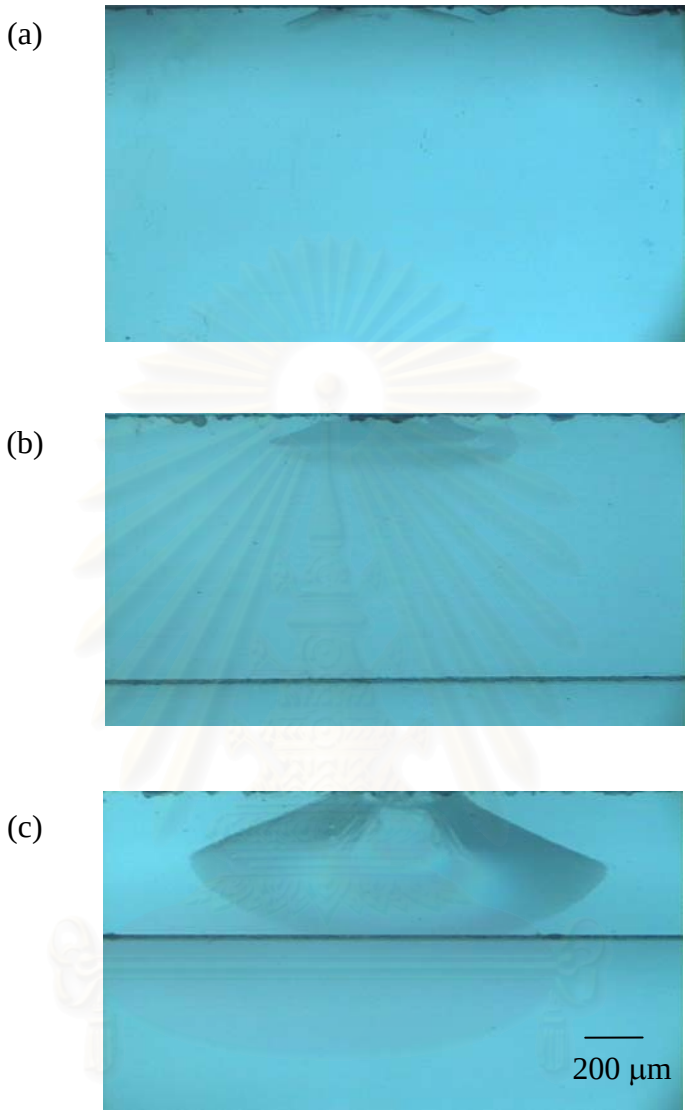

Fig. 4.6 Contact fracture in bulk glass in comparison with the glass/steel-epoxy resin/glass system for two coating thicknesses, d = 1000 and 500 μm, bonded with the same steel-epoxy resin of thickness h = 20μm, due to a WC sphere of radius r = 1.59 mm at fixed P = 200 N: (a) cone crack in bulk glass; (b) cone crack in layer system of coating thickness d=1000 μm; and (c) cone crack in layer system of coating thickness d=500 μm.

4.2.1 Effect of Indentation Load

Figure 4.7 from bonded-interface specimens, it shows the effect of indentation load on Hertzian contact damages on the glass/steel-epoxy resin/glass system, with the coating thickness of 1000 μm bonded with steel-epoxy resin of thickness h = 20μm. The indentation loads P are 100, 150, 200 and 250 N. In this layer system, the adhesive bonding is strong enough to preclude delamination. It can be seen from the micrographs in Fig. 4.7 that cone cracks are obtained only within the coating layer for every indentation load. The cone crack initiated at the top coating surface at P = 100 N extends downward into the coating layer (see Fig. 4.7 (a)). At P = 150 N, the cone crack develops much further in its length than the cone crack due to P = 100 N (see Fig. 4.7 (b)). Its length increases at higher P values (see Figs. 4.7(c) and (d)). The cone crack length c as a function of indentation load is shown in Fig. 4.8.

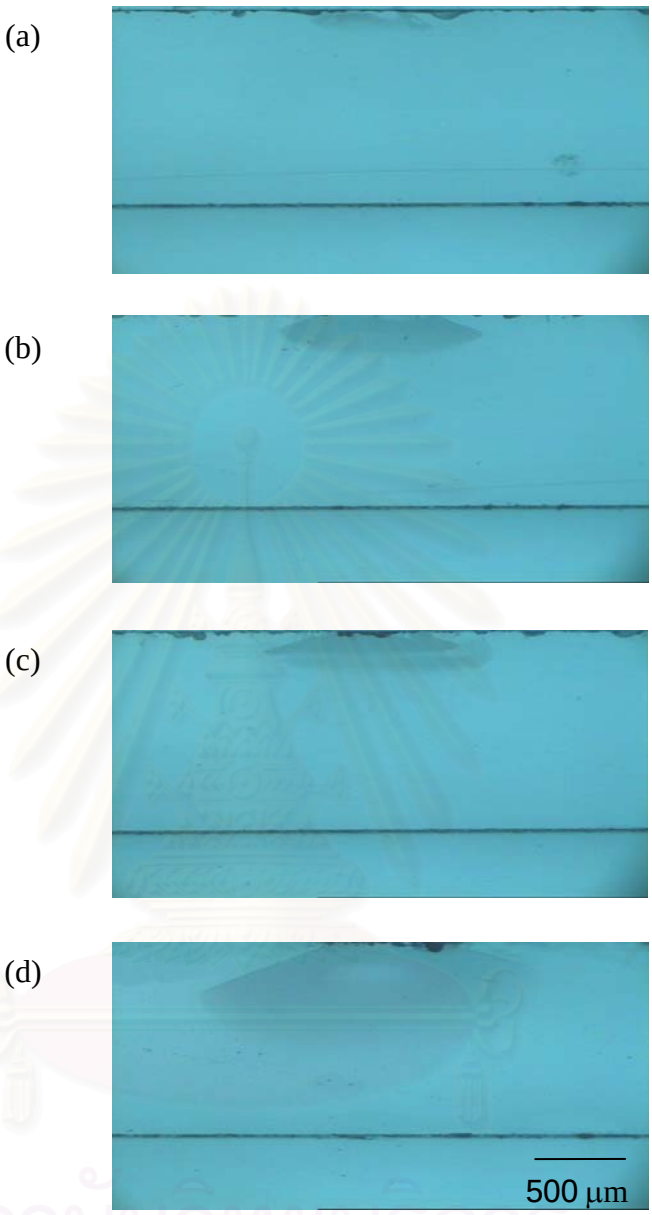

Fig. 4.7 Contact fracture in glass/steel-epoxy resin/glass system, with soda-lime glass coating thickness d = 1000 μm bonded with steel-epoxy resin of thickness h = 20 μm, using a WC sphere of radius r = 1.59 mm. It demonstrates the effect of indentation load: (a) P = 100 N; (b) P = 150 N; (c) P = 200 N; and (d) P = 250 N. Note that the cone crack length increases, as the load is increasing.

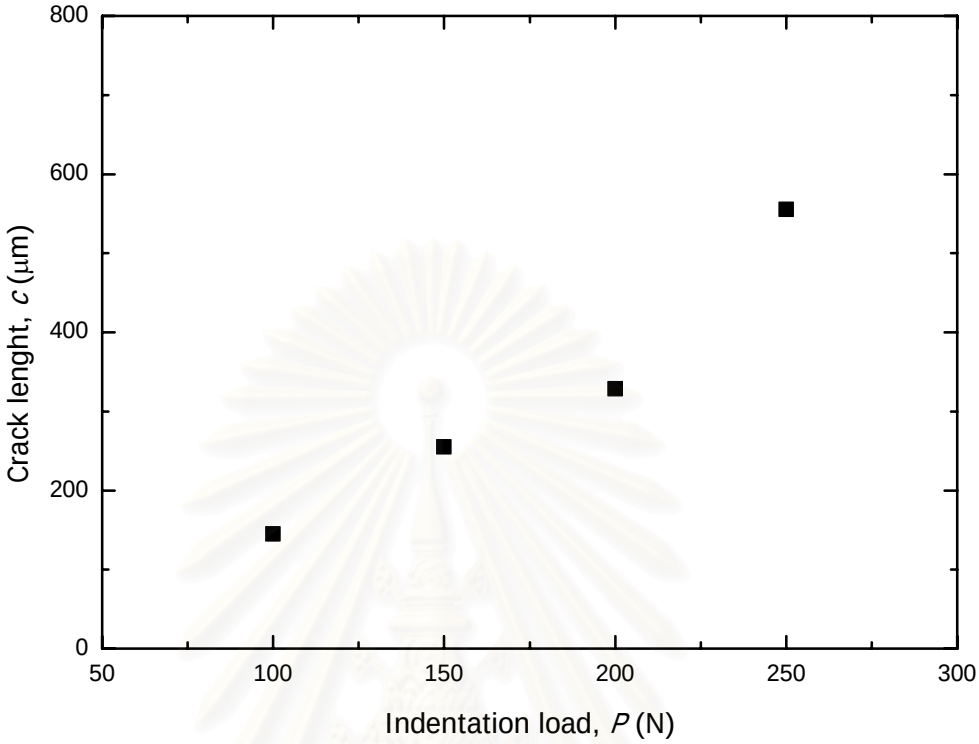

Fig. 4.8 Plot of the cone crack length in the coating layer as a function of indentation load, for glass/steel-epoxy resin/glass system, with coating thickness d = 1000 μm bonded with steel-epoxy resin of thickness h = 20 μm.

Figure 4.9 shows the effect of indentation load on Hertzian contact damage on the glass/steel-epoxy resin/glass system, with the coating thickness of 500 μm bonded with steel-epoxy resin of thickness h = 20μm, from bonded-interface specimens. The indentation loads P are 100, 150, 200 and 250 N. Again, no delamination is shown along the glass/steel-epoxy resin/glass interface. The first appeared crack is the cone crack initiates at the top surface of the coating layer at load P = 100 N, and the cone crack length increases as the load increasing (Figs. 4.9 (a), (b) and(c)). However, at the indentation load P = 250 N, its length does not increase, but there is another crack initiated at the top surface of the interlayer (see Fig. 4.9 (d)). This second type of crack extends vertically toward the coating layer. This new fracture mode that occurs at the bottom surface of coating layer is the radial crack, and the critical load P_r to initiate the radial crack for this system is 200 N < P_r < 250 N (Fig. 4.9 (d)).

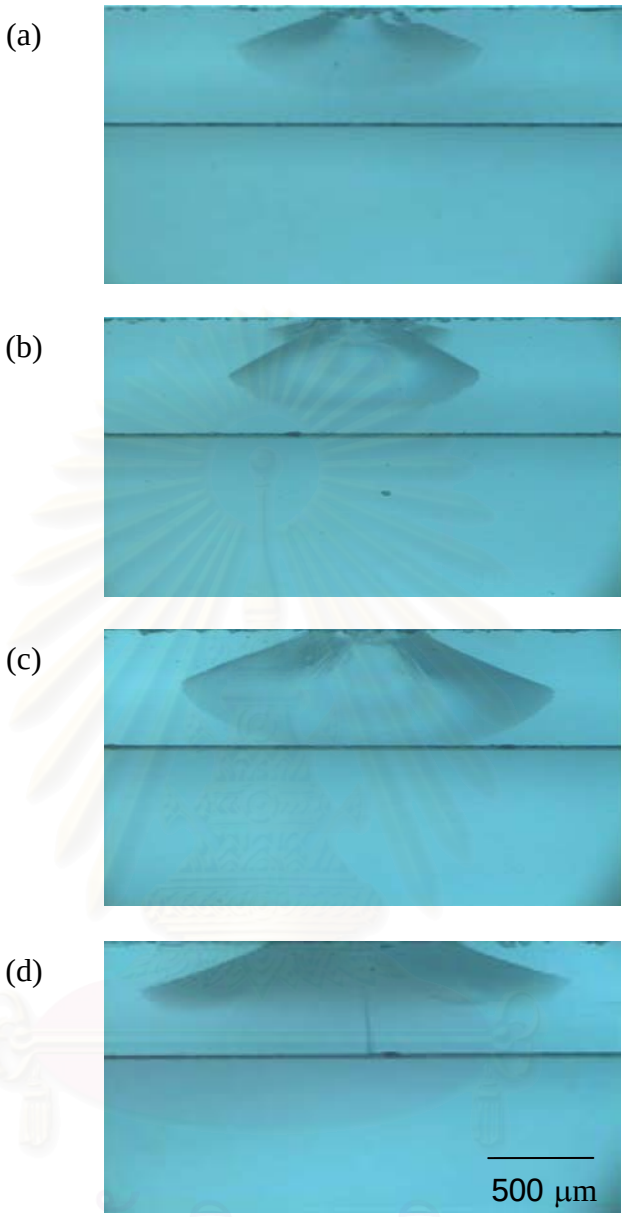

Fig. 4.9 Contact fracture in glass/steel-epoxy resin/glass system, with soda-lime glass coating thickness d = 500 μm bonded with steel-epoxy resin of thickness h = 20μm, using a WC sphere of radius r = 1.59 mm. It demonstrates the effect of indentation load: (a) P = 100 N; (b) P = 150 N; (c) P = 200 N; and (d) P = 250 N.

Figure 4.10 shows the effect of indentation load on the Hertzian contact damage on glass/steel-epoxy resin/glass system, with the coating thickness of 1000 μm bonded with steel-epoxy resin of thickness h = 200 μm, from bonded-interface specimens. The indentation loads P are 50, 100, 150, and 200N. Again, no delamination is shown along the glass/steel-epoxy resin/glass interface. At P = 50 N, the initiated cone crack at the top coating surface extends downward into the coating layer (Fig. 4.10 (a)). It grows further at P = 100 N (Fig. 4.10 (b)). At P = 150 N (Fig. 4.10(c)), the fracture in the coating changes from a single cone crack system to a multiple cone crack system. The cone crack does not appear to extend much further in depth than the first cone crack. At P = 200 N, the other crack systems and the radial cracks extend vertically upward from the top surface of the interlayer toward the coating layer (Fig. 4.10 (d)). The critical load P_r to initiate the radial crack for this system is 150 N < P_r < 200 N. Consequently the primary effect of increased loadings is to increase the density rather than the depth of cone cracks.

Figure 4.11 shows the effect of indentation load on the Hertzian contact damage on glass/steel-epoxy resin/glass system, with the coating thickness of 500 μm bonded with steel-epoxy resin of thickness h = 200 μm, from bonded-interface specimens. The indentation loads P are 50, 100, 150, and 200 N. A cone crack is found to be initiated at the top surface of the coating layer at P =50 N (see Fig. 4.11 (a)). It extends downward further into the coating layer at P = 100 N (Fig. 4.11 (b)). At P = 150 N (Fig. 4.11(c)) and P = 200 N (Fig. 4.11 (d)), multiple cone cracks occur and do not appear to extend much further in depth than the first cone crack. The critical load P_r to initiate another crack system, the radial crack, for this system is 100 N < P_r < 150 N.

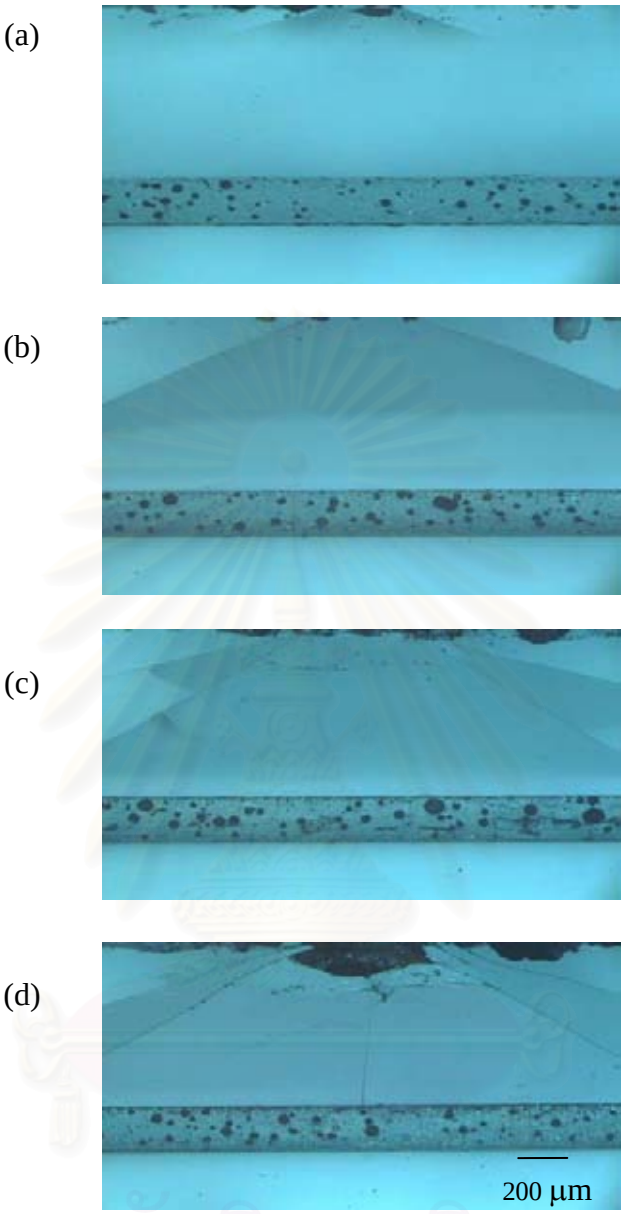

Fig. 4.10 Contact fracture in glass/steel-epoxy resin/glass system, with soda-lime glass coating thickness d = 1000 μm bonded with steel-epoxy resin of thickness h = 200μm, using a WC sphere of radius r = 1.59 mm. It demonstrates the effect of indentation load: (a) P =50 N; (b) P = 100 N; (c) P = 150N; and (d) P =200 N. Note that the crack density increases as the load is increasing.

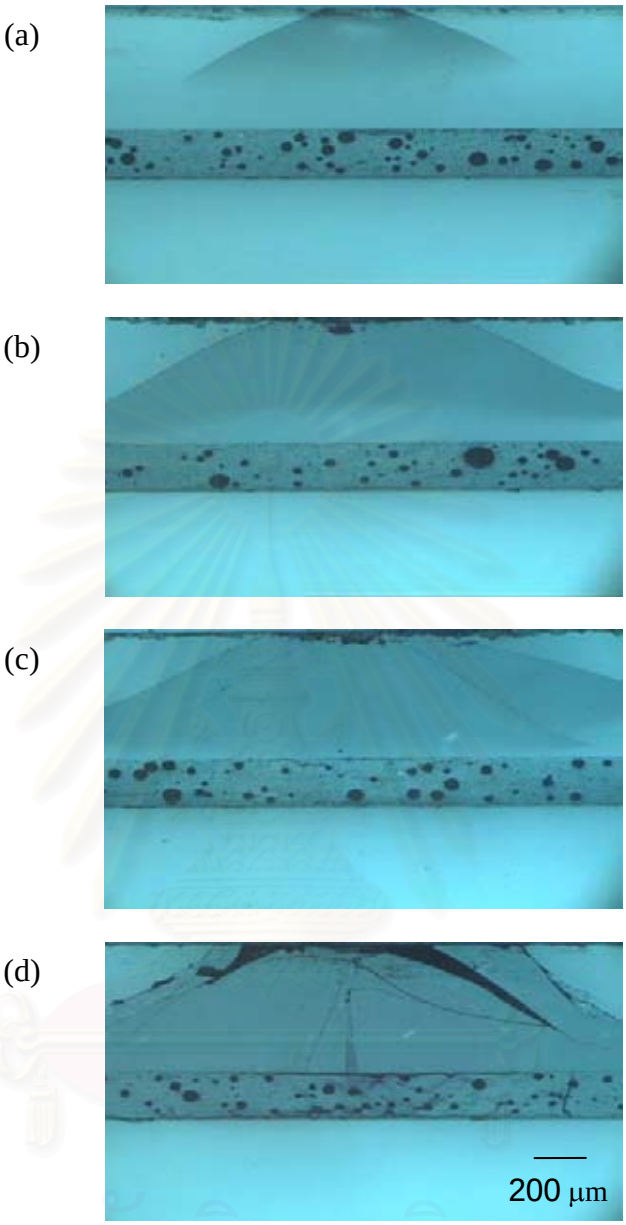

Fig. 4.11 Contact fracture in glass/steel-epoxy resin/glass system, with soda-lime glass coating thickness d = 500 μm bonded with steel-epoxy resin of thickness h = 200 μm, using a WC sphere of radius r = 1.59 mm. It demonstrates the effect of indentation load: (a) P =50 N; (b) P = 100N; (c) P = 150 N; and (d) P = 200 N. Note that the damage increases as the load is increasing.

4.2.2 Effect of Coating Layer Thickness

The sequence of micrographs of Hertzian contact damage in glass/steel-epoxy resin/glass system for two coating thicknesses, d = 1000 and 500 μm, bonded with the same steel-epoxy resin of thickness h = 20 μm, due to a WC sphere of radius r = 1.59 mm at P = 250 N, in Fig.4.12 illustrates the effect of coating thickness on the damage patterns. For the thick coating (see Fig.4.12 (a)), only the cone crack is generated in coating, whereas in the thinner coating (see Fig.4.12 (b)), not only the cone crack is initiated, but the radial crack is also initiated at the interface between the steel-epoxy resin interlayer and the coating layer. This indicates that the damage pattern in the coating layer is dependent on the coating thickness.

The plot of cone crack length, c, as a function of coating thickness; d = 500 and 1000 μm, at load P = 100, 150, 200 and 250 N, is shown in Fig.4.13. The cone crack lengths of the thin coating are longer than cone crack lengths of the thick coating at all load. At P = 250 N, cone crack lengths of the thin coating tend to have no significant change, but another crack system, the radial crack, is initiated. The critical load P_r of radial crack initiation is 200 N< P_r <250 N for this layered system.

(a)

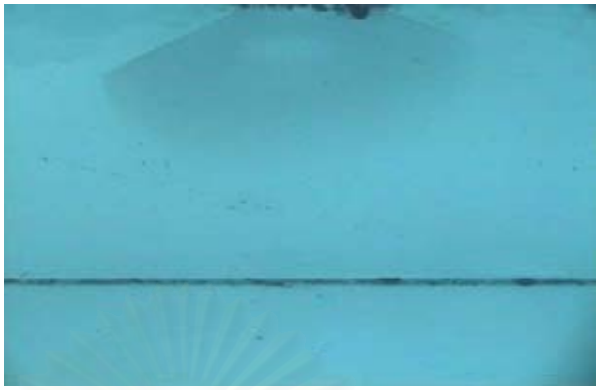

(b)

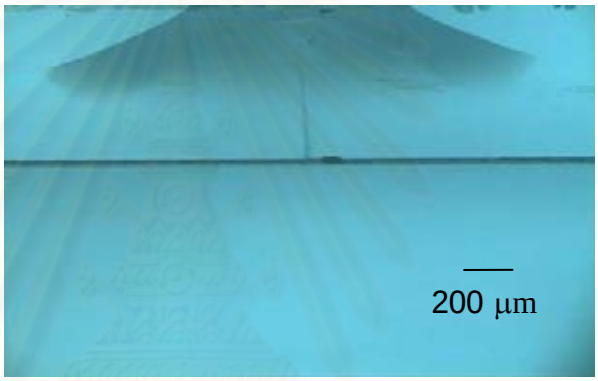

Fig. 4.12 Contact fracture in glass/steel-epoxy resin/glass system for two coating thicknesses, d = 1000 and 500 μm, bonded with the same steel-epoxy resin of thickness h = 20 μm, due to a WC sphere of radius r = 1.59 mm at load P = 250 N. It demonstrates the effect of coating thickness on the damage pattern: (a) d = 1000 μm and (b) d = 500 μm. Note that the damage increases as the coating thickness is decreasing.

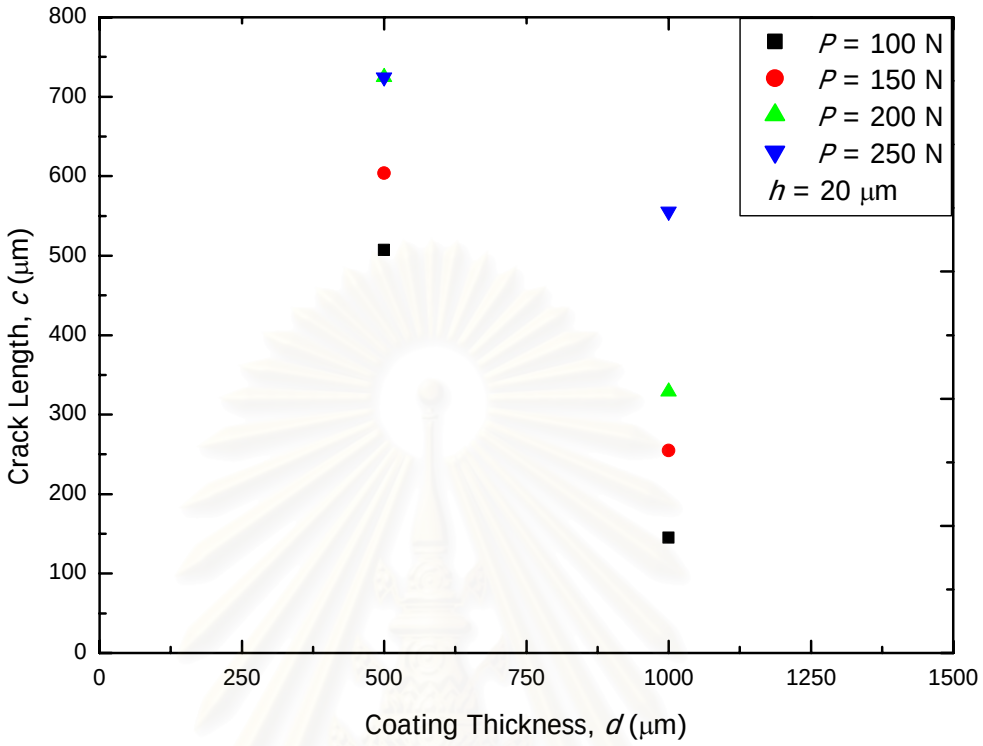

Fig. 4.13 Plot of the cone crack length in coating layer as a function of coating thickness, in different indentation loads, for glass/steel-epoxy resin/ glass system with steel-epoxy resin of thickness h = 20 μm.

The Hertzian contact damages in the glass/steel-epoxy resin/glass system for two coating thicknesses, d = 1000 and 500 μm, bonded with the same steel-epoxy resin of thickness h = 200 μm, due to a WC sphere of radius r = 1.59 mm at a fixed load P = 200 N, are shown in Fig.4.14 to illustrate the effect of coating thickness on the damage patterns. The multiple cone cracks are found to be initiated in both the thick coating and the thinner coating, but the density of cone cracks and radial cracks increases as the coating thickness decreases (see Figs. 4.14 (a) and (b)). From Section 4.2.1, P_r of the thick coating (Fig. 4.9) and thin coating (Fig. 4.10) are 150 N< P_r <200 N and 100 N< P_r <150 N, respectively. Therefore, this indicates as the coating thickness d decreases, the critical load P_r for the radial crack initiation decreases at any specified thickness h of the steel-epoxy resin.

(a)

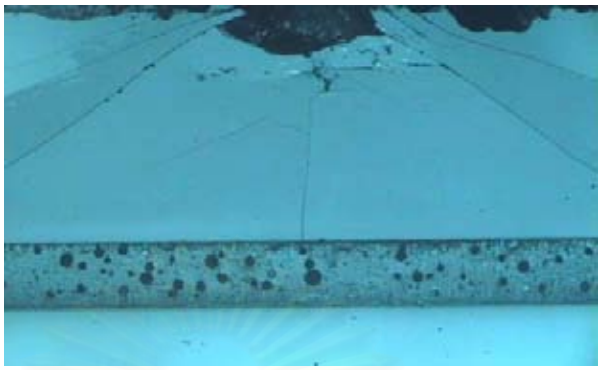

(b)

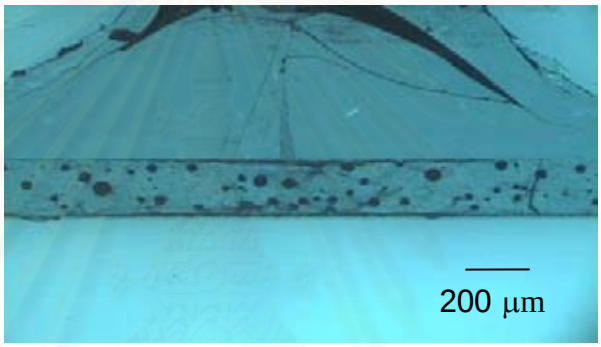

Fig. 4.14 Contact fracture in glass/steel-epoxy resin/glass system for two coating thicknesses, d = 1000 and 500 μm, bonded with steel-epoxy resin of thickness h = 200 μm, due to a WC sphere of radius r = 1.59 mm at load P = 200 N. It demonstrates the effect of coating thickness on the damage patterns: (a) d = 1000 μm and (b) d = 500 μm. Note that the damage decreases when the coating thickness increases.

4.2.3 Effect of Thickness of Steel-Epoxy Resin Interlayer

Figure 4.15 shows micrographs of Hertzian contact damage on two thicknesses of the steel-epoxy resin interlayer, h = 20 and 200 μm, due to a WC sphere of radius r = 1.59 mm at a fixed coating thickness d = 1000 μm, for a fixed load P = 200 N to illustrate the effect of thickness of the steel-epoxy resin on the damage patterns. A small single cone crack occurs at the tope surface of the coating layer of the thin interlayer specimen (see Fig. 4.15 (a)). In the thick interlayer specimen (Fig. 4.15 (b)), fractures in the coating layer are multiple cracks. Many cone cracks develop in the coating layer, and a radial crack generates at the bottom surface of the coating layer. This demonstrates that the critical load P_r to initiate the radical crack decreases as the thickness of interlayer h increases at a fixed thickness of the coating layer.

Figure 4.16 shows micrographs of Hertzian contact damage for thicknesses of the steel-epoxy resin interlayer, h = 20 and 200 μm, due to a WC sphere of radius r = 1.59 mm at another fixed thickness of the coating layer d = 500 μm, for a fixed indentation load P = 200 N. Again only a single cone crack develops in the coating layer of the thin interlayer specimen (see Fig. 4.16 (a)), whereas multiple cracks initiate in the coating layer of the thicker interlayer specimen (see Fig. 4.16 (b)). Referring to Sec.4.2.1 P_r of the system with thicker interlayer h = 20 μm is 200 N < P_r < 250 N (see Fig. 4.9 (d)), whereas P_r of the system with thicker layer interlayer, this system h = 200 μm is 100 N < P_r < 150 N (see Fig. 4.11 (c)). Consequently, these results indicate that the critical local P_r to initiate the radical crack decreases whereas the crack density increases as the thickness of the steel-epoxy resin increasess.

(a)

(b)

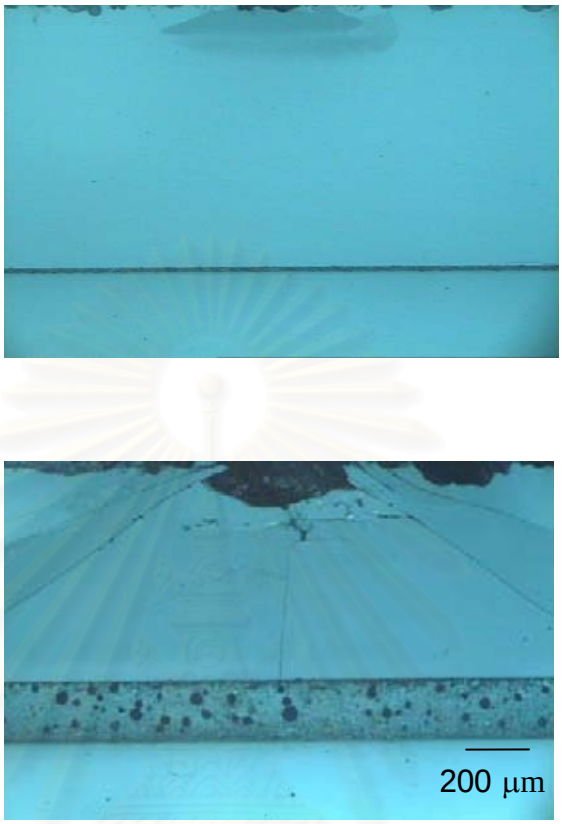

Fig. 4.15 Hertzian contact damage for two thicknesses of steel-epoxy resin interlayer, h = 20 and 200 μm, due to a WC sphere of radius r = 1.59 mm at fixed thickness of coating layer d = 1000 μm, for fixed load P = 200 N to illustrate the effect of thickness of steel-epoxy resin interlayer on the damage patterns: (a) h = 20 μm and (b) h = 200 μm. Note that the damage increases when h decreases.

(a)

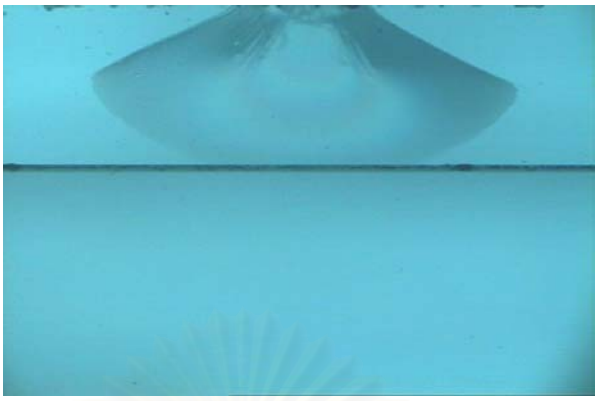

(b)

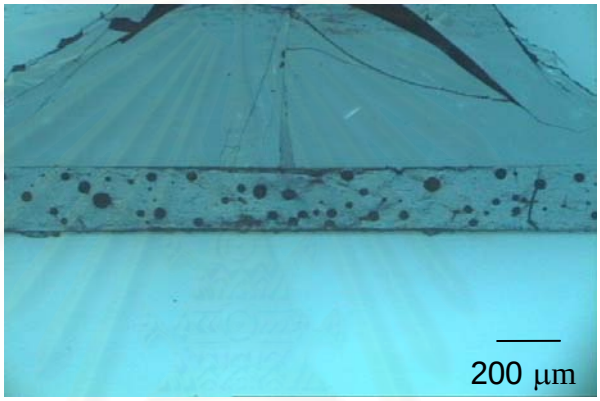

Fig. 4.16 Hertzian contact damage for two thicknesses of the steel-epoxy resin interlayer, h = 20 and 200 μm, due to a WC sphere of radius r = 1.59 mm at fixed thickness of coating layer d = 500 μm, for fixed indentation load P = 200 N to illustrate the effect of thickness of steel-epoxy resin interlayer on the damage patterns: (a) h = 20 μm and (b) h = 200μm. Note that the damage increases with increasing h.

4.3 Damage Patterns of Glass/ Epoxy Resin/Glass

4.3.1 Effect of Indentation Load

Figure 4.17 from bonded-interface specimens, it shows the effect of indentation load on Hertzian contact damage on glass/ epoxy resin/glass system, with coating thickness of 1000 μm bonded with epoxy resin of thickness h = 20 μm. The indentation loads P are 100, 150, 200 and 250 N. There is no delamination during indentation. Micrographs show cone crack fractures in the coating layer without any crack in the substrate. The initiated cone crack at the top coating surface at P = 100 N extends downwards into the coating layer (Fig. 4.17 (a)). At P = 150 N, the cone crack develops much further in crack length than the cone crack with P = 100 N (Fig. 4.17 (b)) Then the crack length increases moderately at P = 200 N (Fig. 4.17(c)) and increases slightly at P = 250 N (Fig. 4.17 (d)). The cone crack length c as a function of indentation load; P = 100, 150, 200 and 250 N, is shown in Fig. 4.18. It is assumed that the cone crack length increases when the load is increasing until it reaches a peak before changing from a single cone crack system to a multiple crack system

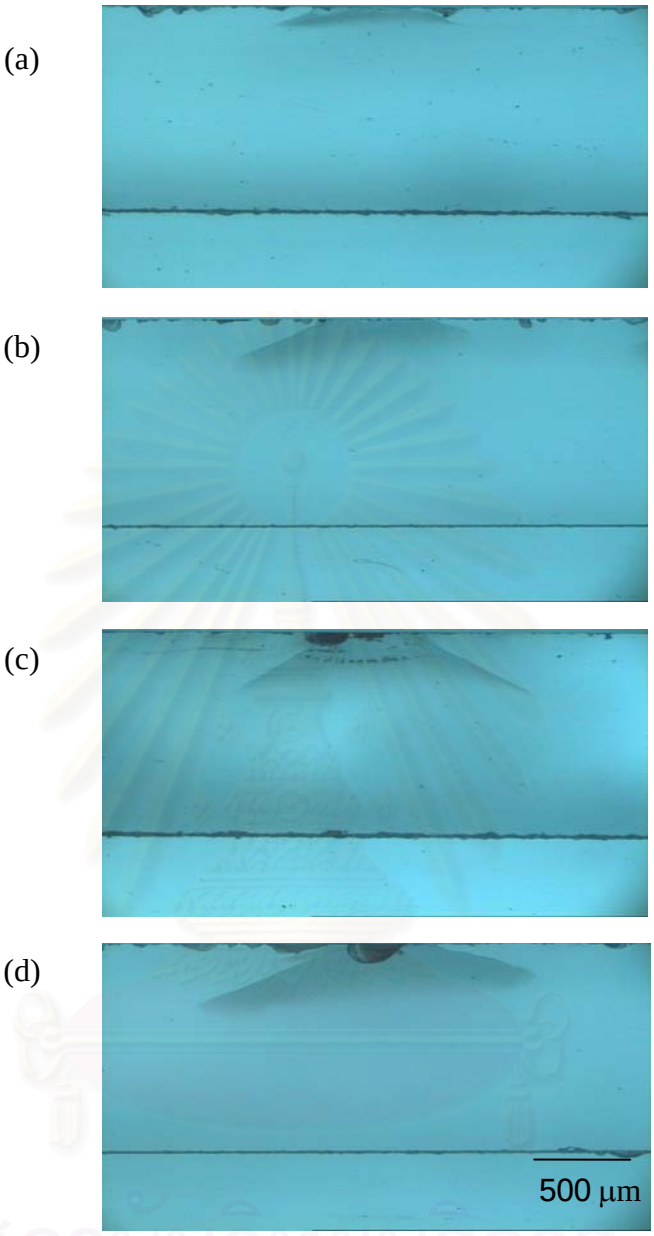

Fig. 4.17 Contact fracture in glass/ epoxy resin/glass system, with soda-lime glass coating thickness d = 1000 μm bonded with epoxy resin of thickness h = 20 μm, using a WC sphere r = 1.59 mm. It demonstrates the effect of indentation load: (a) P = 100 N; (b) P = 150 N; (c) P = 200 N; and (d) P = 250 N. Note that the cone crack length increases when the load is increasing.

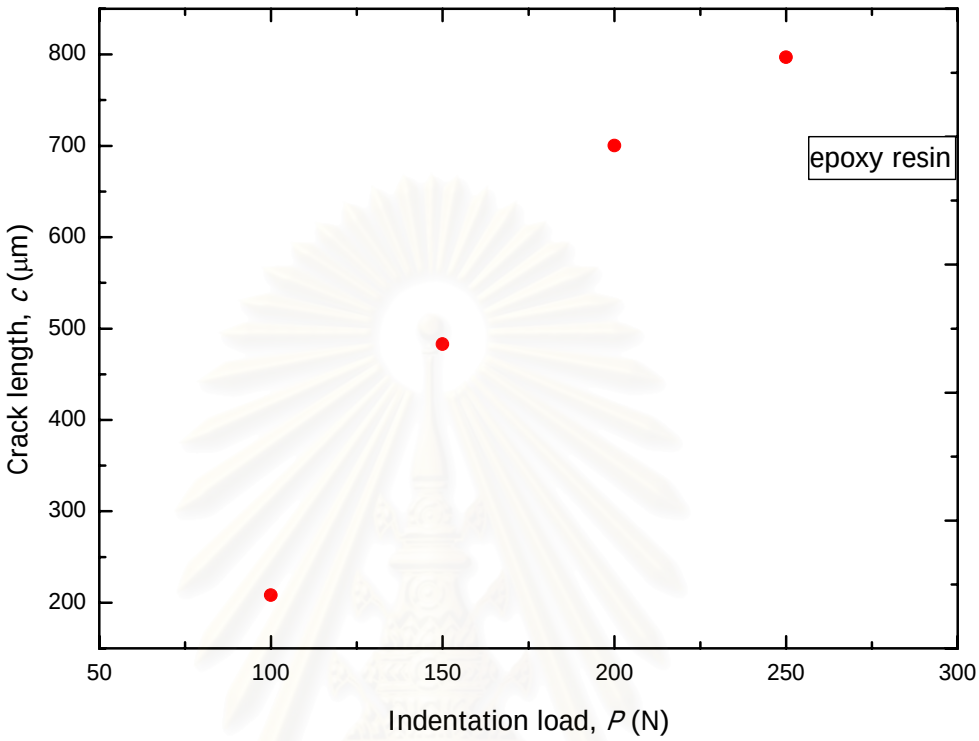

Fig.4.18 Plot of the cone crack length in the coating layer as a function of indentation load, for glass/ epoxy resin/glass system, with coating thickness d = 1000 μm bonded with epoxy resin of thickness h = 20 μm.

Figure 4.19 from bonded-interface specimens, it shows the effect of indentation load on Hertzian contact damage on glass/ epoxy resin/glass system, with coating thickness of 500 μm bonded with epoxy resin of thickness h = 20 μm. The indentation loads P are 100, 150, 200 and 250 N. Again, no delamination is shown along the glass/ epoxy resin/glass interface. The initiated cone crack on the top coating surface at P = 100 N extends downward into the coating layer (Fig. 4.19 (a)). The cone crack develops at P = 150 N (Fig. 4.19 (b)). At P = 200 N and 250 N (Fig. 4.19 (c) and (d)), the cone crack does not appear to extend much further in depth than the cone crack with P = 150 N, but the cone crack generates outside the contact circle and the radial crack initiates from the coating/ substrate interface. Hence, the primary effect of increased loading is to increase the density rather than the depth of the cone crack. The critical load to initiate the radial crack for this system is 200 N < P_r < 250 N.

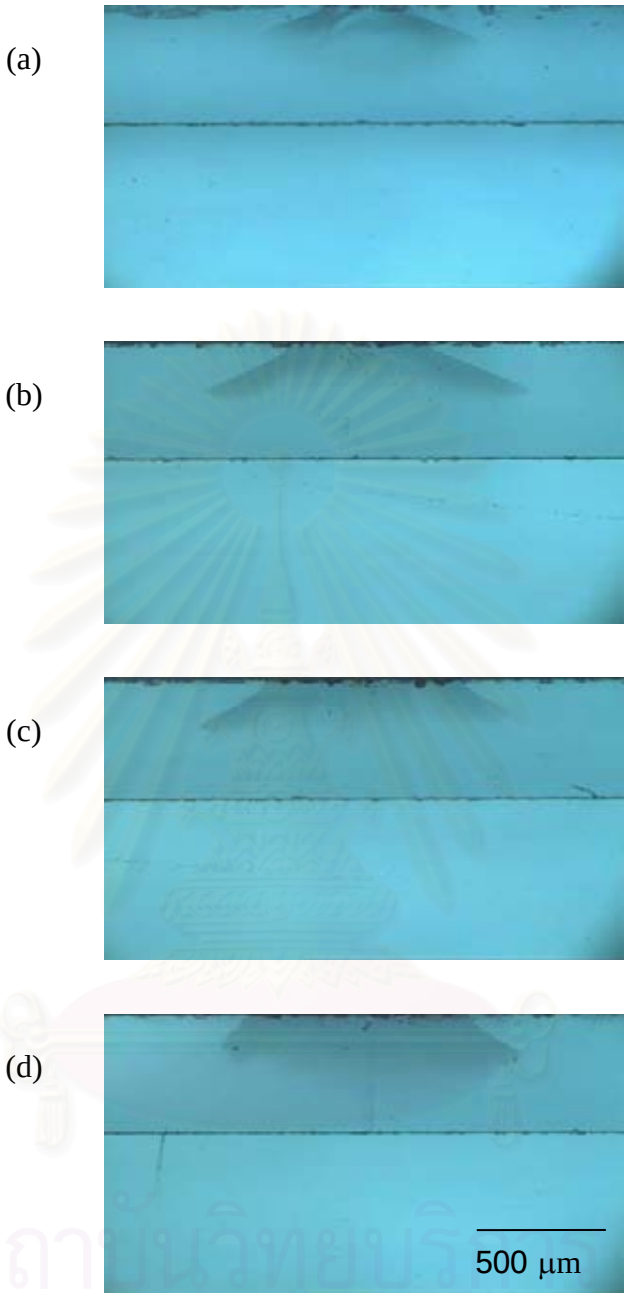

Fig. 4.19 Contact fracture in glass/ epoxy resin/glass system, with soda-lime glass coating thickness d = 500 μm bonded with epoxy resin of thickness h = 20 μm, using a WC sphere r = 1.59 mm. It demonstrates the effect of indentation load: (a) P = 100 N; (b) P = 150 N; (c) P = 200 N; and (d) P = 250 N. Note that the crack density increases when the load increases.

Figure 4.20 shows the effect of indentation load on Hertzian contact damage on glass/ epoxy resin/glass system, with coating thickness of 1000 μm bonded with epoxy resin of thickness h = 200 μm. The indentation loads P are 50, 100, 150, and 200 N. There is no delamination during indentation. At P = 50 N, the cone crack initiated at the top coating surface extends downward into the coating layer (Fig. 4.20 (a)). The cone crack grows further at P = 100 N (Fig. 4.20 (b)). At P = 150 N (Fig. 4.20(c)), the fracture in the coating changes from a single cone crack system to a multiple crack system and does not appear to extend much further in depth than the first cone crack, and micrographs show the radial cracks extend vertically towards the top surface at P = 200 N (Fig.4.20 (d)). The critical load to initiate the first radial crack for this system is 150 N < P_r < 200 N. Therefore the cause of the effect of increased loading is to increase the density rather than the dept of cone cracks. That is the damages increase when the load increases.

Figure 4.21 shows the effect of indentation load on Hertzian contact damage on glass/ epoxy resin/glass system, with coating thickness of 500 μm bonded with epoxy resin of thickness h = 200 μm. The indentation loads P are 50, 100, 150, and 200 N. There is no delamination during indentation. The micrographs show the initiated cone crack at the top coating surface at P =50 N extends downwards into the coating layer (Fig. 4.21 (a)). The indentation load at P = 100 N and 150 N (Fig. 4.21 (b) and (c)) does not increase the cone crack in size, but increases the crack in density. The fracture in the coating changes from a single cone crack system to a multiple crack system, and the micrographs show the radial cracks extend vertically upward toward the top surface. Therefore, damages increase when the load increases, and the critical load to initiate the radial crack for this system is 50 N < P_r < 100 N.

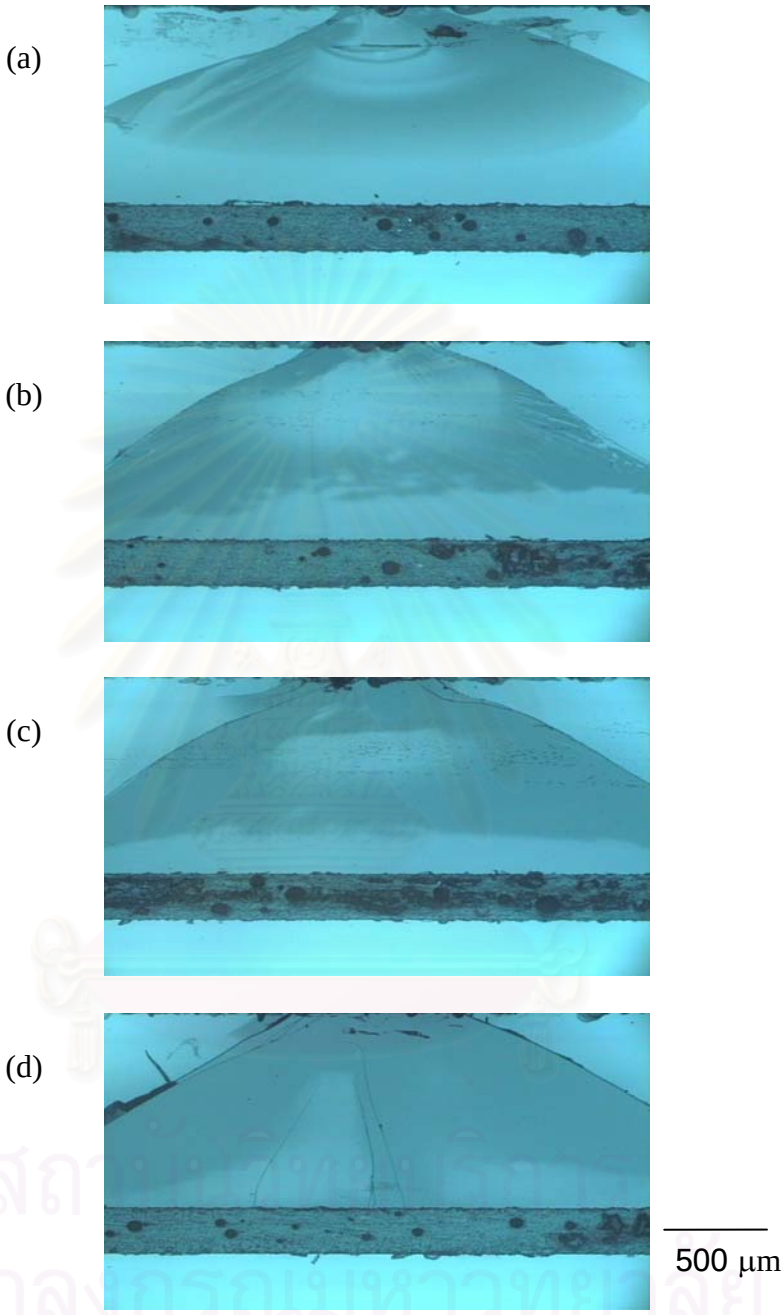

Fig.4.20 Contact fracture in glass/ epoxy resin/glass system, with soda-lime glass coating thickness d = 1000 μm bonded with epoxy resin of thickness h = 200μm, using a WC sphere r = 1.59 mm. It demonstrates the effect of indentation load: (a) P = 50 N; (b) P = 100 N; (c) P = 150 N; and (d) P =200 N. Note the damage increases when the load increases.

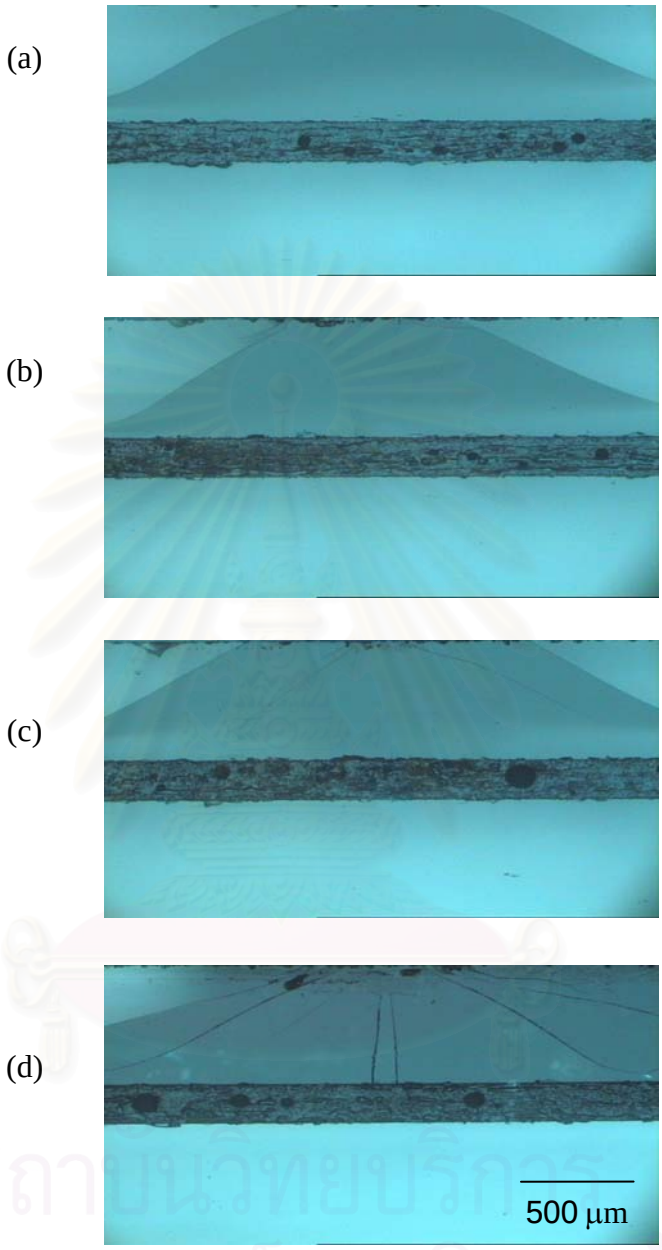

Fig. 4.21 Contact fracture in glass/ epoxy resin/glass system, with soda-lime glass coating thickness d = 500 μm bonded with steel-epoxy resin of thickness h = 200 μm, using a WC sphere r = 1.59 mm. It demonstrates the effect of indentation load: (a) P =50 N; (b) P = 100N; (c) P = 150 N; and (d) P = 200 N. Note that the damages increase when the load is increasing.

4.3.2 Effect of Coating Layer Thickness

The sequence of micrographs of Hertzian contact damage on glass/ epoxy resin/glass system for two coating thicknesses, d = 1000 and 500 μm, bonded with epoxy resin of thickness h = 20 μm, with a WC sphere r = 1.59 mm at fixed indentation load P = 250 N. In Fig. 4.22, it illustrates the effect of coating thickness on the damage patterns. A single cone crack occurs in the thick coating layer (Fig. 4.22 (a)). In the thinner coating (Fig. 4.22 (b)) not only the cone crack is initiated, but the radial crack is also initiated at the interface between the silicone sealant interlayer and the coating layer. This indicates that the damage pattern in the coating layer is dependent on the coating thickness, and decreasing d will cause decreasing P_r.

The micrographs of Hertzian contact damage on glass/ epoxy resin/glass system for two coating thicknesses, d = 1000 and 500 μm, bonded with epoxy resin of thickness h = 200 μm, with a WC sphere r = 1.59 mm at fixed load P = 200 N. In Fig. 4.23 it illustrates the effect of coating thickness on the damage patterns. The multiple cracks initiate in both thick coating and thin coating, but the density of the cone cracks and the radial cracks increases as the coating thickness decreases (Fig. 4.23 (a) and (b)). From Section 4.23, P_r of thick coating (Fig. 4.20) and thin coating (Fig. 4.35) are 150 N < P_r < 200 N and 50 N < P_r < 100 N, orderly. Therefore, it indicates that decreasing d will cause decreasing P_r at any specified h.

(a)

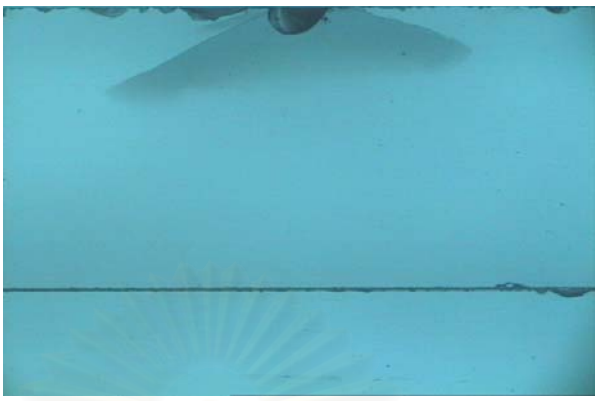

(b)

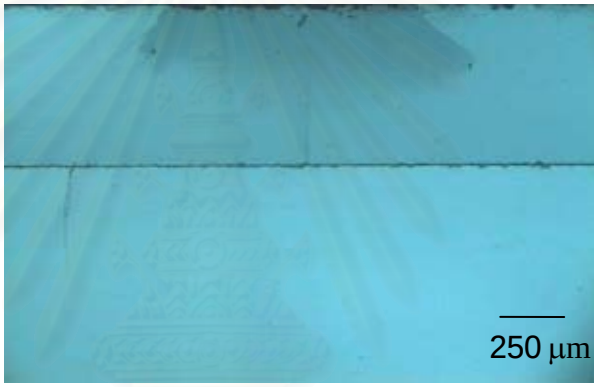

Fig. 4.22 Contact fracture in bulk glass and glass/ epoxy resin/glass system for two coating thicknesses, d = 1000 and 500 μm, bonded with epoxy resin of thickness h = 20 μm, with a WC sphere r = 1.59 mm at load P = 250 N. It demonstrates the effect of coating thickness on the damage pattern: (a) d = 1000 μm and (b) d = 500 μm. Note that the damage decreases when the coating thickness increases.

(a)

(b)

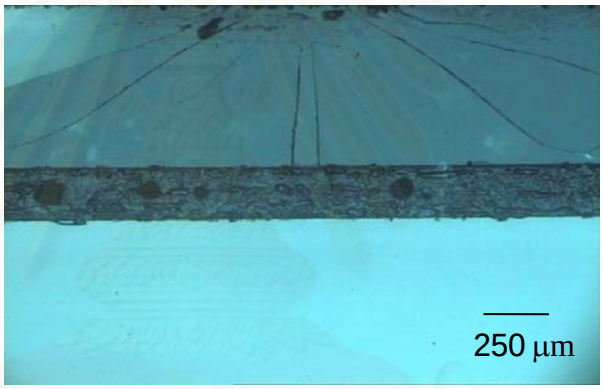

Fig. 4.23 Contact fracture in bulk glass and glass/ epoxy resin/glass system for two coating thicknesses, d = 1000 and 500 μm, bonded with epoxy resin of thickness h = 200 μm, with a WC sphere r = 1.59 mm at load P = 200 N. It demonstrats the effect of coating thickness on the damage pattern: (a) d = 1000 μm and (b) d = 500 μm. Note that the damage decreases when the coating thickness increases.

4.3.3 Effect of Thickness of Epoxy-Resin Interlayer

Figure 4.24 shows the micrographs of Hertzian contact damage for two adhesive polymer thicknesses, h = 20 and 200 μm, with a WC sphere r = 1.59 mm at fixed coating thickness d = 1000 μm, for load P = 200 N. It illustrates the effect of interface adhesive polymer thickness on the damage patterns. A single cone crack occurs in the coating layer of the thin adhesive specimen (Fig. 4.24 (a)). In the thick adhesive (Fig. 4.24 (b)) the fractures in the coating are multiple cracks. Many cone cracks develop in the coating, and the radial crack generates at the bottom surface of the coating. It demonstrates that P_r declines when h increases at fixed coating, so the damage increases when h increases.

Figure 4.25 shows the micrographs of Hertzian contact damage for two adhesive polymer thicknesses, h = 20 and 200 μm, due to a WC sphere r = 1.59 mm at fixed coating thickness d = 500 μm, for load P = 200 N. It illustrates the effect of interface adhesive polymer thickness on the damage patterns. A single cone crack develops in the coating layer of the thin adhesive specimen (Fig. 4.25 (a)), whereas the multiple cracks initiate in the coating layer of thicker adhesive specimen (Fig.4.25 (a)) at load P = 200 N. From Section 4.3.1, P_r of system h = 20 μm at d = 500 μm is 200 N < P_r < 250 N (Fig. 4.19(d)), and P_r of system h = 200 μm at d = 500 μm is 50 N < P_r < 100 N (Fig. 4.21(c)). Consequently it indicates that P_r declines when h increases. As a result the damage increases when h increases at any given d.

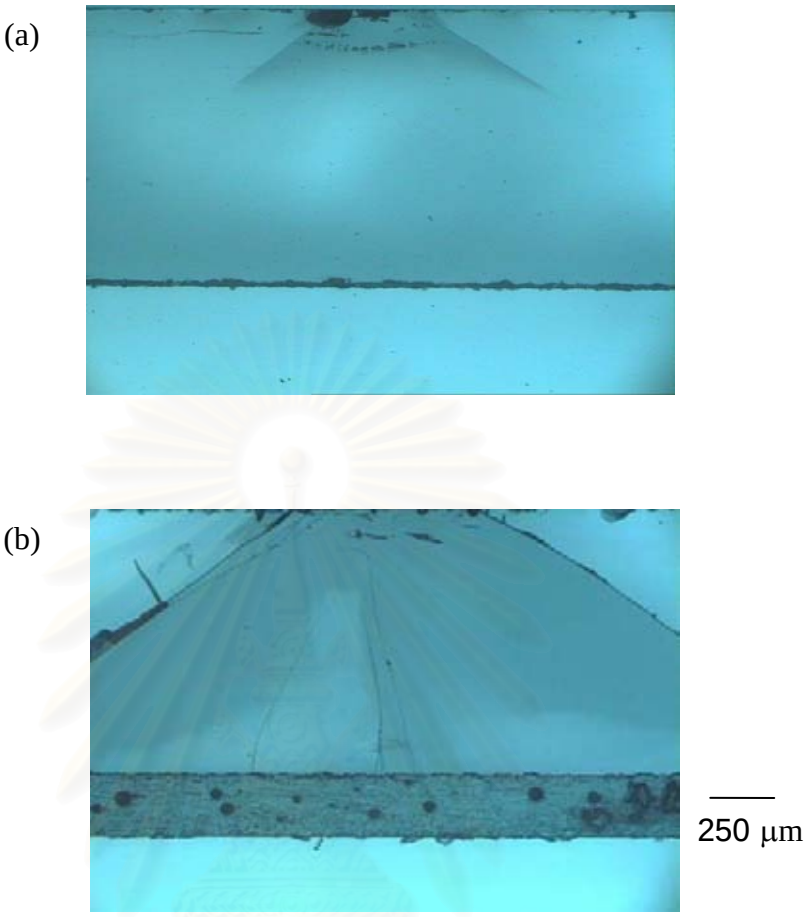

Fig. 4.24 Hertzian contact damage for two adhesive polymer thicknesses, h = 20 and 200 μm, with a WC sphere r = 1.59 mm at fixed coating thickness d = 1000 μm, for load P = 200 N. It illustrates the effect of interface adhesive polymer thickness on the damage patterns. (a) h = 20 μm and (b) h = 200 μm. Note that the damage increases when h increases.

(a)

(b)

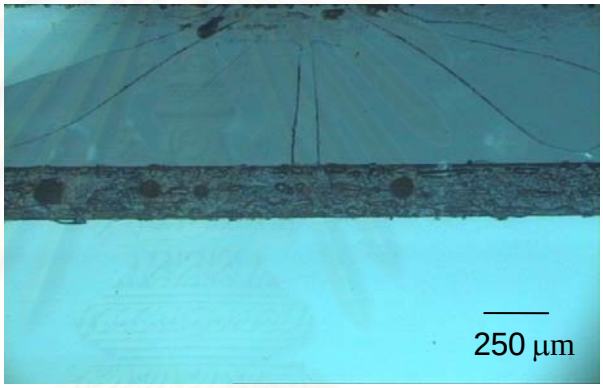

Fig. 4.25 Hertzian contact damage for two adhesive polymer thicknesses, h = 20 and 200 μm, with a WC sphere r = 1.59 mm at fixed coating thickness d = 500 μm, for load P = 200 N. It illustrates the effect of interface adhesive polymer thickness on the damage patterns. (a) h = 20 μm and (b) h = 200μm. Note that the damage increases with h increases.

4.4 Damage Patterns of Glass/Silicone Sealant /Glass

4.4.1 Effect of Indentation Load

Figure 4.26 shows the effect of indentation load on Hertzian contact damage on glass/ silicone sealant/glass system, with coating thickness of 1000 μm bonded with silicone sealant of thickness h = 20 μm, from bonded-interface specimens. The indentation loads P are 100, 150, 200 and 250 N. There is no delamination during indentation. The micrographs show the cone crack fractures in the coating layer without any crack in the substrate. The cone crack initiated at the top coating surface at P = 100 N extends downward into the coating layer (Fig. 4.26 (a)). The cone crack grows further at P = 150 N (Fig. 4.26 (b)) Then the fracture in the coating changes from a single cone crack system to a multiple cone crack system at P = 200 N (Fig. 4.26(c)). The first cone crack length increases slightly, and the glass coating is chipped from specimen at load P = 250 N (Fig. 4.26 (d)). It indicates that the damages increase with increasing load. The cone crack length c as a function of indentation load; P = 100, 150, 200 and 250 N, is shown in Fig. 4.27.

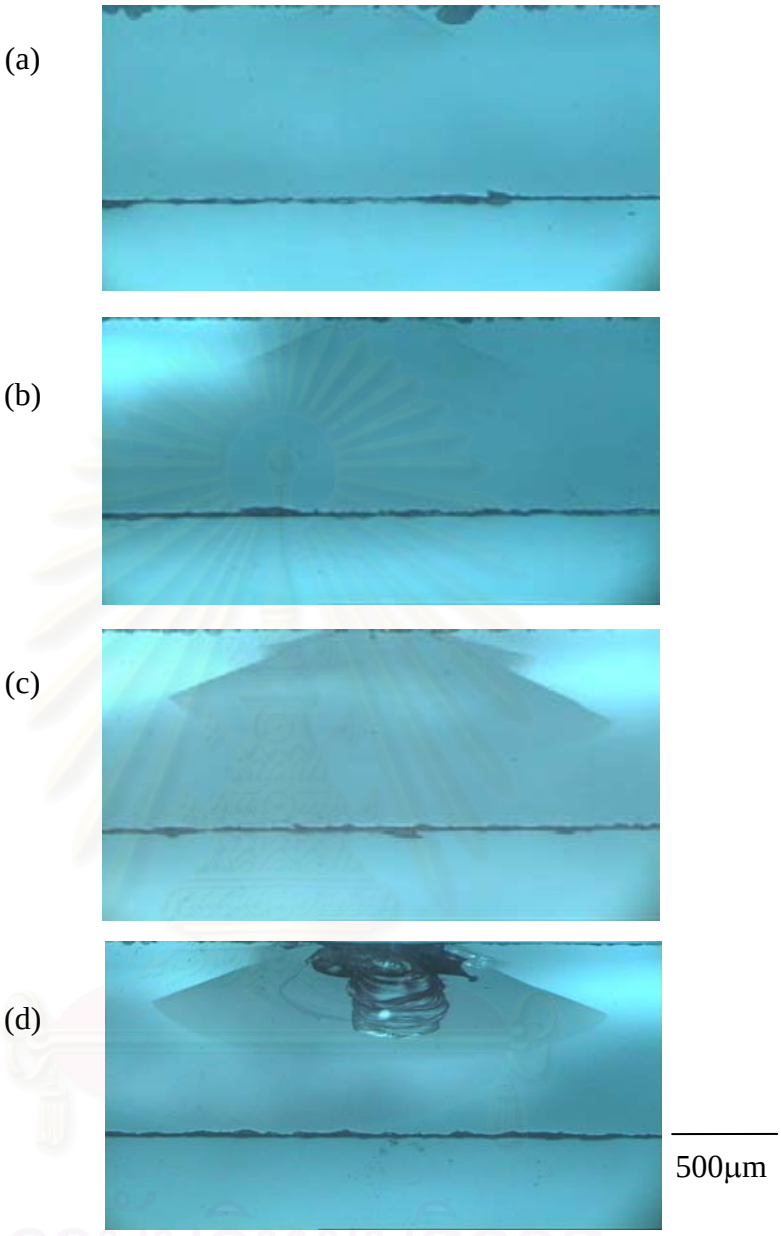

Fig. 4.26 Contact fracture in glass/ silicone sealant/glass system, with soda-lime glass coating thickness d = 1000 μm bonded with silicone sealant of thickness h = 20 μm, using a WC sphere r = 1.59 mm. It demonstrates the effect of indentation load: (a) P = 100 N; (b) P = 150 N; (c) P = 200 N; and (d) P = 250 N. Note that the damage increases with the increasing load.

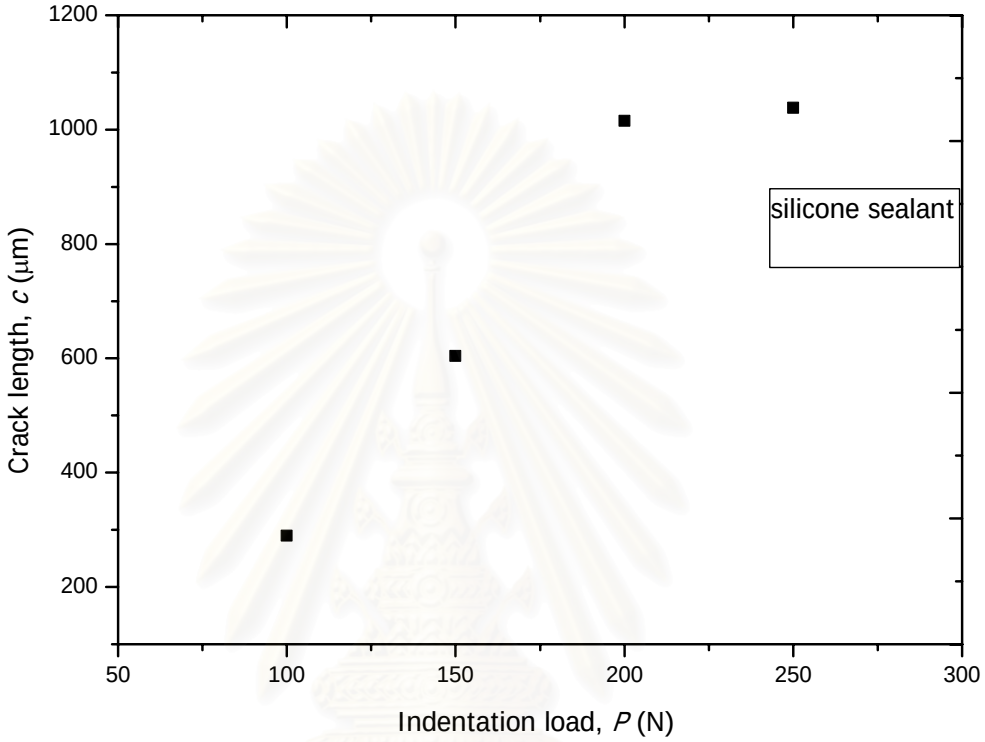

Fig. 4.27 Plot of the cone crack length in the coating layer as a function of indentation load for glass/silicone sealant/glass system, with coating thickness d = 1000 μm bonded with silicone sealant of thickness h = 20 μm.

Figure 4.28 shows the effect of indentation load on Hertzian contact damage on glass/ silicone sealant/glass system, with coating thickness of 500 μm bonded with silicone sealant of thickness h = 20 μm, from bonded-interface specimens. The indentation loads P are 100, 150, 200 and 250 N. Again, no delamination is evident along the glass/ silicone sealant/glass interface. At P = 100 N, the cone crack initiated at the top coating surface extends downward into the coating layer (Fig. 4.28 (a)). The micrographs show radial crack occurs in the bottom surface of the coating at P = 150 N (Fig. 4.28 (b)) and the the radial crack length increases with the increasing load (Fig. 4.28(c) and (d)). Therefore the damages increase with increasing load, and the critical load to initiate the radial crack for this system is 100 N < P_r < 150 N.

Figure 4.29 shows the effect of indentation load on Hertzian contact damage on glass/ silicone sealant/glass system, with coating thickness of 1000 μm bonded with silicone sealant of thickness h = 200 μm, from bonded-interface specimens. The indentation loads P are 50, 100 and 150 N. At P = 50 N, the large cone crack initiated at the top coating surface extends downward and outward into the coating layer to the interface layer, but it does not penetrate the interlayer (Fig. 4.29 (a)). The coating contains a variety of cracks at P = 100 N (Fig. 4.29(b)), the fracture in the coating changes from a single cone crack system to a multiple crack system, and the radial crack extends vertically upward toward the top surface with large size. A feature of these cracks is that they appear to arrest as they approach the bounding surfaces of the coating. At the highest load (P = 200 N) the damage intensified, leading to glass removal and coating failure (Fig. 4.29(c)). The critical load to initiate the first radial crack for this system is 50 N < P_r < 100 N.

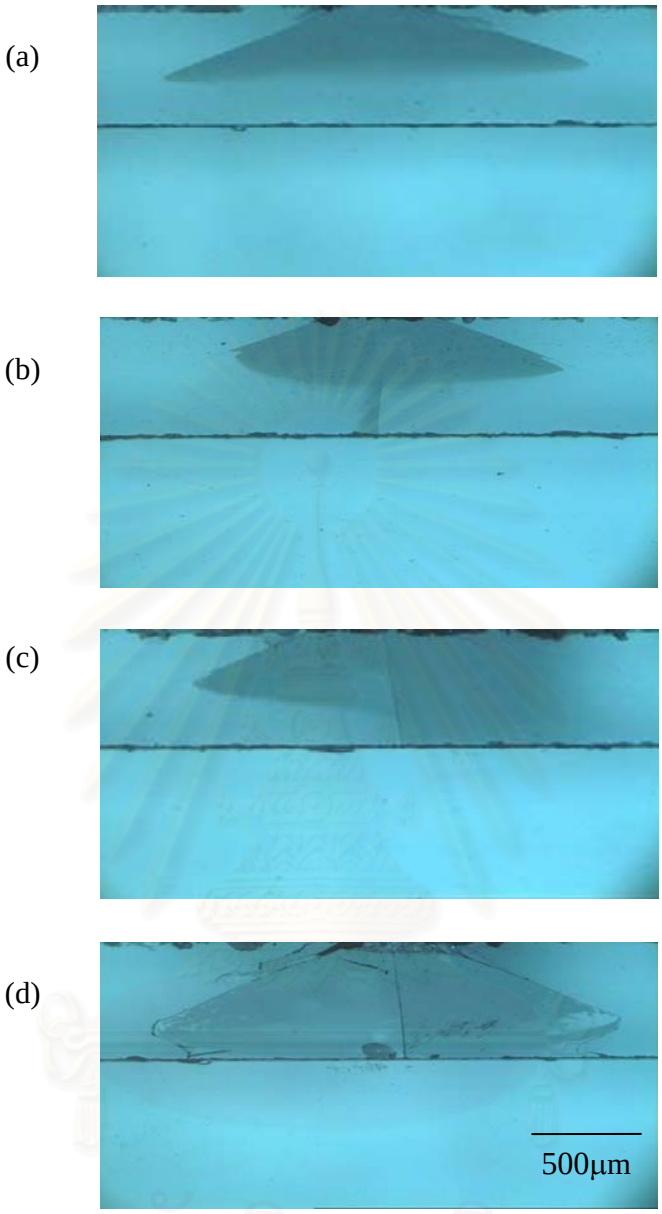

Fig. 4.28 Contact fracture in glass/ silicone sealant/glass system, with soda-lime glass coating thickness d = 500 μm bonded with silicone sealant of thickness h = 20 μm, using a WC sphere r = 1.59 mm. It demonstrates the effect of indentation load: (a) P = 100 N; (b) P = 150 N; (c) P = 200 N; and (d) P = 250 N. Note that the damage increases with increasing load.

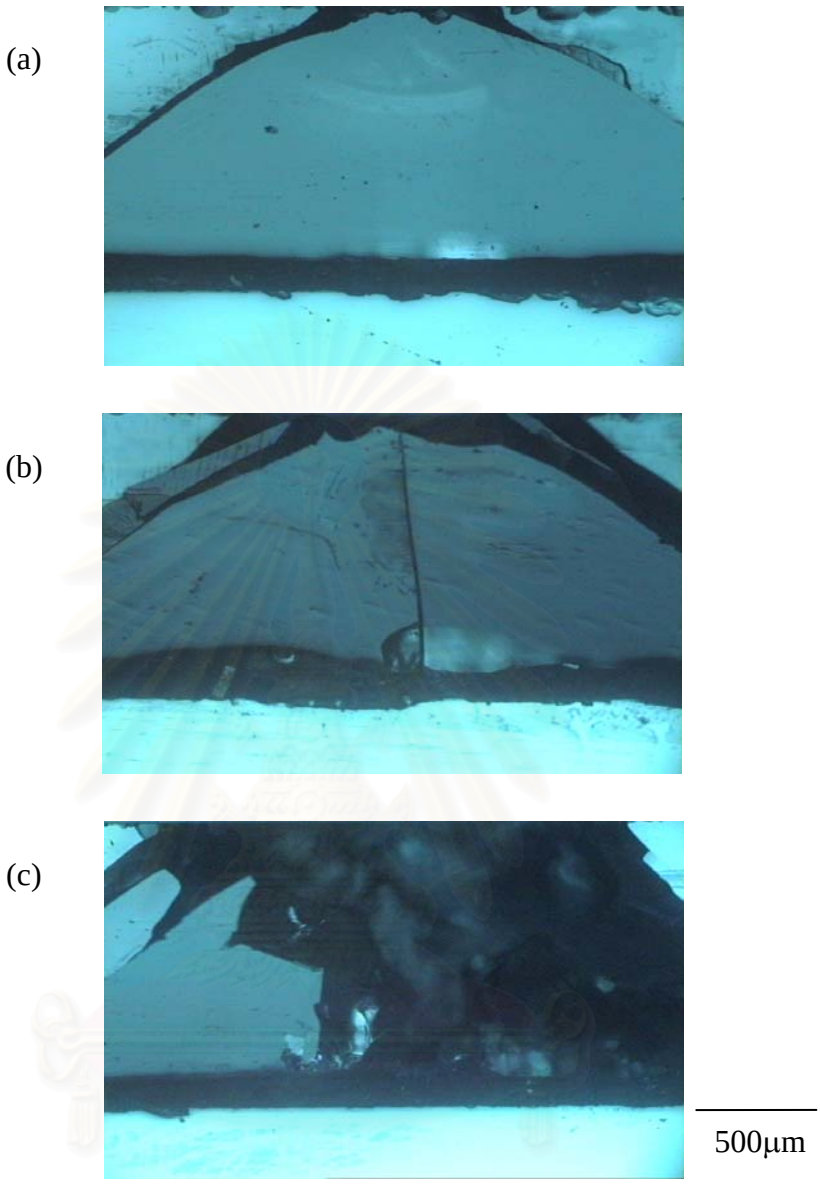

Fig. 4.29 Contact fracture in glass/silicone sealant/glass system, with soda-lime glass coating thickness d = 1000 μm bonded with silicone sealant of thickness h = 200 μm, using a WC sphere r = 1.59 mm. It demonstrates the effect of indentation load: (a) P = 50 N; (b) P = 100 N; and (d) P =150 N. Note that the crack density increases with the increasing load.

Figure 4.30 shows the effect of indentation load on Hertzian contact damage on glass silicone sealant/glass system, with coating thickness of 1000 μm bonded with silicone sealant of thickness h = 200 μm, from bonded-interface specimens. The indentation loads P are 50, 100 and 150 N with no delamination. At P = 50 N (Fig. 4.30 (a)), the coating contains a variety of cracks. The cone cracks initiated at the top surface outside the contact circle, and they extend downward and outward into the coating. The radial crack initiated from the coating/substrate interface, extends upward and inward until glass removal and coating failure, as increasing load (Fig. 4.30 (b) and (c)). The critical load to initiate the first radial crack for this system is under 50 N.

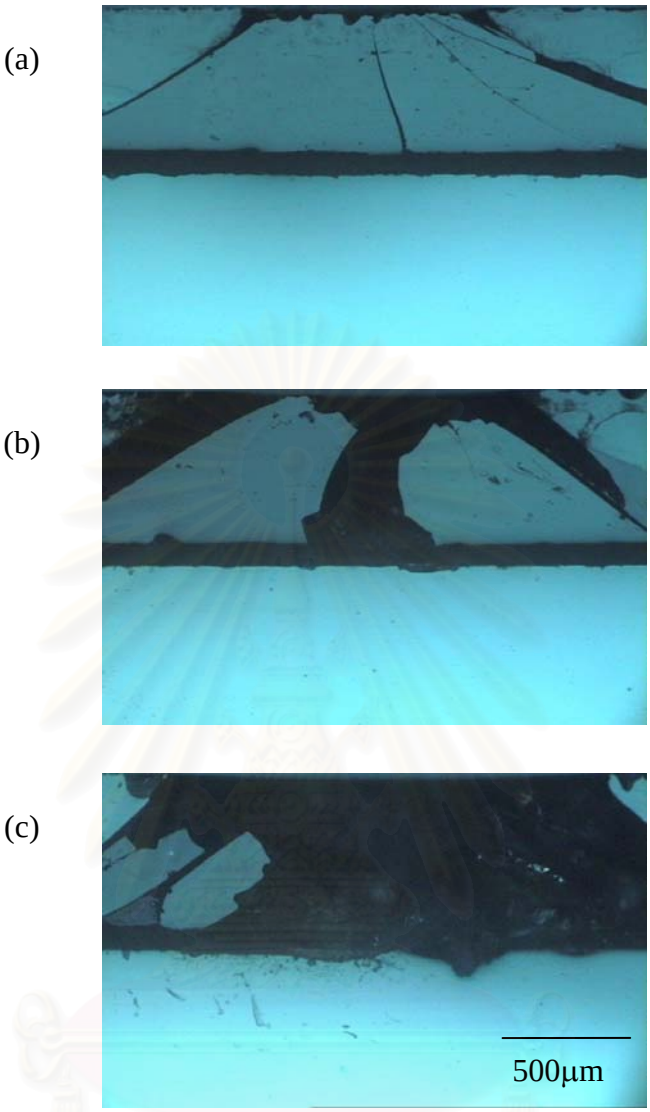

Fig. 4.30 Contact fracture in glass/silicone sealant/glass system, with soda-lime glass coating thickness d = 500 μm bonded with steel-silicone sealant of thickness h = 200 μm, using a WC sphere r = 1.59 mm It demonstrates the effect of indentation load: (a) P =50 N; (b) P = 100N; and (d) P = 200 N. Note the damages increase with increasing load.

4.4.2 Effect of Coating Layer Thickness

The sequence of micrographs of Hertzian contact damage on glass/silicone sealant/glass system for two coating thicknesses, d = 1000 and 500 μm, bonded with silicone sealant of thickness h = 20 μm, due to a WC sphere r = 1.59 mm at fixed indentation load P = 150 N. In Fig. 4.31, illustrates the effect of coating thickness on the damage patterns. A single cone crack occurs in the thick coating layer (Fig. 4.31 (a)). In the thinner coating (Fig. 4.31 (b)) there is not only cone crack initiates but radial crack appears. It indicates that the damage patterns in coating layer are dependent on coating thickness, and decreasing d decreases P_r.

The micrographs of Hertzian contact damage in glass/silicone sealant/glass system for two coating thicknesses, d = 1000 and 500 μm, bonded with silicone sealant of thickness h = 200 μm, due to a WC sphere r = 1.59 mm at fixed load P = 50 N, in Fig. 4.32 illustrates the effect of coating thickness on the damage patterns. A single cone crack occurs in the thick coating layer (Fig. 4.32 (a)), whereas the multiple cracks initiate in thinner coating (Fig. 4.32 (b)). Therefore the density of the cone cracks and the radial cracks increases as the coating thickness decreases, and decreasing d decreases P_r.

(a)

(b)

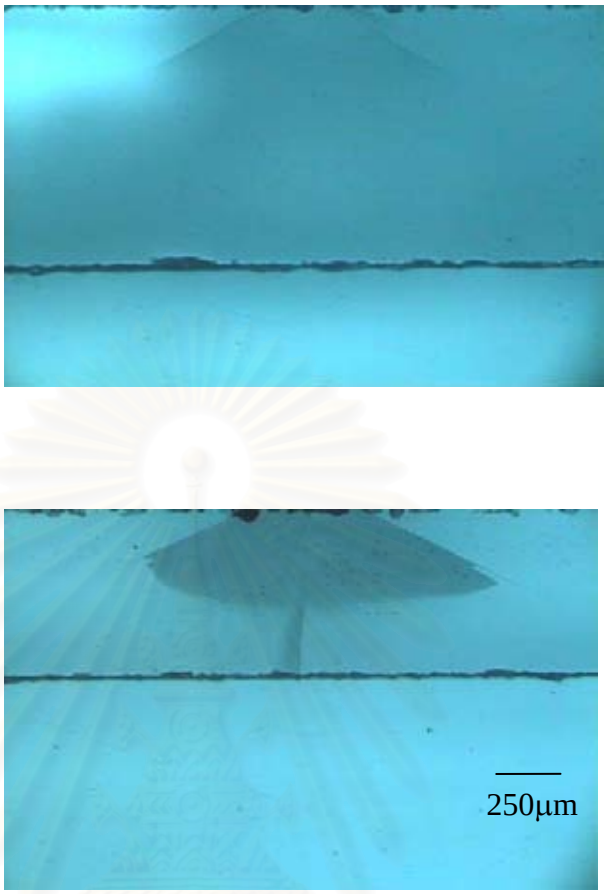

Fig. 4.31 Contact fracture in bulk glass and glass/silicone sealant/glass system for two coating thicknesses, d = 1000 and 500 μm, bonded with silicone sealant of thickness h = 20 μm, due to a WC sphere r = 1.59 mm at load P = 150 N. It demonstrates the effect of coating thickness on the damage pattern: (a) d = 1000 μm and (b) d = 500 μm. Note that the decreased damage at increasing coating thickness.

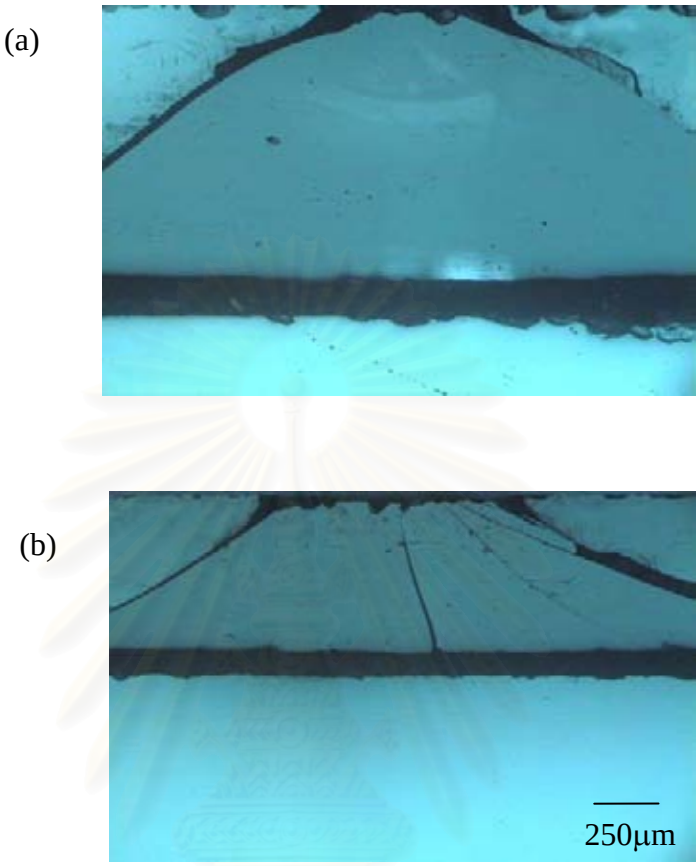

Fig. 4.32 Contact fracture in bulk glass and glass/silicone sealant/glass system for two coating thicknesses, d = 1000 and 500 μm, bonded with silicone sealant of thickness h = 200 μm, due to a WC sphere r = 1.59 mm at load P = 50 N. It demonstrates the effect of coating thickness on the damage pattern: (a) d = 1000 μm and (b) d = 500 μm. Note that the decreased damage at increasing coating thickness.

4.4.3 Effect of Thickness of Silicone-Sealant Interlayer

Figure 4.33 shows micrographs of Hertzian contact damage for two adhesive polymer thicknesses, h = 20 and 200 μm, due to a WC sphere r = 1.59 mm at a fixed coating thickness d = 1000 μm, for a fixed load P = 100 N. It illustrates the effect of thickness of silicone sealant interlayer on the damage patterns. A single cone crack occurs in the coating layer of the thin adhesive specimen (Fig. 4.33 (a)). In the thick adhesive (Fig. 4.33(b)), the fractures in the coating are multiple cracks. Many cone cracks develop in the coating, and the radial crack generates at the bottom surface of the coating and extends vertically upward toward the top surface with large size. It demonstrates that P_r declines with increasing h at fixed coating, and the damage increases with increasing h.

Figure 4.34 shows micrographs of Hertzian contact damage for two adhesive polymer thicknesses, h = 20 and 200 μm, due to a WC sphere r = 1.59 mm at fixed coating thickness d = 500 μm, for a fixed load P = 100 N, illustrates the effect of interface adhesive polymer thickness on the damage patterns. A single cone crack develops in the coating layer of thin adhesive specimen (Fig. 4.34 (a)), whereas the multiple cracks initiate in the coating layer of the thicker adhesive specimen, and there are glass chipping in the coating layer. (Fig. 4.34 (a)) So the damage increases with increasing h at any given d.

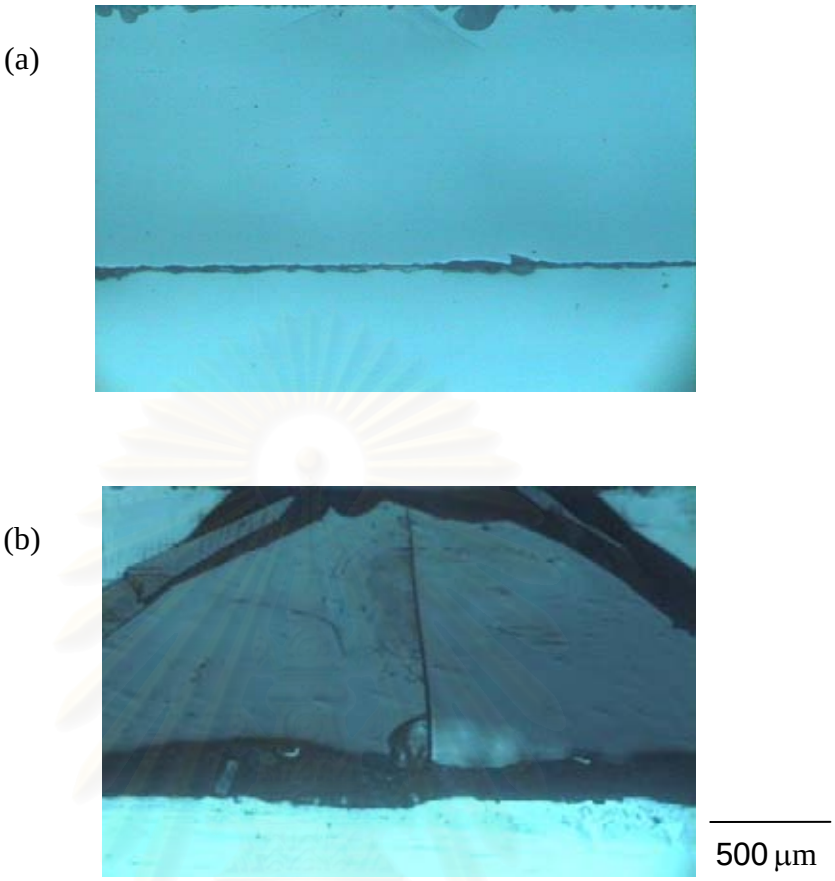

Fig. 4.33 Hertzian contact damage for two adhesive polymer thicknesses, h = 20 and 200 μm, due to a WC sphere r = 1.59 mm at fixed coating thickness d = 1000 μm, for load P = 100 N, illustrates the effect of interface adhesive polymer thickness on the damage patterns. (a) h = 20 μm and (b) h = 200 μm. Note the damage increases with increasing h.

.

(a)

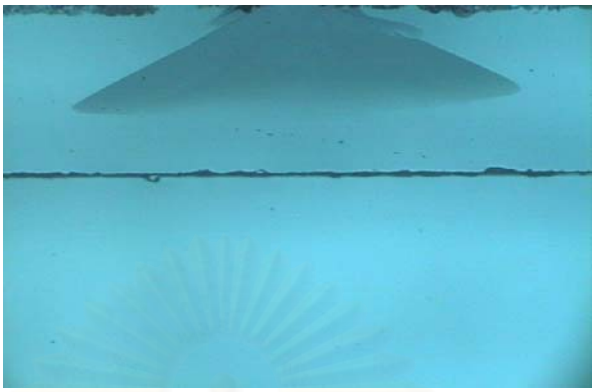

(b)

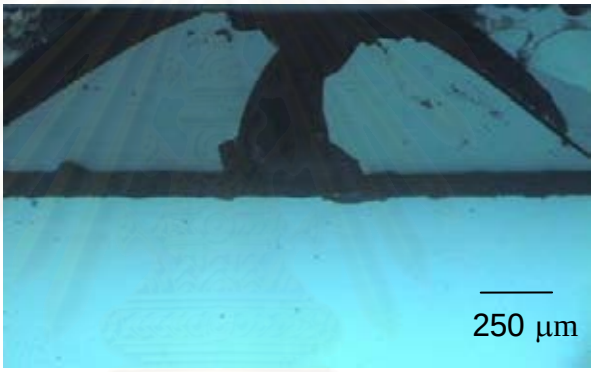

Fig. 4.34 Hertzian contact damage for two adhesive polymer thicknesses, h = 20 and 200 μm, due to a WC sphere r = 1.59 mm at fixed coating thickness d = 500 μm, for load P = 100 N, illustrates the effect of interface adhesive polymer thickness on the damage patterns. (a) h = 20 μm and (b) h = 200 μm. Note the damage increases with increasing h.

4.5 Effect of Young's Modulus of Interface Layer on Damage Patterns of Coating Layers

Figure 4.35 shows the effect of Young's Modulus of interface layer on damage patterns of coating layers for indentation load P = 200 N, with a WC sphere r = 1.59 mm. Three systems are glass/steel-epoxy resin/glass, glass/epoxy resin/glass and glass/silicone sealant/glass with coating thickness of 1000 μm and adhesive thickness h = 20 μm. Young's moduli of steel-epoxy resin, epoxy resin and silicone sealant are called E_1, E_2 and E_3, respectively, and $E_1 > E_2 > E_3$. The micrographs show the cone crack fractures in the coating layer without any crack in the substrate. The cone crack length of glass/steel-epoxy resin/glass system is the shortest (Fig. 4.35 (a)), and the longest crack length occurs in glass/silicone sealant/glass system (Fig. 4.35(c)) at the same load. However, there are many cone cracks occurring in glass/silicone sealant/glass system and they do not appear to extend much further in depth than the first cone crack. Plots of the cone crack length in coating layer as a function of indentation load are shown in Fig. 4.36. The cone crack length of glass/epoxy resin/glass (Fig. 4.35 (b)) changes slightly between P = 200 N and 250 N. (Fig. 4.17 (d)) It's assumed that the cone crack length increases with increasing load until it reaches a peak before changing from a single cone crack system to a multiple crack system. So the primary effect of increased loading is to increase the density rather than the depth of cone cracks. That is damage increases as indentation load increases. From this effect it indicates that system jointing with silicone sealant has got the most damage when the load is increasing.

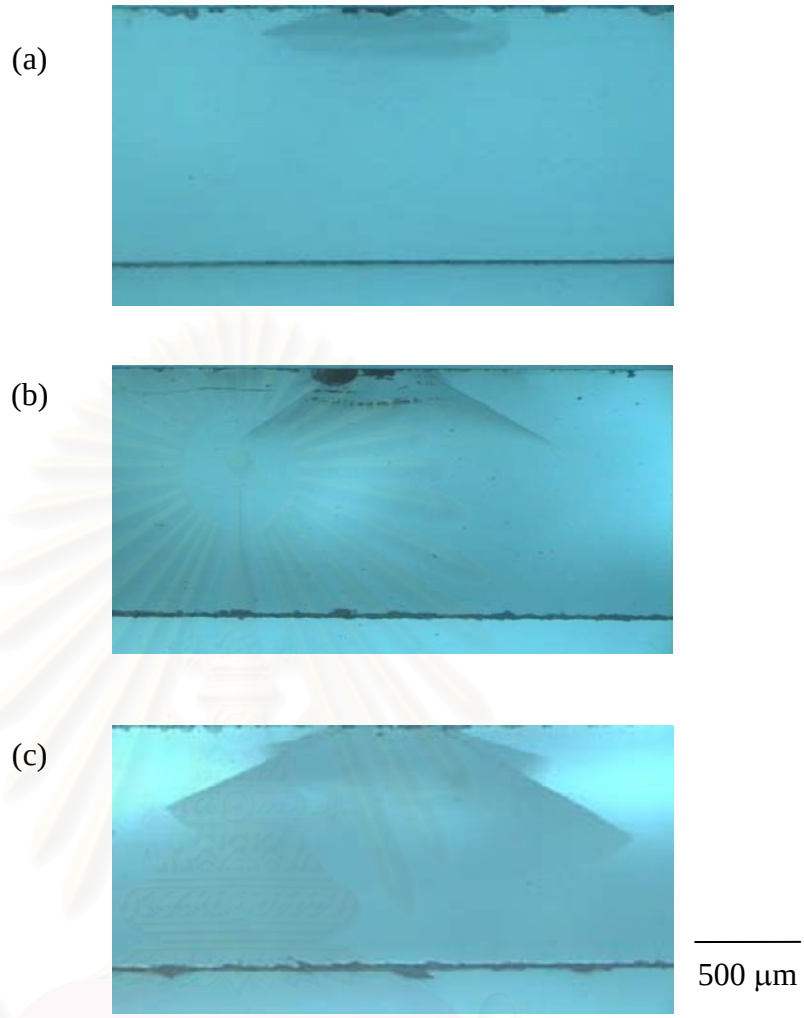

Fig. 4.35 Contact fracture in glass/steel-epoxy resin/glass, glass/epoxy resin/glass and glass/silicone system for indentation load P = 200 N, due to a WC sphere r = 1.59 mm. It shows the effect of Young's Modulus of interface layer on damage patterns of coating thickness d = 1000 μm and the adhesive thickness h = 20 μm: (a) system E_1; (b) system E_2; and (c) system E_3. Note that $E_1 > E_2 > E_3$.

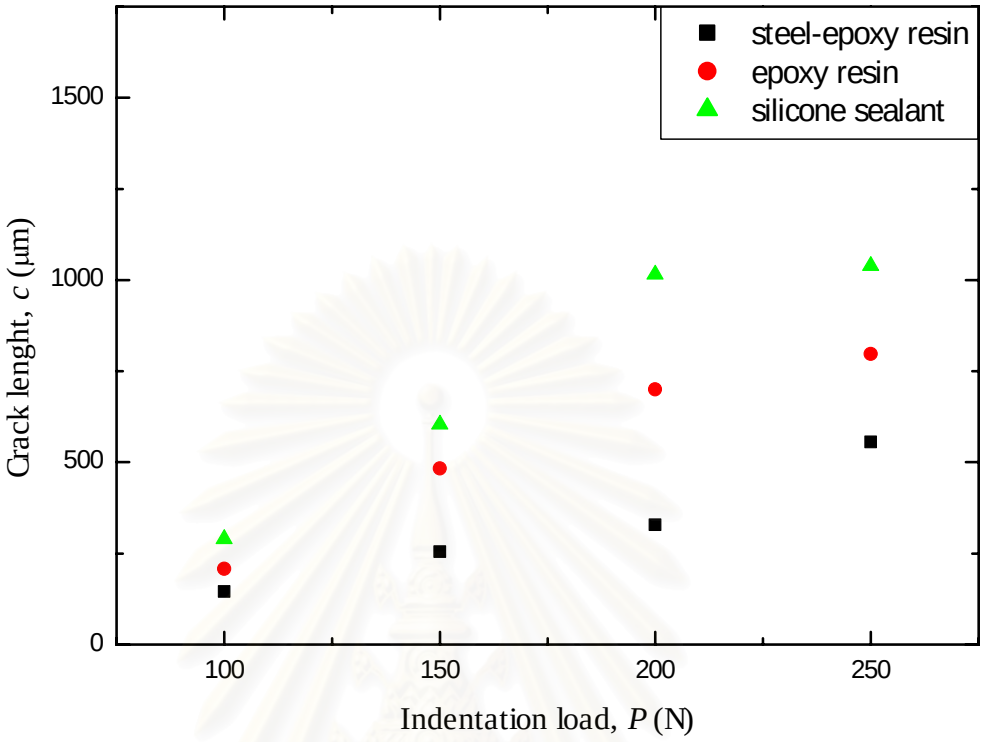

Fig. 4.36 Plot of the cone crack length in the coating layer as a function of indentation load. For glass/ steel-epoxy resin/ glass system, glass/ epoxy resin/ glass system and glass/ silicone sealant/ glass system with d = 1000 μm and h = 20 μm.

Figure 4.37 shows the effect of Young's Modulus of interface layer on damage patterns of the coating layers at indentation load P = 250 N for d = 1000 and 500 μm and h = 20 μm. As the same h at fixed load P, the effect of coating thickness on the damage patterns of all adhesives is correspondent. That is the damage increases when the coating thickness decreases and P_r decreases as d decreases. It indicates that the damage pattern in coating layer depends on coating thickness. In coating thickness d = 500 μm silicone sealant system is damaged the most, whereas steel-epoxy resin is the least. The radial crack is generated the most easily in the silicone sealant system and it is generated more easily in epoxy than in steel-epoxy resin because the radial crack length of epoxy resin system is longer. Consequently, P_r of silicone sealant system is the least to initiate the radial crack. Moreover P_r of steel-epoxy resin system is the most to initiate the radial crack. It indicates that E decreases will cause decreasing P_r.

Figure 4.38 shows the effect of Young's Modulus of interface layer on damage patterns of the coating layers at indentation load P = 100 N for h = 20 and 200μm and d = 500μm. As the same d at fixed load P, the effect of adhesive polymer thickness on the damage patterns of all adhesives is correspondent. That is the damage increases when adhesive polymer thickness increases and P_r decreases as h increases. It indicates that the damage pattern in the coating layer is depends on adhesive polymer thickness. From adhesive polymer thickness h = 200 μm, silicone sealant system is damaged the most, whereas steel-epoxy resin is the least. It indicates that E decreases will cause damage to increase.

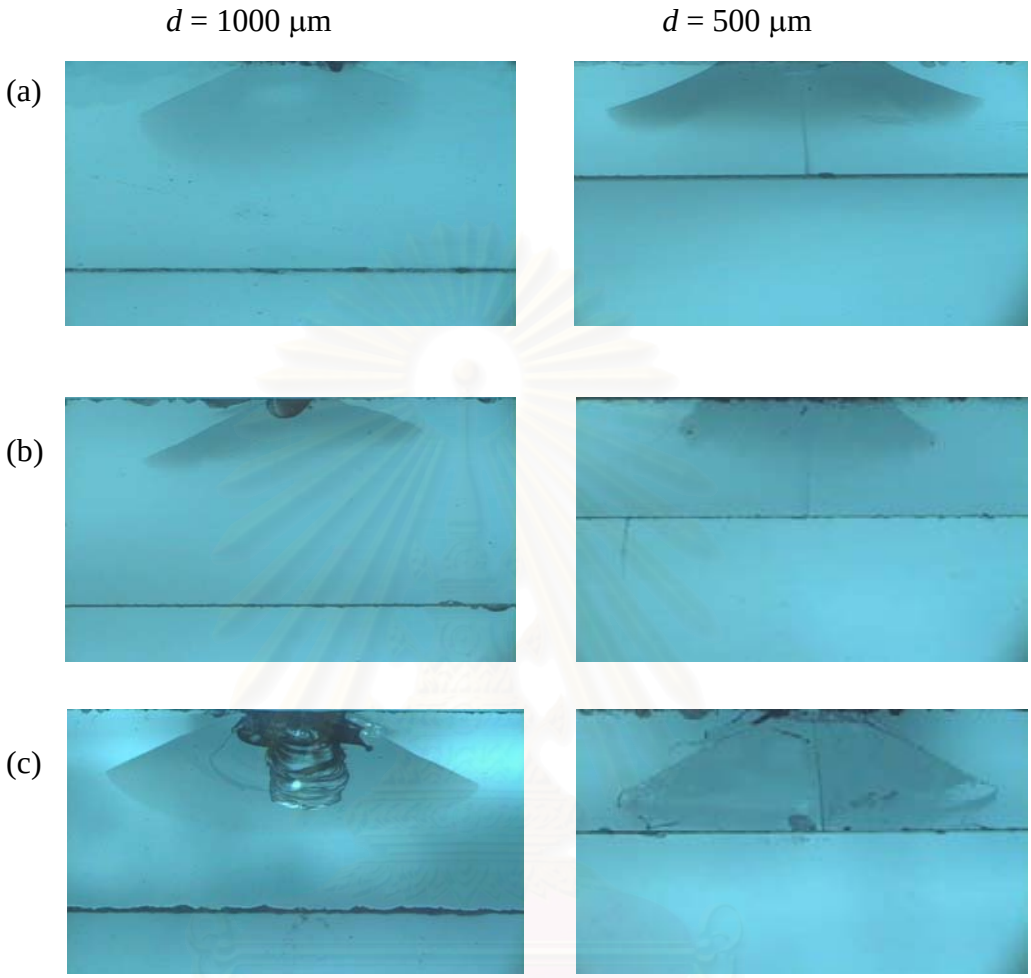

Fig. 4.37 Effect of Young's Modulus of three interface layer on damage patterns of coating layers at indentation load P = 250 N, h = 20μm for d = 1000 and 500μm :(a) glass/ steel-epoxy resin/ glass system; (b)glass/ epoxy resin/ glass system; and (c) glass/silicone sealant/glass system. Note that the damage increases when E decreases.

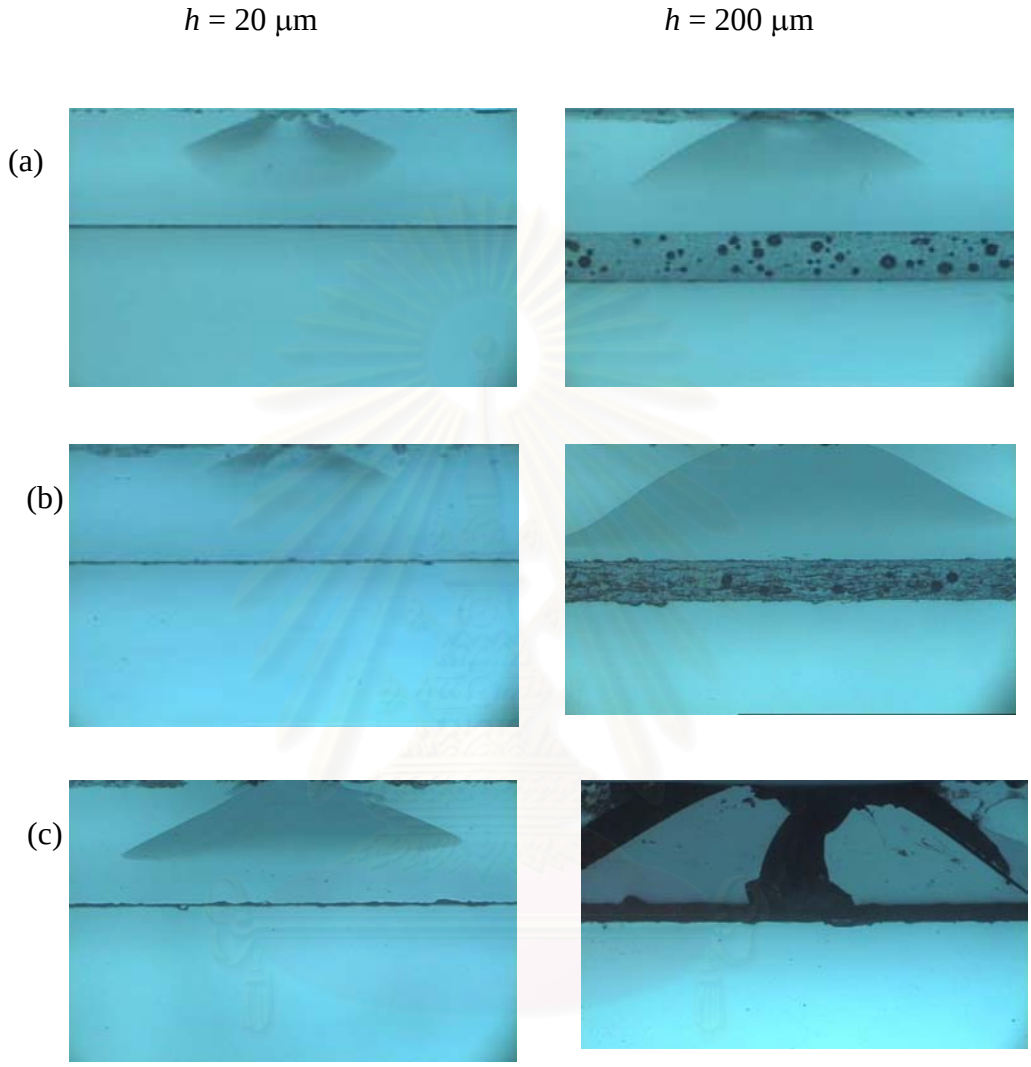

Fig. 4.38 Effect of Young's Modulus of three interface layer on damage patterns of coating layers at indentation load P = 100 N, d = 500μm for h = 20 and 200μm:(a) glass/steel-epoxy resin/glass system; (b) glass/epoxy resin/glass system: and (c) glass/silicone sealant/glass system. Note that the damage increases when E decreases.

CHAPTER V

DISCUSSION AND CONCLUSIONS

In the layer structure, two crack systems occur in the glass coating: the cone crack initiates at the top surface; and the radial crack initiates at the interface. The second crack type is due to the presence of adhesive interlayer which allows the coating layer to flex beneath the contact, leading to the initiation of the upward extending radial cracks at the bottom surface of the coating layer on the median plane containing the contact axis. The results of Hertzian indentation on the three glass/adhesive polymer/glass systems indicate that only cone cracks are initiated in the thick coating layer of thickness of 1000 μm as h = 20 μm. At the same load, the cone crack length of glass/steel-epoxy resin/glass system is the shortest, and the longest crack length occurs in glass/silicone sealant/glass system. It is noted that the response of glass/steel-epoxy resin/glass on Hertzian contact with the thick coating and small adhesive thickness is the most closely resemble to that of the bulk glass.

However, the primary effect of increased loading is to increase the density rather than the depth of cone cracks. The cone crack density increases as the load increases at any specified d and h. Furthermore the specimens with the silicone sealant interlayer are damaged the most, whereas those with the steel-epoxy resin interlayer are the least. That is the damages increase as Young's modulus of the adhesive interlayer decreases. For the effect of coating thickness, it is found that the damage increases when the coating thickness decreases, and P_r decreases when d decreases at any specified h. Furthermore, decreasing E of the adhesive interlayer

results in increasing damages. For the effect of adhesive interlayer thickness, it is found that increasing h results in decreasing P_r at any specified d, and the damages increase as E of the adhesive interlayer decreases. On other words, our results of the Hertzian indentation tests indicate that the Young's modulus of adhesive interlayer have a profound influence on fracture modes of the brittle layer structures. The ratio between the adhesive interlayer thickness and the coating thickness is important. Since the Young's modulus of silicone sealant interlayer (0.00025 GPa) is very small, the silicone sealant interlayer can flex most during the contact. Consequently, it allows the flexure mode to develop and generate radial fractures at the bottom surface of the coating layer. In addition, the critical load inducing the radial crack is inversely proportional to the ratio of adhesive and coating thicknesses. Therefore, indentation loads ($50 \text{ N} \leq P \leq 250 \text{ N}$) might be not enough to generate the radial crack in the layer system of the coating thicknesses 1000 μm and the adhesive thickness 20 μm for all adhesives.

From this work, the coating thickness is an important variable. When the coating is thick, cracks initiate at the top surface, similar to monolithic material. Radial crack occurs only at higher loads. Decreasing the coating thickness enhances cracking in the coating. In the thin coatings, cracks initiate from both the top surface and the coating/substrate interface. This result indicates that the thickness of the coating should be at least as large as the prospective contact dimension for optimum substrate protection. This implies that for the dental restoration, for example, the thickness of the enamel should be related to contact radius and cuspal radius (≈2-4 mm). On the other hand, thin coatings may not always protect the substrate in heavy loading conditions.

In addition, the strength of interface layer also plays an important role in cracking and the type of damage incurred. When the bond between the coating and substrate is strong, as in the glass/steel- epoxy resin/glass, glass/ epoxy resin/glass and glass/silicone sealant/glass, delamination along the interlayer is avoided. A strong interface is desirable because the coating can remain intact on the substrate without removal and no penetrating crack. This implies that for substrate protection, such as in car windscreen, cutting tools or dental restorations, the interlayer strength should be strong so that the coating can protect the substrate without coating removal from the substrate during the application, and the adhesive needs to be weak enough to prevent the cracks from penetrating into the adjacent layers.

Since the Young's modulus of steel-epoxy resin is highest among those of the adhesive interlayers used in the layered-structure models in this work, the elastic mismatch between glass coating and steel-epoxy resin is smallest. Therefore the numbers of cracks in the coating of this glass/ steel-epoxy resin/glass system at a given load are found to be less than the other two trilayer systems. Although the cracks in the coating of the models with the silicone sealant interlayer which has the softest adhesive interlayer used in this work, are found not to be able to penetrate into the substrate, the models with the silicone sealant interlayer are damaged the most during the indentation, especially in the models with small coating thickness and large interlayer thickness. So, the design of the appropriate layer geometry with low Young's modulus of interlayer is the layer with small interlayer thickness and large coating thickness. For optimum substrate protection, the results from this work indicate a brittle coating with low elastic mismatch between the coating and the

adhesive interlayer is desirable. However, these requirements must ultimately be balanced against the costs of fabricating and finishing.

Another area of interest, which relates to engineering layer design, is fracture mechanism in layer structures. We need to know why and how radial cracks in the coating stop extending into substrates and do not even intersect the interlayer interfaces. This mechanism is not quite understood. It is important to do further work to determine the causes of the crack inhibition in the coating near the interlayer interfaces. A combination of finite element analysis with the in-situ observation of crack behavior in the layer structure experiments could provide more insight into fracture mechanism in the layer structure during indentation.

REFERENCES

1. Graff, G. Ceramics Take on Tough Tasks. The Materials Revolution. Forester, T., ed. Massachusetts: The MIT Press, (1998): 179-192.
2. Kingery, W.D. Looking to the Future in Ceramics. The Materials Revolution. Forester, T., ed. Massachusetts: The MIT Press, (1988): 315-328.
3. Tressler, R.E., Messing, G.L, Pantano, C.G, and Newnham, R.E. eds. Tailoring of Multiphase and Composite Ceramics. New York: Plenum, 1986.
4. Chan, H.M. Layered Ceramics: Processing and Mechanical Behavior. Annu.Rev. Mater.Sci. 27 (1997): 249-282.
5. Pajares, A., Wei, L., Lawn, B.R., Padture, N.P., and Berndt, C.C. Mechanical Characterization of Plasma-Spayed Ceramic Coatings on Metal Substrates. Mater.Sci.Eng. A208 (1996): 158-165.
6. Pinyo, L. Processing and Mechanical Properties of Hydroxyapatite /Tetragonal Zirconia Bilayer Structure. Master's Thesis, Department of Physics, Faculty of Science, Chulalongkorn University, 2002.
7. Virkar, A.V., Huang, J.L., and Cutler, R.A. Strengthening of Oxide Ceramics by Transformation-Induced Stress. J.Am.Ceram.Soc. 70 (1987): 164-170.
8. Virkar, A.V., Jue, J.F., Hansen, J.J., and Cutler, R. A. Measurement of residual stresses in Oxide-ZrO_2 Three–layer Composites. J.Am.Ceram.Soc. 71 (1988): C-148-151.
9. Phillipps, A.J., Clegg, W.J., and Clyne, T.W. Fracture Behavior of Ceramic Laminates in Bending-I. Modelling of Crack Propagation. Acta Metall. Mater. 41 (1993): 805-817.

10. Clegg, W.J. and Seddon, L.R. The Failure of Tough Ceramic Laminates. Euro. Mat.91.Anvances in Structural material. 2 (1991): 266-69.

11. Clegg, W.J. The Frabricaton and Failure of Laminatar Ceramic Composites. Acta Metall. Mater. 40 (1992): 3085-3093.

12. Mawdsley, J.R., Kovar, D. and Halloran, J.W. Fracture Behavior of Alumina/Monazite Multilayer Laminates. J.Am.Ceram.Soc. 83 (2000):802-808.

13. Russo, C.J., Hammer, M.P., Chan, H. M., and Miller, G.A. Design of a Laminated Ceramic Composite for Improved Strength and Toughness. J.Am.Ceram. Soc. 75 (1992): 3396-3400.

14. Russo, C.J., Hammer, M.P., Chan, H. M., and Miller, G.A. Mechanical Properties of Laminated Ceramic Composites in Alumina-and Zirconia-Based Systems. Ceram. Eng. Sci. Proc. 14 (1993): 998-1005.

15. Gordon, J.E. The New Science of Strong Materials. Harmondsworth: Penguin, 1968.

16. Folsom, C.A., Zok, F.W., and Lange, F.F. J.Am.Ceram.Soc. 77(1994):2081

17. Lawn, B.R. Fractrue of Brittle Solids. Ch.8. London: Cambridge University, 1994.

18. Jung, Y.G., Wuttiphan, S., Peterson, I.M., and Lawn, B.R. Damage Modes in Dental Layer Structures. J. Dent. Res. 78(1999): 887-897.

19. Russo, J., Harmer, M. P., Chan, H.M., and Miller., G. A. Design of a Laminated Ceramic Composite for Improved Strength and Toughness. J.Am.Ceram. Soc.75 (1992): 3396-3400.

20. Wuttiphan, S., Lawn, B.R., and Padture, N.P. Crack Suppression in strongly Bonded Homogeneous/Heterogeneous Laminates: A study on Glass/ Glass-Ceramic Bilayers. J. Am. Ceram. Soc. 79 (1996): 634-640.

21. Liu, H., Lawn, B.R., and Hsu, S. M. Hertzian Contact Response of Tailored Silicon Nitride Multilayers. J. Am. Ceram.Soc.79 (1996):1009-1014

22. Lee, K.S., Wuttiphan, S., Hu, X.Z., Lee, S.K., and Lawn, B.R. Contact Induced Transverse Fractures in Brittle Layers on Soft Substrates: A Study on Silicon Nitride Bilayers. J.Am.Ceram.Soc. 81 (1998): 571-580.

23. Lee, K.S., Wuttiphan, S., Lawn, B.R., and Kim, D.K. Contact Damage and Strength Degradation in Brittle/Quasi-Plastic Silicon Nitride Bilayers. J. Am.Ceram.Soc.81(1998): 294-304

24. Wei, L., Pajares, A., and Lawn, B.R. Effect of Mechanical Damage on Thermal Conduction of Plasma Sprayed Coatings. J.Mater.Res. 11(1996):1329-1332.

25. Pajares, A., Wei, L., Lawn, B. R., Padture, N.P., and Berndt, C.C. Mechanical Characterization of Plasma- Sprayed Ceramic Coatings on Metal Substrates by Contact Testing. Mater.Sci.Eng. A208 (1996): 158-165

26. Fischer-Cripps, A.C., Lawn, B. R., Pajares, A., and Wei, L. Stress Analysis of Elastic-Plastic Contact Damage in Ceramic Coatings on Metal Substrates. J.Am.Ceram.Soc. 79 (1996): 2619-2625.

27. Pajares, A., Wei, L., Lawn, B.R., and Berndt, C.C. Contact Damage in Plasma-Sprayed Alumina-Based Coatings. J.Am.Ceram.Soc. 79 (1996): 1907-1914.

28. Wuttiphan, S., Pajares, A., Lawn, B. R., and Bermdt, C.C. Effect of Substrate and Bond Coat on Contact Damage in Zirconia- Based Plasma Coatings. Thin Solid Films. 293 [1-2] (1997): 251-260.

29. An, L. H., Chan, M., Padture, N. P., and Lawn, B. R. Damage-Resistant Alumina-Based Layer Composites. J. Mater.Res.11 (1996): 204-210.

30. Kim, H.W., Deng, Y., Miranda, P., Pajares, A., Kim, D.K., Kim, H.E., and Lawn, B. R. Effect of Flaw State on the Strength of Brittle Coating on Soft Substrates. J.Am.Ceram.Soc. 84 (2001):2377-2384.

31. Chai, H., Lawn, B.R., and Wuttiphan, S. Fracture modes in brittle coating with large interlayer modulus mismatch. J. Mater.Res. 14 (1999): 3805-17.

32. Lawn, B.R., Lee, K.S., Chai, H., Pajares, A., Kim, D.K., Wuttiphan, S., Peterson , I.M., and Hu, X. Damage-Resistant Brittle Coating. Advanced Engineering Materials. 2 (2000): 745-748.

33. Chai, H. and Lawn, B.R. Role of Adhesive Interlayer in Transverse Fracture of Brittle Layer Structures. J.Mater.Res. 15 (2000): 1017-24.

34. Mencik, J. Strength and Fracture of Glass and Ceramics. Czechoslovakia: Elsevier, 1992.

35. Holloway, D.G. The Physical Properties of Glass. London and Winchester: Wykeham, 1973.

36. Callister, W. D. Materials Science and Engineering an Introduction. USA: John Wiley & Sons, 1991.

37. Kingery, W.D., Bowen, H.K., and Uhlmann, D.R. Introduction to Ceramics. New York: John Wiley & Sons, 1976.

38. Meyers, M.A. and Chawla, K. K. Mechanical Behavior of Materials. USA: Prentice-Hall, 1999.

39. Anderson, G.P. Encyclopedia of Physical Science and Technology. (1987): 221

40. Skeist, I. Handbook of Adhesives. 2 nd ed., New Jersey: Van Norstrand Reinhold, 1997.

41. Thomas, A. Surface Coating.(1990): 179

42. Hertz, H. Hertz's Miscellaneous Papers. Chs.5, 6. London: Macmillan, 1896.

43. Johnson, K.L. Contact Mechanics. London: Cambridge University Press, 1985.

44. Lawn, B.R. Fracture of Brittle Solids. 2 nd ed., Cambridge Solid State Science Series. Great Britain: Cambridge University (1993).

45. Lawn, B.R. and Wilshaw. T.W. Fracture of Brittle Solids. London: Cambridge University, 1975.

46. Irwin, G.R. Handbook of Physics. Berlin: Springer-Verlag, 1958.

47. Wiederhron, S.M. Subcritical Crack Growth in Ceramics. Fracture Mechanics of Ceramics.vol.2. New York: Plenum, 1974.

48. Lawn, B.R. and Wilshaw, T.W. Indentation Fracture: Principles and Applications. J.Mater.Sci. 10 (1975): 1049-1081.

49. Timoshenko, S. and Goodier, J.N. Theory of Elasticity. Ch.13. New York: McGrawHill, 1951.

50. Lawn, B.R. Indentation of Ceramics with Spheres: A Century after Hertz. J.Am.Ceram.Soc. 81 (1998): 1977-94.

51. Tabor, D. Hardness of Metals. Oxford: Clarendon, 1951.

52. Swain, M.V. and Lawn, B.R. A Study of Dislocation Arrays at Spherical Indentations in LiF as a Function of Indentation Stress and Strain. Phys. Status Solodi. 35(1969): 909-923.

53. Huber, M.T. Zur Theorie der Berührung Fester Elasticher Körper. Ann.Phys. 43(1904): 153-163.

54. Frank, F.C. and Lawn, B.R. On the Theory of Hertzian Fracture. Proc. R. Soc. London.1458 (1967): 291-306.

55. Auerbach, F. Measurement of Hardness. Ann. Phys. Chem. 43(1891):61.

56. Langitan, F.B. and Lawn, B.R. Hertzian Fracture Experiments on Abraded Glass Surfaces as Definitive Evidence for an Energy Balance Explanation of Auerbach's Law. J. Appl. Phys. 10 (1969): 4009-4017.

57. Lawn, B.R., Wilshaw, T.W., and Hartley, N.E.W. Int.J.Fract. 10 (1974: 1-16.

58. Lawn, B.R., Wiederhron, S.M., and Johnson, H. Strength Degradation of Brittle Surfaces: Blunt Indenter. J. Am. Ceram. Soc.58 (1975): 428-432.

59. ASTM: D 638-95, Standard Test Methods for Tensile Properties of Plastic.

60. Singh, K. Mechanics of Materials. Delhi:Standard Publishers Distributors, 2000.

VITAE

My name is Porntip Sakolkool. I was born on 20th June, 1978, at Buriram Province. I received the Bachelor of Science (Physics) from the Faculty of Science and Technology, Thammasat University in February, 2001. I received the Local Graduate Scholarship from National Science and Technology Development Agency (NSTDA) and financial-support research from Chulalongkorn University to study for Master degree in Physics at Chulalongkorn University.